

REPORT DOCUMENTATION PAGE			Form Approved OMB No. 0704-0188	
Public reporting burden for this collection of information is estimated to average 1 hour per response, including the time for reviewing instructions, searching existing data sources, gathering and maintaining the data needed, and completing and reviewing the collection of information. Send comments regarding this burden estimate or any other aspect of this collection of information, including suggestions for reducing this burden, to Washington Headquarters Services, Directorate for Information Operations and Reports, 1215 Jefferson Davis Highway, Suite 1204, Arlington, VA 22202-4302, and to the Office of Management and Budget, Paperwork Reduction Project (0704-0188), Washington, DC 20503.				
1. AGENCY USE ONLY (Leave blank)	2. REPORT DATE 28.Sep.00	3. REPORT TYPE AND DATES COVERED DISSERTATION		
4. TITLE AND SUBTITLE NONLINEAR ULTRASOUND IMAGE MODELING: DEVELOPMENT OF A COMPLETE END-TO-END MODEL FOR QUALITATIVE AND QUANTITATIVE ANALYSIS OF MEDICAL ULTRASOUND		5. FUNDING NUMBERS		
6. AUTHOR(S) MAJ AYER KEVIN W				
7. PERFORMING ORGANIZATION NAME(S) AND ADDRESS(ES) ROCHESTER INSTITUTE OF TECHNOLOGY		8. PERFORMING ORGANIZATION REPORT NUMBER CY00373		
9. SPONSORING/MONITORING AGENCY NAME(S) AND ADDRESS(ES) THE DEPARTMENT OF THE AIR FORCE AFIT/CIA, BLDG 125 2950 P STREET WPAFB OH 45433		10. SPONSORING/MONITORING AGENCY REPORT NUMBER		
11. SUPPLEMENTARY NOTES				
12a. DISTRIBUTION AVAILABILITY STATEMENT Unlimited distribution In Accordance With AFI 35-205/AFIT Sup 1			12b. DISTRIBUTION CODE	
13. ABSTRACT (Maximum 200 words)				
14. SUBJECT TERMS			15. NUMBER OF PAGES 123	
			16. PRICE CODE	
17. SECURITY CLASSIFICATION OF REPORT	18. SECURITY CLASSIFICATION OF THIS PAGE	19. SECURITY CLASSIFICATION OF ABSTRACT	20. LIMITATION OF ABSTRACT	

Nonlinear Ultrasound Image Modeling: Development of a Complete End-to-End Model for
Qualitative and Quantitative Analysis of Medical Ultrasound

by

Kevin W. Ayer

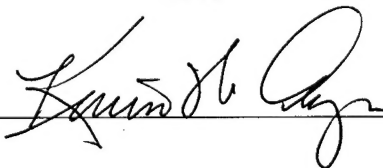
Major, United States Air Force

B.S., Chemistry, University of Texas at El Paso, El Paso, Texas, 1982
B.S., Electrical Engineering, Auburn University, Auburn, Alabama, 1986
M.S., Electrical Engineering/Electro-Optics, Air Force Institute of Technology,
Wright-Patterson Air Force Base, Ohio, 1989

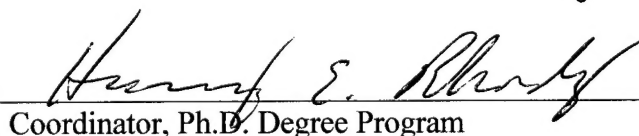
A dissertation submitted in partial fulfillment of the
Requirement for the degree of Doctor of Philosophy
To the Chester F. Carlson Center for Imaging Science
Rochester Institute of Technology

2000

Signature of the Author



Accepted by



Coordinator, Ph.D. Degree Program

8 Jun 2000
Date


20001013 056

CHESTER F. CARLSON CENTER FOR IMAGING SCIENCE
ROCHESTER INSTITUTE OF TECHNOLOGY
ROCHESTER, NEW YORK


CERTIFICATE OF APPROVAL

Ph.D. DEGREE DISSERTATION

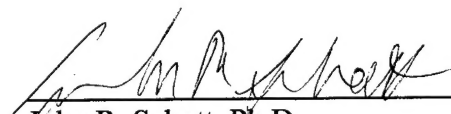
The Ph.D. Degree Dissertation of Major Kevin W. Ayer
has been examined and approved by the
dissertation committee as satisfactory for the
dissertation required for the
Ph.D. degree in Imaging Science



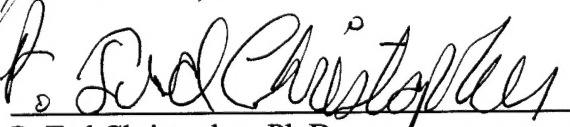
N. A. H. K. Rao, Ph.D., Dissertation Advisor



Theodore W. Wilcox, Ph.D.



John R. Schott, Ph.D.



P. Ted Christopher, Ph.D.



Date

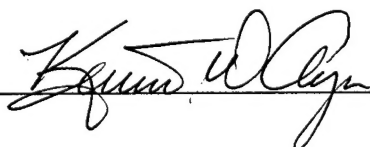
DISSERTATION RELEASE PERMISSION
ROCHESTER INSTITUTE OF TECHNOLOGY
CHESTER F. CARLSON CENTER FOR IMAGING SCIENCE

Title of Dissertation:

Nonlinear Ultrasound Image Modeling: Development of a complete End-to-End Model for
Qualitative and Quantitative Analysis of Medical Ultrasound

I, Kevin W. Ayer, hereby grant permission to Wallace Memorial Library of R.I.T. to reproduce
my thesis in whole or in part. Any reproduction will not be for commercial use or profit.

Signature



8 Jun 2000
Date

Nonlinear Ultrasound Image Modeling: Development of a complete End-to-End Model for Qualitative and Quantitative Analysis of Medical Ultrasound

by

Kevin W. Ayer

Submitted to the Chester F. Carlson Center for Imaging Science
in partial fulfillment of the requirement for the
Doctor of Philosophy Degree
at the Rochester Institute of Technology

Abstract

Finite amplitude sound propagation undergoes nonlinear distortion due to continuous path interaction with the propagation medium. This distortion tends to defocus the beam causing significant lateral and contrast resolution degradation. Fundamental understanding of this interaction requires development of computational models that accurately predict the nonlinear interaction – development of media-borne harmonics – as well as produce an ultrasound image – introduction of transducer effects, interface transitions, and innovative image processing to extract harmonics. Most computational models of ultrasound propagation assume axial symmetry for computational expediency. Two notable exceptions are the K-Z-K and NLP models. A new end-to-end model, NUPROP, is introduced that also incorporates non-axially symmetric geometries and simplified transducer responses to accurately predict ultrasound RF signals for image reconstruction. Nonlinearities are modeled using either the Fubini solution or Burgers' Equation coupled with angular spectrum propagation or Lommel formulation, appropriately masked by the transducer frequency response. Comparative analyses are performed on NUPROP results with high correlation with the literature. Parameter sensitivity analyses are performed to determine harmonic signal characteristics as a function of propagation distance. A-line and B-scan images are produced.

Acknowledgements

There were three aims of this research: first, to develop an accurate predictive model of ultrasound wave propagation in various media. The second aim was to use the model to predict signals, developing an understanding of parameter sensitivities in generating harmonic ultrasound images. Verification was accomplished using existing data from previous experimentation as well as data from other simulations. Finally, the third aim was to develop a technique whereby the user could reliably predict, both qualitatively and quantitatively, the effects of nonlinearity on ultrasound wave propagation and subsequent image reconstruction, thus advancing the scientific community's understanding of nonlinear ultrasound. These goals have been accomplished and I owe my success to many people, whom I publicly thank in this dissertation.

I am deeply indebted to Dr. Navalgund A. H. K. Rao, my advisor, for his undaunted pursuit of truth and in whom I could depend for hours of remarkably keen discussion. His encouragement and enthusiasm inspired me, giving me that intellectual spark to succeed. I thank Dr. Rao for all that he has taught me. I am also indebted Dr. Ted Wilcox, my committee chair, whose snippets of mathematical brilliance only he could provide.

I greatly appreciate the valuable criticism and deep insight into nonlinear wave propagation Dr. Ted Christopher provided throughout the development and implementation of NUPROP. His unique mannerisms and calm demeanor brought a measure of peace to the turmoil of developing NUPROP as a useful modeling tool.

I thank Dr. John Schott for his unique contributions to this development effort. The "can you apply it?" perspective kept me continually focused on application of this dissertation work.

Outside of my committee, I thank the faculty and staff at the Chester F. Carlson Center for Imaging Sciences. Everyday was a wonderful experience. Their support was priceless. Many

thanks to Dr. Arney, who listened well and knew when to bring humor into a trying time; and to Dr. Rhody, whose "down-home" teaching style made learning a joy. I deeply thank Dr. Maria Helguera for her technical support in the laboratory, and tons of data without which verification of NUPROP could not have been accomplished. Many thanks to Barb Capierso, who kept me in supply of paper, pens, and just about anything I needed, to Sue Chan, who kept my academic record in "spit-spot" shape so I could graduate, and to Carolyn Kitchen, who made acquisition of computers (and just about any other large item I needed) a snap.

Among my fellow students, I thank Dr. Erich Hernandez-Baquero who provided a great sounding board for my research; Dr. Ron Fairbanks, who taught me to make any decision into a course of action; and, finally, to Dr. Charles "Chaz" Daly, with whom I had tremendously fruitful technical discussions, in person and via e-mail.

This work is dedicated to God and my family,
from whom I gain great strength and reassurance that, no matter what may come,

I am loved.

For Lynn, my beloved wife,

For Kyleen and Kyle, my wonderful children.

Contents

ABSTRACT	III
ACKNOWLEDGEMENTS.....	IV
CONTENTS	VII
LIST OF FIGURES	X
CHAPTER 1. INTRODUCTION	2
CHAPTER 2. LITERATURE REVIEW.....	4
NONLINEAR WAVE PROPAGATION	4
LINEAR WAVE PROPAGATION.....	7
OTHER APPROACHES	10
IMAGE MODELING	13
CHAPTER 2: SUMMARY.....	15
CHAPTER 3. NUPROP MODULE DEVELOPMENT.....	17
PHANTOM GENERATION: CONTINUOUS POINT SCATTERER ARRAY	17
WAVEFORM TYPE.....	18
<i>Single Frequency Sinusoid</i>	18
<i>Narrowband Frequency Sinusoid</i>	18
<i>Linear Frequency Modulated Sinusoid (Apodized and Non-Apodized)</i>	19
WAVE PROPAGATION: NONLINEAR.....	20
<i>Burgers' Equation Model</i>	20

<i>Fubini Solution Model</i>	21
WAVE PROPAGATION: LINEAR	22
<i>Angular Spectrum Model</i>	22
<i>Lommel Formulation</i>	23
IMAGE GENERATION	24
POST PROCESSING: STATISTICAL ANALYSES	28
CHAPTER 3: SUMMARY	30
 CHAPTER 4. CODE DEVELOPMENT AND DESCRIPTION	 32
NUPROP HIERARCHY	32
MENU OPERATIONS	37
<i>File</i>	37
<i>Execute</i>	37
CHAPTER 4: SUMMARY	45
 CHAPTER 5. NUPROP VERIFICATION	 46
LONGITUDINAL SIGNAL FORMATION.	46
TRANS-AXIAL SIGNAL FORMATION	52
IMAGE FORMATION	53
CHAPTER 5: SUMMARY	54
 CHAPTER 6. EXERCISING NUPROP	 56
SINGLE FREQUENCY SINUSOID: ONSET DISTANCE COMPUTATION	57
<i>Effects of B/A Ratio and Path Attenuation Variation on Onset Distances for Second and Third Harmonic</i>	
<i>Signal Generation</i>	58
<i>Effects of Varying Input Signal Strength on Onset Distance</i>	62

<i>Effects of Varying Input Signal Frequency on Onset Distance</i>	62
NARROWBAND SINUSOID: IMAGE FORMATION	63
<i>Effects of Frequency Variation on Image Generation</i>	63
<i>Effects of Varying B/A Ratio on Image Generation</i>	66
<i>Effects of Varying Signal Amplitude on Image Formation</i>	69
<i>Effects of Varying Wave Velocity on Image Formation</i>	71
THE APODIZED CHIRP: EXPERIMENT VERSUS NUPROP MODELING	73
SIMULATION: NARROWBAND SINUSOID VERSUS APODIZED CHIRP	79
CHAPTER 6: SUMMARY	83
CHAPTER 7. CHAPTER SUMMARIES AND	
RECOMMENDATIONS.....	86
CHAPTER SUMMARIES.....	86
RECOMMENDATIONS.....	92
<i>NUPROP Code Validation</i>	92
<i>Code Improvements</i>	95
REFERENCES	107
APPENDICES	111
APPENDIX I. MATHEMATICAL DEVELOPMENT OF BURGERS' EQUATION	111
APPENDIX II. MATHEMATICAL DEVELOPMENT OF FUBINI'S SOLUTION	113
APPENDIX III: LINEAR FREQUENCY MODULATED INPUT SIGNAL (CHIRP)	119

List of Figures

- Figure 2-1. Graphical representation of a complex pressure field propagating from one parallel plane to another using the angular spectrum technique. 7
- Figure 3-1. Frequency dependent and independent apodization schemes for ensuring minimum overlap of frequency signals: fundamental, second, and subsequent harmonics. The signal is presented in dB scale. The fundamental frequency is arbitrarily set to 2.5 MHz, with second and third harmonics shown at 5.0 MHz and 7.5 MHz, respectively. The apodization functions are Gaussian with exponent 2..... 18
- Figure 3-2. Examples of apodized and non-apodized linear frequency modulated sinusoids. Initial frequency: 1.5 MHz, sweep rate of 1.5×10^{12} , and apodization to ensure minimum harmonic signal overlap. Note that the chirps represented here consist of the fundamental and 10 harmonics of the initial frequency. 19
- Figure 3-4. Example of statistical analyses from NUPROP ultrasound simulation widget. The left panel displays the simulated images for the fundamental, second and third harmonics, and the phantom along with their respective thresholded images. For this example, a simple threshold level of 40 was used. The upper right panel displays the histogram plots for each simulation image. The lower right panel displays each simulated image's statistics: mean, variance, and skew..... 29
- Figure 4-1. NUPROP hierarchy of processing. Each first-level base is designated with an underline: Menu, Radio Button, Parameter Input, and Display. Each second-level base is designated by the origination of an arrow such as File under the Menu Base Operations. Each third-level base is designated by smaller print text such as Sinusoid Chirp of Radio Button Base as well as a termination and origination of an arrow. Each fourth-level base is designated by small print italicized such as Plot Images under Menu Base/File/Save..... 33
- Figure 4-2. The Execute Base. Execute is the "heart" of NUPROP. Through the Execute Base all NUPROP processes are activated. All the parameters set in the Parameters Base are used to generate the waveforms necessary to simulate nonlinear ultrasound propagation and, consequently, image formation..... 36

Figure 4-3. Example of NUPROP's generation of tissue phantoms. Three elliptical objects are oriented and inter-dispersed within a 256x128 array. The variation determines the regional distinction in the tissue simulation (left bottom image). The nominal levels determine the distinction between regions in the pristine simulation (bottom right image). The pristine image is used strictly for visually cueing of anomalous region(s). This example shows one hypo-echoic region (cyst).....	38
Figure 4-4. Example of NUPROP Widget-Based Graphical User Interface. This example illustrates the basic widget configuration including the radio buttons, parameter input section, display regions, and the status bar.	39
Figure 4-5. Example of statistical analyses from NUPROP ultrasound simulation widget. The left panel displays the simulated images for the fundamental, second and third harmonics, and the phantom along with their respective thresholded images. For this example, a simple threshold level of 40 was used. The upper right panel displays the histogram plots for each simulation image. The lower right panel displays each simulated image's statistics: mean, variance, and skew.....	41
Figure 5-1. Comparison of NUPROP output and data from Ryan, R. P., Ph.D. thesis, Brown University, 1963. The underlying image is data captured from photographing the oscilloscope output at two penetration depths: 5 and 10 cm. The overlaying traces are NUPROP predictions using Fubini (black dotted) and Burgers' (dotted red) under the same (5 cm penetration depth) or similar conditions (9.52 cm vice 10 cm). Note that under conditions prescribed for (b), NUPROP predicts the nonlinear waveform precisely. For condition (c), NUPROP predicts the waveform at the shock distance (9.52 cm), comparing favorably with Ryan's data at 10 cm.	46
Figure 5-2. Comparison of fundamental decay and harmonic growth. Data on the left is from Ryan, R. P., A. Lutsch, and R. T. Beyer, <i>J. Acoust. Soc. Am.</i> , 34, 31, (1962).....	48
Figure 5-3. Comparison of data from Averkiuo et. al. and NUPROP for a P3-2 rectangular geometry transducer on-axis signal strength as a function of propagation distance. The solid line represents Averkiuo's on-axis signal amplitude at the fundamental frequency of 2 MHz, 10 cm focal length, circular transducer with equivalent area to the P3-2 rectangular transducer.....	49

Figure 5-4. Demonstration of difference between circular and rectangular aperture diffraction patterns and its effect on signal strength. As the size of the aperture increases, the maximum signal difference, in percent, slightly decreases: 8 pixels produced a maximum difference of 23.0469%; 16 pixels produced a maximum difference of 22.1680%; 32 pixels produced 21.6553% difference.....	50
Figure 5-5 Comparison of angular spectrum (Red Curves) and Lommel (Black Curve) formulation accuracy. (a) Effects of increasing cross-track resolution on angular spectrum accuracy. (b) Effects of down-range resolution on angular spectrum accuracy.....	51
Figure 5-6. Comparison of NUPROP's Fubini-Angular Spectrum technique with Christopher's NLP Code for trans-axial signal formation (Beam Profile). Conditions: 2 MHz fundamental with harmonic at 4 MHz, P3-2 transducer in water, at 4 cm penetration. The black curves were generated by Christopher's NLP code. The red curves were generated using NUPROP's Fubini-Angular Spectrum Technique.	53
Figure 5-7. Comparison of NUPROP simulation of a point source signal using conditions described in Bamber and Dickinson [1980] and data from Bamber and Dickinson [1980]. The inscribed boundaries (white circle [top] and ellipse [bottom]) are associated with the 3dB, or half power, contours.	54
Figure 6-1. Graphical representation of NUPROP variables. Computational variables govern the size of the computational space allocated for signal and image generation. Environmental variables govern path constituency and attenuation. Object variables govern signal interaction. System variables govern input type, nonlinear and linear propagation modeling types, transducer characteristics, path observation depth, and trace lines for frequency representational graphs. Image of heart from Gray's Anatomy, New York: Bounty Books, p. 467, 1977.	56
Figure 6-2. Illustration of minimizing frequency band overlap to ensure minimum energy cross-over between frequencies. By minimizing the overlaps, the coherent summation of frequency components within the nonlinearly generated signal is valid.....	57
Figure 6-3. Effect of varying B/A ratio on harmonic signal onset distance. B/A ratios range from 5.0 to 12.0, typical range of biological medium (distilled water to fat). Onset distances range	

from 4.7 mm to 3.9 mm for second harmonic signal. Onset distances range from 2.1 cm to 1.7 cm for third harmonic signal.....	59
Figure 6-4. Effect of varying B/A ratio from 5.0 to 12.0, for varying path attenuation, on onset distance for pulsed sinusoid with center frequency of 1.0 MHz, pulse duration of 10 μ s. ..	60
Figure 6-5. Effects of varying path attenuation on onset distance for second and third harmonic signal from a pulsed sinusoid of 1.0 MHz, 10 μ s pulse duration. Note that as path attenuation increases, onset distance decreases in a “pseudo-first order” manner as a function of path attenuation.....	61
Figure 6-6. Effects of varying input signal amplitude on harmonic onset distances. Input signal strength varies from 0.5 MPa to 4.0 MPa. System parameter settings: wave velocity: 1500 m/s; frequency dependent attenuation: 1×10^{-9} dB/cm/MHz; B/A ratio: 7.0; signal frequency: 1.75 MHz; observation distance: 5.25 cm.	62
Figure 6-7. Effects of varying input signal frequency on harmonic onset distance. System parameter settings: wave velocity: 1500 m/s; frequency dependent attenuation: 1×10^{-9} dB/cm/MHz; B/A ratio: 7.0; signal input amplitude: 0.5 MPa; observation distance: 5.25 cm.	63
Figure 6-8. NUPROP Tissue Generation Module. Settings used to generate simulated ultrasound images for sequence in Figure 6-9. Three elliptical objects were generated, forming the complex tissue object. Object 1 is the outer ellipse (white). Object 2 is the small ellipse at a 45 degree angle (black). Object 3 is the inner ellipse (gray).	64
Figure 6-9. Effects of varying center frequency of a narrow-band sinusoidal ultrasound pulse on simulated image formation. Conditions that generated this sequence of images are specified. Frequency was varied from 1.0 MHz to 3.0 MHz. Fundamental (F); Second Harmonic (2); Third Harmonic (3): and Phantom (P).....	65
Figure 6-10. Effects of varying B/A ratio on simulated ultrasound images. The phantom used is shown in upper right corner. Images associated with fundamental, second harmonic, and third harmonic are shown in columns 1, 2, and 3, respectively. B/A ratios of 5, 6, and 10 are rows 1, 2, and 3, respectively. Difference images 5 – 6, 5 – 10, and 6 – 10 are shown in rows 4, 5, and 6, respectively. Difference images are presented in dB.....	67

Figure 6-11. Histogram of Difference images in Figure 6-8. The difference images from Figure 6-7 are redisplayed. The histogram of the fundamental image differences, second harmonic image differences, and third harmonic image differences are presented. The third harmonic difference image histogram shows appreciable distribution, whereas the fundamental and second harmonic difference image histograms essentially show no difference.....	67
Figure 6-12. Effect of varying B/A ratio on signal strength for images generated using 1.75 MHz center frequency, narrowband sinusoid insonification: signal amplitude: 0.5 MPa; observation depth: 4.2 cm; velocity: 1500 m/s; no appreciable frequency dependent attenuation.....	68
Figure 6-13. Effects of varying signal amplitude on image formation. Input signal strengths of 1.0 MPa, 2.0 MPa, and 3.0 MPa were used. System parameters were set as follows: wave velocity: 1500 m/s; B/A ratio: 7.0; observation distance: 2.5 cm; frequency dependent attenuation; 1×10^{-9} dB/cm/MHz.	69
Figure 6-14. Difference images and histograms associated with third harmonics for 1.0, 2.0, and 3.0 MPa signal amplitudes. Differences between fundamentals and second harmonics were negligible. System parameters were set as follows: wave velocity: 1500 m/s; B/A ratio: 7.0; observation distance: 2.5 cm; frequency dependent signal attenuation: 1×10^{-9} dB/cm/MHz.	70
Figure 6-15. Effects of varying wave velocity on image formation. As apparent in the images, very little difference exists between the fundamental and second harmonic images of varying velocities. Differences are manifested in the third harmonic image.	72
Figure 6-16. Difference images and histograms associated with third harmonics for 1400, 1500, and 1600 m/s wave velocities. Differences between fundamentals and second harmonics were negligible.....	72
Figure 6-17. Examples of apodized and non-apodized linear frequency modulated sinusoids. Initial frequency: 1.5 MHz, sweep rate of 1.5×10^{12} . Repeat of Figure 3-2.....	74
Figure 6-18. Illustration of the effects of dispersion or phase shifting and destructive interference on coherently added harmonic signals. Dispersion is indicated within the small circles. In this example, a small phase shift was added to each harmonic signal causing the harmonics to eventually add out of phase, manifested in the destructive interference at the higher frequencies, depicted in the larger circle.....	74

Figure 6-19. Experimental apparatus used to collect chirp signal data. The apparatus consists of a 2.5 MHz transducer acoustically coupled to the wall of the water tank. The hydrophone is attached to a X-Y-Z electronically actuated stage for precise positioning within the water tank (9.5 cm on-axis from the face of the transducer). The signal from the hydrophone and the signal generator are displayed on an oscilloscope. The signals are digitized and sent to a computer for storage (digitizer and computer not shown)	75
Figure 6-20 Comparison of NUPROP's simulated, apodized chirp signal and experimental data. Gray trace is NUPROP simulation, black trace is experimental data.	78
Figure 6-21. Reconstruction of experimental data's chirp constituents. Each constituent chirp is produced by correlating the experimental data with a NUPROP generated apodized chirp: fundamental chirp initial frequency, f_0 : 1.5 MHz with a sweep rate of 2.7×10^{12} , second harmonic chirp beginning at twice f_0 , and the third harmonic at three times f_0	79
Figure 6-22. Comparison of narrowband sinusoid and apodized chirp signal simulate B-scan images with signal to noise ratio of 5×10^9	80
Figure 6-23. Block diagram of potential additive noise sources for an ultrasound imaging system. Noise can be introduced at each electronic device within the image reconstruction process: transmit device, sensing device, oscilloscope, and digitizer.	81
Figure 6-24. Effects of signal to noise ratio on image formation for narrowband sinusoid and apodized chirp. Noise source: signal electronics at the input and output.	82
Figure 6-25. Effect of increasing chirp sweep rate while maintaining appropriate apodization and comparable center to average frequencies.	83
Figure 7-1. Cartoon rendition of beam profile measurement apparatus. Waveform from the signal generator drives the transducer (single frequency sinusoid). The hydrophone is accurately positioned using the computer controlled X-Y-Z stage. The Y-Position is fixed as the X-Position scans in micron steps across the ultrasound beam. Signals from the hydrophone are displayed on an oscilloscope, with further processing and data capture using a signal digitizer and computer (not depicted in this cartoon).	93
Figure 7-2. Illustration of experimental apparatus used for ultrasound B-scan imaging. A transducer is attached to a single stage computer controlled actuator for precision placement along the scan direction. A wire phantom containing several wires spatially displaced is	

insonified. The reflected ultrasound energy is captured by the transducer. The B-scan image is generated from A-line scans of the wire phantom at various points along the scan path.	94
Figure 7-3. Potential wave differential. Region within a few microns has the potential of experiencing a nearly instantaneous velocity differential of $2\dot{X}$	99
Figure 7-4. Snapshots of wave propagating through piecewise homogeneous layer models (Left: without fine structures, Right: with fine structures). The fine structure added to the model on the right is based on actual histological slices of abdominal wall structures. The fine structures introduce considerable diffuse scattering relative to the ideal model.	104
Figure III-1. Linear Chirp Mask. The linear chirp mask is comprised of a "stack" of a given chirp appropriately shifted in the mapped direction as a function of shift in the propagation direction. For this example, every shift in the propagation direction is matched, one for one, by a shift in the mapped direction	120
Figure III-2. Effect of noise on correlation between complex signal and chirp mask. The top graph depicts a complex return signal with no additive noise and its correlation as a function of chirp number. Each peak matches exactly the location in the propagation path of each reflection point. The center graph depicts a noisy return signal and its correlation with the chirp mask. Even under these stressful conditions, the peaks are discernable. The bottom graph depicts an extremely stressful sensing condition: S/N of 0.5. The correlation peaks are essentially obliterated by the noise	121

Chapter 1. Introduction

Medical ultrasound has been a mainstay in noninvasive imaging of the human body. Ultrasound has proven to be a relatively risk free, accurate and versatile technique for clinical diagnostics. Ultrasound allows for real-time images of moving structures and is relatively inexpensive, both features that make ultrasound a desirable imaging modality. Even though ultrasound provides such benefits for medical imaging, two reasons keep ultrasound from being more widely used for quantitative medical diagnostics: first, the interaction of sound with biological tissue is a very complex process, with many parameters that are either assumed constant or measured in a coupled way. A coupled measurement implies that no single parameter can be measured without disturbing or affecting the measure of another parameter. For instance, the measure of absorption depends on acoustic impedance or scattering, in turn, all three are dependent on temperature and temporal frequency of the input signal. The second reason is our lack of knowledge of fundamental interactive processes. One such interaction results in the generation of harmonics and sub-harmonics of the fundamental temporal frequency of the input signal. This phenomenon is known as nonlinearity.

Harmonic energy generation, or nonlinear wave propagation, is frequency dependent, signal amplitude dependent, and is highly susceptible to media attenuation, either through absorption or scattering. It is this susceptibility and subsequent lack of experimentally derived evidence that gave rise to the false assumption that nonlinear effects were not a significant contributor to ultrasound diagnostic imaging. Recent advances in digital architectures, increased dynamic range, and improved signal processing capabilities make it possible to exploit harmonic or nonlinearly generated energy for tissue diagnostics. This thesis provides both a theoretical underpinning and

analytical tool to understanding how nonlinear ultrasound waves are formed, how they propagate, and, more importantly, how they may interact with biological tissue to produce significantly improved ultrasound images.

Experimental verification and validation of the analytical tool (called *Nonlinear Ultrasound PROPagation*: NUPROP) is presented. Results from exercising NUPROP illustrate how this analytical tool can be used to predict fundamental harmonic wave generation properties as well as investigate the influence various systematic, environmental, and object dependent parameters have on image formation.

Chapter 2. Literature Review

This chapter discusses the current literature associated with nonlinear-linear ultrasound wave propagation, namely the generation of nonlinear longitudinal waves using either Burgers' or Fubini's approaches, another nonlinear technique using the K-Z-K equation, linear wave propagation using angular spectrum or the Lommel formulation, and image formation through modeling of the imaging system as a linear, separable function convolved with a continuum of point scatterers describing the medium property of interest. The sections are divided into Nonlinear Wave Propagation, Linear Wave Propagation, Other Approaches, and Image Formation.

Nonlinear Wave Propagation

In his 1997 paper, Christopher discusses the use of computational predictions based on his earlier work, and their application to experimental validation, whereby second harmonics are produced by finite amplitude distortion. Christopher employed a frequency domain solution to Burgers' equation to derive the nonlinear propagation behavior of the medium. Burgers' solution is mathematically developed in Appendix I and described in Chapter 3 as it applies to this research.

Christopher described his experiment wherein he used a concentric ring transducer introducing a sonic waveform. The central portion of the concentric design used a circular disk operating at a 5.0MHz center frequency. The concentric ring surrounding the disk operated at 2.5 MHz and introduced said frequency tone at 1.6 microsecond bursts. Christopher simulated a two-way 2.5 MHz input burst signal and a second harmonic (5.0 MHz) propagated 4.4 cm, with corresponding integrated profiles. Christopher found that the nonlinear parameter, β , was not significant to the

results of his simulations. Christopher then experimentally obtained comparable results for contrast resolution for a scatterer free or cyst region of tissue. His results suggest that a single pulse methodology is sufficient to produce viable, second harmonic generation images.

Krishnan, Hamilton, and O'Donnell [1997] reported that harmonics generated by nonlinear wave propagation in the tissue, the same harmonics that reduce contrast in perfused agent experiments, could be modeled by a Taylor series expansion of the equation of state for plane waves in liquid media under adiabatic conditions. Their approach directly applied Christopher and Parker [1991] mathematical concepts and laboratory experimentation to modeling contrast agent image enhancement. Their approach to describing the nonlinear effect employed the nonlinear ratio, B/A . A and B are the coefficients associated with the first two terms of a Taylor series expansion of the state equation. The equation of state is given as

$$p - p_o = A \left(\frac{\rho - \rho_o}{\rho_o} \right) + \frac{B}{2} \left(\frac{\rho - \rho_o}{\rho_o} \right)^2 \quad (2-1)$$

where p and p_o are pressure and static pressure, respectively and ρ and ρ_o are density and static density, respectively.

Krishnan, *et. al.*, [1997] developed a method of studying harmonic cancellation, whereby the second harmonic was obtained through the use of a frequency solution to Burgers' equation (Haran and Cook [1983]; Trivett and Buren [1984]). Krishnan, *et. al.*, [1997] used an incremental step approach whereby the wavefront was propagated a distance, z_1 , by performing a linear propagation followed by a nonlinear propagation. The linear propagation accounted for each frequency component while the nonlinear propagation accounted for the generation of harmonics and sub-harmonics. Linear propagation was accomplished by decomposing the signal into an angular spectrum of plane waves (described later in the section on angular spectrum). Nonlinear

propagation was accomplished, as previously mentioned, using a frequency domain solution to Burgers' equation. The solution takes on the following form

$$u_n(z + \Delta z, i) = u'_n(z + \Delta z, i) + j \frac{\beta \pi f \Delta z}{2c^2} \left(\sum_{k=1}^{n-1} k u'_k(z + \Delta z, i) u'_{n-k}(z + \Delta z, i) + \sum_{k=n}^N u'_k(z + \Delta z, i) u'_{k-n}(z + \Delta z, i)^* \right),$$

$$n = 1, 2, \dots, N.$$
(2-2)

where $u_n(z + \Delta z, i)$ is the n^{th} temporal frequency component of the normal velocity waveform at the i^{th} azimuthal point in space at a depth, $z + \Delta z$, and $u'_n(z + \Delta z, i)$ is the same temporal frequency component of the waveform prior to nonlinear propagation. The variable, β , is a function of the nonlinear ratio, B/A , as $\beta = 1 + \frac{B}{2A}$. The variable f is the center frequency of the propagating waveform and c is sound speed in the medium. Krishnan, *et. al.*, did not consider attenuation in their development.

Another technique for describing nonlinear wave behavior was developed by Fubini [1935], where he derived an explicit solution to the equation for motion of plane sound waves in a gas. Derivation of the Fubini solution is given in Appendix II and described, in greater detail, in Chapter 3 relative to its application in this research. Important features of the Fubini solution are

1. A slope term in the denominator that reaches negative infinity at a finite propagation distance known as the shock distance. Computation beyond this point produces invalid results
2. The fundamental component signal amplitude of the wave will decrease as the wave propagates, harmonic component signal amplitudes increase
3. As initial wave amplitude increases, shock distance will decrease

4. As frequency increases, the shock distance will decrease
5. The ratio, u/u_o , can be viewed as appropriately weighted sum of frequency dependent, sinusoidal basis functions

Linear Wave Propagation

Lewin [1989] provided a more detailed description of the angular spectrum technique. His aim was to provide an analytical means of predicting transducer performance. His assessment of the advantages of using the angular spectrum technique included high spatial resolution, computational efficiency using the FFT, and the method's applicability to both forward and back propagation. Lewin's derivation of the angular spectrum method is repeated in the following: Note: this derivation can be found in several references Goodman [1968]; Stepanishen and Benjamin, [1982]; Powers [1976]:

A complex pressure wave field is generated by a set of monochromatic sources. A wave field is represented as $u(x, y, z_o)$ in a plane parallel to the X - Y plane at a position z_o as depicted in Figure 2-1.

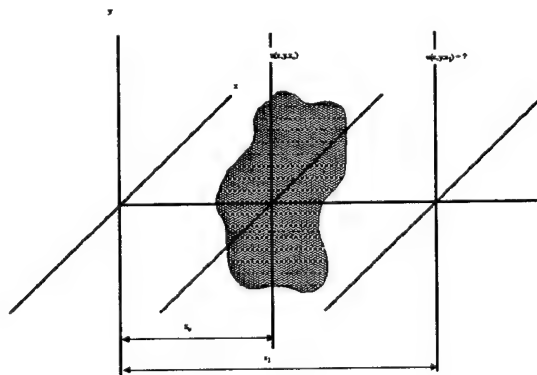


Figure 2-1. Graphical representation of a complex pressure field propagating from one parallel plane to another using the angular spectrum technique.

The two-dimensional Fourier transform of this complex pressure wave field is represented as $U(\xi, \eta, z_0)$. Each complex field frequency is modified by an appropriate phase factor as it propagates from its original position (z_0) to a new position (z_1). This accounts for a plane wave propagating from z_0 to z_1 . The phase factor can be represented as

$$G(\xi, \eta, z_0, z_1) = e^{i2\pi(z_1-z_0)\sqrt{\lambda^{-2}-\xi^2-\eta^2}} \quad (2-3)$$

Consequently, the field at z_1 can be represented as

$$u(x, y, z_1) = \iint U(\xi, \eta, z_0) \cdot e^{i2\pi(z_1-z_0)\sqrt{\lambda^{-2}-\xi^2-\eta^2}} \cdot e^{i2\pi(\xi x + \eta y)} d\xi d\eta \quad (2-4)$$

where λ is the temporal wavelength of the propagating wave field, ξ and η are the angular spatial frequencies associated with the x and y coordinates, respectively, and $U(\xi, \eta, z_0)$ is the Fourier transform of the complex field at z_0 . Essentially, the propagation of a complex field at z_0 to a position, z_1 , can be modeled as a space-invariant filter in the frequency domain. Notably, if λ^2 is greater than $\xi^2 + \eta^2$, then the phase term is purely imaginary giving rise to harmonic wave propagation. Whereas, if the converse is true, then the phase factor is real, yielding strong attenuation in the positive z -direction.

Lewin handled evanescent waves in the back-propagation direction by nulling them out prior to back-propagation calculations, thus the evanescent waves had no contribution to the return or reflected signal. Lewin also assumed that the medium acted on the propagating wave the same irrespective of propagation direction. Lewin's application of the angular spectrum technique was strictly linear.

Daly and Rao [1998] proposed a closed form frequency domain formalism whereby spatially integrated diffraction corrections were employed. The Lommel diffraction formulations were used as a "coupled-pair" or approximate Fourier transform pairs, amenable to closed-form spatial

integration, deriving an exact diffraction solution for a circular piston transducer geometry. As Daly and Rao point out, diffraction corrections are necessary when trying to characterize biological tissue using ultrasound, especially in the near field, sometimes inappropriately referred to as the Fresnel region. Lommel functions are defined as follows:

$$U_n(u, v) = \sum_{s=0}^{\infty} (-1)^s \left(\frac{u}{v} \right)^{n+2s} J_{n+2s}(v) \quad (2-5a)$$

$$V_n(u, v) = \sum_{s=0}^{\infty} (-1)^s (n+2s) \left(\frac{v}{u} \right)^{n+2s} J_{n+2s}(v) \quad (2-5b)$$

Since the Lommel functions are infinite summations, they can only be approximated numerically. In the Fresnel approximation, and imposing circular symmetry, the velocity potential, $H_1(\rho, z, \omega)$, can be approximated as

$$H_1(\rho, z, \omega) \approx \hat{H}_1(\rho, z, \omega) = \frac{1}{z} e^{-ik(z + \frac{\rho^2}{2z})} \int_0^a e^{ik \frac{\rho_0^2}{2z}} J_0\left(\frac{k\rho}{z} \rho_0\right) \rho_0 d\rho_0 \quad (2-6)$$

where $\rho_0 = \sqrt{x_0^2 + y_0^2}$ is the off-axis distance at $z = 0$, plane, $\rho = \sqrt{x^2 + y^2}$ is the off-axis at the z plane, a is the aperture diameter, and the hat indicates estimation. Invoking the singularity function with a change of upper limit integration (equal to infinity), then (2-6) can be interpreted as the Hankel transform of the product of the singularity function and a quadratic phase term, rewriting (2-6) as

$$\hat{H}_1(\rho, z, \omega) = \frac{1}{z} e^{-ik(z + \frac{\rho^2}{2z})} \left[\frac{a}{\rho} J_1\left(\frac{ka\rho}{z}\right) * \frac{1}{i} e^{ik \frac{\rho^2}{2z}} \right] \quad (2-7)$$

where the convolution is now with respect to $k\rho/z$, with the closed form solution given as

$$\hat{H}_1(\rho, z, \omega) = \frac{1}{k} e^{-i\left(kz + \frac{v^2}{2u} + \frac{u}{2}\right)} [U_1(u, v) + iU_2(u, v)] \quad (2-8)$$

with $u = ka^2 / z$ and $v = ka\rho / z$.

Oberhettinger [1961] developed exact expression for the inverse Fourier transform of H_1 given as

for $\rho < a$

$$h_1(\rho, z, t) = \begin{cases} 0, & ct < z \\ c, & z < ct, R' \\ \frac{c}{\pi} \arccos \left[\frac{(ct)^2 - z^2 + \rho^2 - a^2}{2\rho\sqrt{(ct)^2 - z^2}} \right], & R' < ct < R \\ 0, & ct > R \end{cases} \quad (2-9)$$

for $\rho > a$

$$h_1(\rho, z, t) = \begin{cases} 0, & ct < R' \\ \frac{c}{\pi} \arccos \left[\frac{(ct)^2 - z^2 + \rho^2 - a^2}{2\rho\sqrt{(ct)^2 - z^2}} \right], & R' < ct < R \\ 0, & ct > R \end{cases} \quad (2-10)$$

where $R' = \sqrt{z^2 + (a - \rho)^2}$ and $R = \sqrt{z^2 + (a + \rho)^2}$. With significant manipulation and invocation of relationships developed by Wolf [1953]; Daly [1998], the spatially integrated, estimation of the Fourier domain representation of the velocity potential is given as

$$\langle \hat{H}_1(z, \omega) \rangle_a = \frac{-2\pi z}{k^2} e^{-i\left(kz + \frac{u}{2}\right)} \cdot \left\{ i \frac{u}{2} e^{i\frac{u}{2}} + e^{-i\frac{u}{2}} \left[\frac{u}{2} J_1(u) - i \frac{u}{2} J_0(u) \right] \right\} \quad (2-11)$$

where $u = ka^2 / z$, a Fresnel distance normalized wavenumber.

Other Approaches

Nikoonahad and Iravani [1989] incorporated a complex, frequency dependent compressibility into the wave equation to predict the focal plane distribution in biological media. Their approach

employs a complex, frequency dependent wavenumber derived from ultrasonic propagation given by

$$\nabla^2 u - \rho \bar{k} \frac{\partial^2 u}{\partial t^2} = 0 \quad (2-12)$$

where \bar{k} is a complex wavenumber defined by O'Donnell [1981] as

$$\begin{aligned} \bar{k} &= k_1(\omega) + ik_2(\omega) \\ k_1(\omega) &= \frac{1}{\rho c_r^2} \left(\frac{c_r}{c(\omega)} \right)^2 \\ k_2(\omega) &= \frac{2\alpha(\omega)}{\rho \omega c(\omega)} \end{aligned} \quad (2-13)$$

where $c(\omega)$ and $\alpha(\omega)$ are phase velocity and absorption coefficient, respectively. The subscript on c refers to the phase velocity at reference frequency, ω_r . Nikoonahad and Iravani state that the absorption coefficient must exhibit two properties:

1. Nearly linear dependence on frequency
2. A square law dependence on frequency in liquids where relaxation times are short.

Nikoonahad and Iravani reported that Seghal and Greenleaf [1982] used these two properties and formulated

$$\begin{aligned} \ln \left(\frac{c(\omega)}{c_r} \right) &= \frac{2 \ln(\gamma)}{\pi} \ln \left(\frac{A(\omega) + B(\omega)}{A(\omega_r) + B(\omega_r)} \right) \\ \alpha(\omega) &= \frac{2\omega A(\omega) \ln(\gamma)}{c(\omega) B(\omega)} \\ A(\omega) &= \omega \tau \\ B(\omega) &= \sqrt{1 + (\omega \tau)^2} \end{aligned} \quad (2-14)$$

For these relationships, γ is the specific heat ratio and τ is the relaxation time. By substituting these relationships into the previous equation, the following relationships for k_1 and k_2 are derived

$$\begin{aligned}
k_1(\omega) &= \frac{1}{\rho c_r^2} \left(\frac{A(\omega_r) + B(\omega_r)}{A(\omega) + B(\omega)} \right)^{(4 \ln \gamma)/\pi} \\
k_2(\omega) &= \frac{4A(\omega) \ln \gamma}{\rho c_r^2 B(\omega)} \left(\frac{A(\omega_r) + B(\omega_r)}{A(\omega) + B(\omega)} \right)^{(4 \ln \gamma)/\pi}
\end{aligned} \tag{2-15}$$

Both k_1 and k_2 account for dissipative (absorption) and dispersive (frequency dependent attenuation) processes within biological media. It is this complex wavenumber that is introduced into a three-dimensional Fourier transform, where the angular dimensions are x and y , and the third dimension is time, t . Nikoonahad and Iravani then employed the traditional angular spectrum technique to linearly propagate the transverse wavefront, using the complex, frequency dependent wavenumber as a modifier for the propagation term. Unfortunately, this approach is strictly linear and does not account for harmonic component generation.

Averkiou, Roundhill, and Powers [1997] proposed a different mathematical approach employing the Khokhlov-Zabolotskaya-Kuznetsov (KZK) equation developed by Zabolotskaya and Khokhlov [1969]; Kuznetsov [1970]. The KZK relationship accounts for diffraction, absorption, and nonlinearity. Averkiou, *et. al.*, concluded that, since tissue properties were readily available in literature, including coefficients for nonlinearity, this tissue property could be modeled using the KZK equation. The KZK model is given as

$$\frac{\partial^2 p}{\partial z \partial t} = \frac{c_o}{2} \nabla_r^2 p + \frac{\delta}{2c_o^3} \frac{\partial^3 p}{\partial t^3} + \frac{\beta}{2\rho_o c_o^3} \frac{\partial^2 p^2}{\partial t^2} \tag{2-16}$$

where p is the sound pressure, z is the coordinate along the propagation direction,

$\nabla_r^2 = \frac{\partial^2}{\partial r^2} + \frac{1}{r} \frac{\partial}{\partial r}$, r is the angular radial coordinate (assuming axial symmetric sound beam),

$t = t' - \frac{z}{c_o}$ the retardation time, and c_o is the sound speed. The first term on the right-hand side

of this relationship accounts for diffraction; the second term accounts for thermoviscous attenuation or dissipation where δ is the diffusivity of sound Lighthill [1980]; the third term accounts for nonlinearity, where β is given as $1 + \frac{B}{2A}$ Beyer [1960]. One limitation of this approach is the requirement for a directive sound source where $ka \gg 1$, k being the wavenumber associated with the source and “ a ,” the radius of the source. Another limitation is the paraxial approximation, thus limiting the validity of solutions to regions around the axial direction. Although the KZK equation is not universal, it does provide good agreement with experiments adhering to these restrictions Averkiou and Hamilton [1997]; Baker and Humphrey [1990]; Baker, Berg, and Tjøtta [1997].

Image Modeling

Image formation is generally divided into two main tasks: modeling the imaging system and modeling the tissue. Most simulations assume a constant velocity throughout the propagation medium, zero attenuation, zero noise level, infinite receiver bandwidth, and linear gain characteristics of the receiver. An excellent example of this type of simulation was developed by Bamber and Dickinson [1980]. Bamber assumed that the system forming the image had a linear, separable, space invariant point spread function, with the tissue or other object represented by a continuous distributed set of point scatterers. Bamber’s assumptions then yielded an image, $I(x,y)$, using the convolution (denoted \otimes) of the system point spread function, $H(x,y)$ and the set of point scatterers, $T(x,y)$

$$I(x,y) = H(x,y) \otimes T(x,y) \quad (2-17)$$

Pulse echo imaging is a tomographic technique that differs from conventional imaging in a number of respects: signal beam is coherent and the detector is phase sensitive. This will significantly

impact the image reconstruction since return signals from differing locations will interfere, giving rise to classical speckle effects. Bamber's model neglected multiple scattering. Additionally, Bamber's model assumed non-axial symmetry such that the point spread function consists of two, separable convolution filters: one for the longitudinal pulse shape and the other for the trans-axial beam profile such that $H(x,y)$ from equation 2-17 becomes $H_2(x,1)$ and $H_1(1,y)$ yielding

$$I(x,y) = H_2(x,1) \otimes H_1(1,y) \otimes T(x,y) \quad (2-18)$$

Convolution with $H_2(x,1)$ equated to detection if x was the longitudinal direction while convolution with $H_1(1,y)$ equated to smoothing or diffraction if y was the trans-axial direction.

As previously mentioned, Bamber's model depended on describing the medium as a continuous distribution of point scatterers, or the acoustic impulse response of the tissue. One popular tissue model used by Bamber was the inhomogeneous continuum models of Chivers [1977], Gore and Leeman [1977], and Nicholas [1977] in which the density, ρ , and compressibility, β , of the tissue were modeled as continuous and fluctuated about their mean value. Fields and Dunn [1973], however, neglected density fluctuations opting for compressibility fluctuations only. Bamber suggested that, if the medium was considered comprised of a continuum of elemental scatterers within an inhomogeneous medium, and the density term being neglected, then the source strength of each elemental scatterer was proportional to the second derivative of the compressibility at each elemental position in the medium. This is an important concept because, if the spatial distribution of the tissue compressibility is known, then the required tissue impulse response can be derived such that

$$T(x,y,z) = \nabla^2 \beta(x,y,z) \quad (2-19)$$

Bamber further stipulated that $\beta(x,y)$ had to be purely real, constraining the real spectrum to be an even function of frequency and the imaginary spectrum to be an odd function of frequency. After obtaining the compressibility matrix values, Bamber then formed images by simply multiplying the Fourier domain representation of the compressibility matrix by s^2 .

Chapter 2: Summary

The literature is replete with examples of ultrasound modeling techniques that capture aspects of the overall process. For nonlinear wave propagation, two models are prominent: Christopher's and Parker's NLP and the Khokhlov-Zabolotskaya-Kuznetsov (KZK) implementation. Christopher's NLP is based on solutions to Burgers' equation and is implemented using a C-based code. Averkiou's Implementation of the K-Z-K includes diffraction, attenuation, and nonlinearities in a single, third order partial differential equation.

For linear propagation, two methods are presented: angular spectrum and Lommel formulation. Angular spectrum implements a planar geometry derived mathematical convention using a propagation factor that accounts for complex field changes over small incremental distances. Since angular spectrum is developed using planar calculus, focused beam geometries are not easily accommodated.

Angular spectrum is applicable throughout the propagation path, from just in front of the transducer to as far as the user wished to compute the field. Additionally, angular spectrum is suitable for computing field propagation from non-radially symmetric geometries.

Lommel formulation implements planar as well as focused beam transducer geometries. However, Lommel is applicable for circularly symmetric geometries only. Additionally, Lommel is strictly a linear propagation process. Therefore, any process that introduces nonlinearities, i.e. generation of harmonics, will necessarily be inaccurately predicted by Lommel.

Ultrasound image generation models depend strongly on the tissue characterization or tissue construction model used. One model has found considerable favor in literature: Bamber and Dickinson's continuous array of point scatterers. If the tissue characteristic of interest can be modeled as an array of continuous point scatterers, then Bamber's technique is reasonably accurate in predicting linear ultrasound effects. Bamber's technique involves the convolution of the tissue array with the point spread function of the ultrasound pulse. Bamber accomplishes the convolution by taking the process to the Fourier domain and multiplying the Fourier transforms of the tissue array and the point spread function, then inverse Fourier transforming the product.

Though models exist for the various aspects of the ultrasound process, no single model encompasses all aspects of ultrasound propagation and, ultimately, ultrasound imaging. In this work, a new model, Nonlinear Ultrasound Propagation (NUPROP), is introduced that captures aspects of nonlinear wave generation and propagation, linear wave generation and propagation, and image generation.

Chapter 3. NUPROP Module Development

This chapter discusses the main modules comprising NUPROP: 1) phantom generation, 2) input signal waveform type (sinusoid or chirp), 3) implementation of wave propagation - Nonlinear: Burgers' Equation and Fubini Solution, and Linear: Angular Spectrum and Lommel, 4) image generation using the Hilbert transform, and 5) post processing such as statistical analyses.

Phantom Generation: Continuous Point Scatterer Array

The validity of simulating ultrasound images relies on the ability to describe the object or tissue as a continuous array of point scatterers: a model of the acoustic impulse response of the tissue. This view of modeling tissue characteristics is supported by the theory of scattering from an inhomogeneous medium. Phantoms can be represented mathematically as

$$Ph(x, y, z) = A(x, y, z) - \bar{A} \quad (3-1)$$

where $A(x, y, z)$ is the amplitude of the acoustic impedance at a point in space, \bar{A} is the mean value of the array, with $A(x, y, z)$ computed using

$$A(x, y, z) = \sum_n \alpha_n RANDOMU(seed, x_n, y_n, z_n) \quad (3-2)$$

given α_n is the n^{th} object's acoustic impedance value at position x_n, y_n, z_n , $RANDOMU$ is a uniformly distributed random number generating function, and $seed$ is a temporally changing value to initiate the generation of a random number. If $seed$ is not specified, then the algorithm will use the computer's clock to generate a $seed$ value. The mean value is subtracted from the array composite to eliminate any artificial discontinuities introduced by the phantom generation algorithm.

Waveform Type

Single Frequency Sinusoid

Since a single frequency is equivalent to a continuous wave input, it has little to no use in imaging, since the return signals cannot be distinguished from one point scattering position to another. However, the single frequency sinusoidal input is useful in comparing NUPROP's nonlinear wave propagation performance against existing data in literature (Ryan's Fubini solution, Christopher's trans-axial beam profiles, and Averkiu's along-track or longitudinal beam amplitude profile).

Narrowband Frequency Sinusoid

The narrowband or pulsed sinusoidal input is typically used for image generation (B-scan). The narrowband sinusoidal input requires care in constructing the pulse or temporal apodization function. Whether the pulse apodization is frequency dependent or not, the temporal extent must be such as to produce minimal frequency domain overlap of the bands about the harmonics. Figure 3-1 illustrates this condition. Note that the frequency dependent apodization curves have greater overlap than the frequency independent curves.

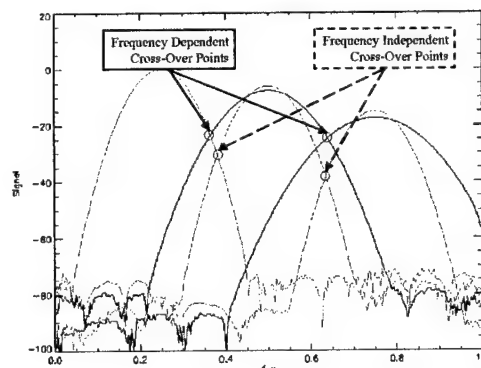


Figure 3-1. Frequency dependent and independent apodization schemes for ensuring minimum overlap of frequency signals: fundamental, second, and subsequent harmonics. The signal is presented in dB scale. The fundamental frequency is arbitrarily set to 2.5 MHz, with second and third harmonics shown at 5.0 MHz and 7.5 MHz, respectively. The apodization functions are Gaussian with exponent 2.

Linear Frequency Modulated Sinusoid (Apodized and Non-Apodized)

Another multiple frequency signal input is the linear frequency modulated sinusoid more commonly called the "chirp." Arguably one of the most useful linear filtering techniques is the use of the quadratic phase filter or chirp. The primary advantage of using a chirp signal over a single frequency sinusoid, or apodized sinusoid, is the ability to have a very wide bandwidth, infinite in fact, while maintaining reasonable signal gain (or signal to noise ratio). Figure 3-2 shows both the apodized and non-apodized chirp signal for start frequency of 1.5 MHz, sweep rate of 8.5×10^{10} . The apodization used for the chirp ensures minimum overlap of frequency harmonic bands.

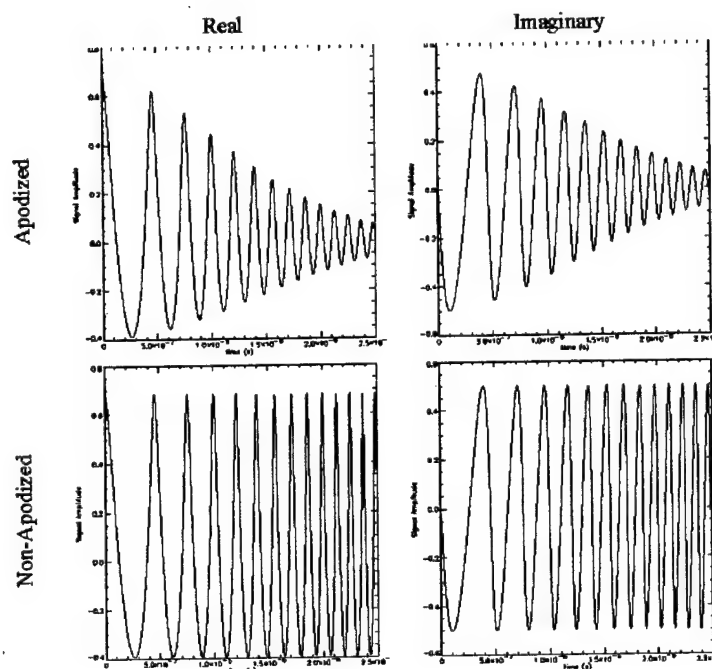


Figure 3-2. Examples of apodized and non-apodized linear frequency modulated sinusoids. Initial frequency: 1.5 MHz, sweep rate of 1.5×10^{12} , and apodization to ensure minimum harmonic signal overlap. Note that the chirps represented here consist of the fundamental and 10 harmonics of the initial frequency.

The non-apodized chirp input signal has the same diagnostic advantages as the single frequency sinusoid, but suffers the same non-imaging capability. The apodized chirp possesses the imaging capability, but suffers strict apodization requirements to ensure minimum overlap. These restrictions may prove to be too stringent so as to negate the apodized chirp's inherent

processing advantage: improved signal to noise ratio without necessary bandwidth reduction. The development of NUPROP's implementation of the chirp is given in Appendix III.

Wave Propagation: Nonlinear

Burgers' Equation Model

The Burgers' equation models the effect of wave shearing in viscous and non-viscous media. The Burgers' relationship can be represented as a second order, non-linear partial differential equation as follows:

$$\frac{\partial u}{\partial t} + u \cdot \frac{\partial u}{\partial z} - \nu \cdot \nabla^2 u = 0 \quad (3-3)$$

where u represents a complex wave field and ν is the viscosity of the media. Solutions to the Burgers' equation are of the form $u = f(\omega t - kz)$ where k is the wavenumber, z is the propagation direction, ω is the wave frequency, and t is time. Blackstock, as referenced in Beyer and Letcher [1969] developed a closed form solution to Burgers' equation given as

$$\frac{u}{u_0} = \frac{4\alpha c_o^2}{\alpha(1+B/2A)} \frac{\sum_{n=1}^{\infty} (-1)^{n+1} n I_n\left(\frac{1}{4\alpha l}\right) e^{-n^2 \alpha} \sin[\omega t - kz]}{I_0\left(\frac{1}{4\alpha l}\right) + 2 \sum_{n=1}^{\infty} (-1)^n I_n\left(\frac{1}{4\alpha l}\right) e^{-n^2 \alpha} \cos[\omega t - kz]} \quad (3-4)$$

where α is the effective absorption coefficient, c_o is the wave speed, ω is the wave frequency, $(1+B/2A)$ is the nonlinear parameter, k is the wavenumber, l is the shock distance (see 3-8), or discontinuity distance as described in the Fubini Solution section of this chapter, and I_n is the Bessel function of order n of the imaginary argument

$$I_n(z) = i^{-n} J_n(iz) \quad (3-5)$$

Fubini Solution Model

Another technique for describing nonlinear wave behavior was developed by Fubini [1935], where he derived an explicit solution to the equation for motion of plane sound waves in a gas

$$\frac{\partial^2 \xi}{\partial t^2} = \frac{c_o^2}{(1 + \partial \xi / \partial a)^{\gamma+1}} \frac{\partial^2 \xi}{\partial a^2} \quad (3-6)$$

as

$$\frac{u}{u_o} = 2 \sum_{n=1}^{\infty} \frac{J_n(nz/l)}{nz/l} \sin[n(\omega t - kz)] \quad (3-7)$$

A discontinuity will occur when the denominator term of (3-6), $\partial \xi / \partial a$, becomes infinitely negative. This “slope” term must approach negative infinity at some propagation distance due to the fact that large values of u will propagate faster than small values of u , thus giving rise to wave distortions. This phenomenon is commonly referred to as a “shock front.” Fubini computed this distance from the origin to the point where the shock forms as

$$l = \frac{c_o^2}{(B/2A + 1)\omega u_o} \quad (3-8)$$

Appendix II describes the mathematical development of this closed form solution to Fubini’s equation.

Up to this point, all solutions have been for continuous or undamped, single frequency sinusoidal input. A more common ultrasound imaging modality is the pulsed sinusoidal signal, whereby a single frequency drive signal is modified using an envelope or temporal windowing function. Such a drive signal can be expressed as

$$f(z,t) = g(z,t) \cdot \sin(\omega t - kz) \quad (3-9)$$

where $g(z,t)$ describes the windowing function. A typical windowing function would be a Gaussian. By “windowing” the sinusoidal, the input signal is no longer single frequency but rather

a “band” of frequencies centered on the fundamental. If more than one frequency exists in the drive signal, then each component must be modified by an appropriately frequency scaled Gaussian to account for this frequency “broadening.” If sufficient separation exists between multiple frequencies, then a reasonable approximation to the overall signal would be a simple modification of (3-7) to include the frequency dependent apodization terms such that

$$\frac{u}{u_o} = \sum_{n=1}^{\infty} \frac{2l}{nz} J_n\left(\frac{nz}{l}\right) \sin[n(s)] \cdot e^{-\pi \frac{(s)^2}{\sqrt{2}\alpha\omega\sigma_n}} \quad (3-10)$$

where α is an engineering scaling function to ensure sufficient localization of energy about each frequency term, σ_n is the frequency dependent standard deviation, and s is $\alpha t - kz$.

Wave Propagation: Linear

Angular Spectrum Model

Linear propagation is accomplished in NUPROP one of two ways: Angular Spectrum or Lommel Formulation. This section discusses NUPROP’s implementation of Angular Spectrum. As previously discussed, angular spectrum is a technique whereby a planar wavefront can be translated along a propagation path, usually denoted as the z -direction, in incremental steps. NUPROP assumes the pressure amplitude is known at the source or excitation field position designated $z = 0$. Goodman [1968, ch. 3] described the angular spectrum as the Fourier transform of the pressure field with respect to x and y , given values of the pressure field in the x - y plane at a distance, z . Defining the pressure field as $p(x,y,z)$, then its angular spectrum is given as

$$P(\xi, \eta, z) = \iint p(x, y, z) e^{-i2\pi(\xi x + \eta y)} dx dy \quad (3-11)$$

The relationship between $P(\xi, \eta, z)$ and $P(\xi, \eta, 0)$ comes from the fact that $p(x,y,z)$ obeys the Helmholtz equation $(\nabla^2 + k^2)p = 0$, where $k = 2\pi/\lambda$ is the wavenumber, resulting in

$$P(\xi, \eta, z) = P(\xi, \eta, 0)H(\xi, \eta, z) \quad (3-12)$$

where $H(\xi, \eta, z)$ is defined as the space-invariant propagation filter

$$H(\xi, \eta, z) = e^{ikz\sqrt{1-\lambda^2(\xi^2+\eta^2)}} \quad (3-13)$$

$$= \begin{cases} e^{ikz\sqrt{1-\lambda^2(\xi^2+\eta^2)}}, & \text{for } \xi^2 + \eta^2 \leq \frac{1}{\lambda^2} \\ e^{-kz\sqrt{\lambda^2(\xi^2+\eta^2)-1}}, & \text{for } \xi^2 + \eta^2 > \frac{1}{\lambda^2} \end{cases}$$

By inspection, if $\xi^2 + \eta^2 \leq \frac{1}{\lambda^2}$, then the wave propagates with an amplitude of unity in the absence of attenuation. If $\xi^2 + \eta^2 > \frac{1}{\lambda^2}$, then the wave exponentially decays with propagation.

This exponentially decaying wave is called an evanescent wave. Evanescent waves decay within a few wavelengths of propagation so they are typically ignored for simulation purposes.

Again, by inspection, if the wavefront is backpropagated from an array of known data, then the evanescent wave will grow exponentially, since, by convention, the sign of the exponent is positive. Typically, the evanescent wave is set to zero prior to backpropagation or the sign of the exponent is set negative to account for evanescent waves decaying in actual tissue. NUPROP's implementation of angular spectrum assumes planar apertures.

Lommel Formulation

This section discusses the development of Lommel formalism relative to NUPROP's implementation. As Daly and Rao have determined, the Lommel formulation is a closed-form estimate of the Fourier transform of the arccos diffraction formulation and can be used to determine the wavefront characteristics at a propagation distance from an extended source. The Lommel-based formalism allows the direct calculation of diffraction effects in the frequency

domain, in the absence of nonlinearities. NUPROP uses Daly's IDL code to compute on-axis amplitudes for circularly symmetric apertures.

Image Generation

The wave equations used for generating nonlinear ultrasound waves (*see section on nonlinear wave propagation*) represent the incident wave. Bamber [1980] computes the signal amplitude at any image point from the received voltage by transforming time dependence to distance dependence, deriving the equation describing the image formation as

$$I(x, y, z) = \int a(2x' - 2x) b(y - y', z' - z) T(x', y', z') d^3 r \quad (3-14)$$

where $I(x, y, z)$ is the image, a is the pulse shape, b is the pulse-echo beam profile, and T is the tissue impulse response given as

$$T(r) = \frac{1}{4} \frac{\partial^2}{\partial z^2} \left(\frac{\rho_1(r)}{\rho_o} - \frac{\beta_1(r)}{\beta_o} \right) \quad (3-15)$$

where $\rho_1(r)$ is the spatial density, ρ_o is the static density, $\beta_1(r)$ is the spatial compressibility, and β_o is the static compressibility. This relationship holds true provided the wavelength of the incident pulse is much smaller than the pulse length or the beam width. The image amplitude distribution, then, is a convolution between the tissue impulse response and the pulse-echo point spread function. So, NUPROP computes harmonic component contributions at each penetration depth using nonlinear processes (longitudinal pulse profile), coupling those processes with the linear propagation to compute the angular or trans-axial beam profiles at those penetration depths, then convolves the resulting function (a three dimensional wave function) with the phantom point scatter array at each position. The result of the convolution produces the RF signal for a given simulation. B-Scan images are then generated using conventional envelope detection via the

Hilbert transform. Typically, ultrasound is used clinically in a pulsed mode, a short duration temporal “burst” of ultrasonic energy. The pulse then travels a distance into the medium, reflects off the object of interest, returning to the same transducer that produced the pulse. The transducer is now “switched” to receive mode, detecting the return echoes from reflections within the medium. The time taken between initial pulse and return signals constitutes the collected data. The intensity of the echoes is also recorded, and is used when rendering the scans.

The pulse returns are converted into weak voltage signals proportional to the echo intensity. The converted echo signals are conditioned through a series of electronic circuits:

1. limiter designed to prevent excessively large transient voltage signals to damage the receiver electronic circuitry,
2. a logarithmic amplifier to boost the weak signal amplitudes (as much as 100 dB),
3. a rectifier to convert negative half-cycles of the echo signals into positive half-cycles,
4. a demodulator to remove the carrier frequency, leaving only the magnitude envelope of the echo signal.

Envelope detection is typically performed on the fundamental frequency carrier. The demodulator performs a Hilbert transform on the data to produce the envelope detection. The Hilbert Transform provides a 90 degree phase shift to its input. If $x(t)$ is the real input signal, and the Hilbert transformed signal is $h(t)$, then the analytic signal is:

$$z(t) = x(t) + ih(t) \quad (3-16)$$

If the analytic signal possesses a single frequency, then the amplitude, $A(t)$, of the waveform can be represented as the square root of the squared magnitude such that

$$A(t) = \sqrt{z(t) \cdot z(t)^*} = [(x(t) + ih(t)) \cdot (x(t) - ih(t))]^{1/2} = \sqrt{x(t)^2 + h(t)^2} \quad (3-16)$$

where $z(t)^*$ represents the complex conjugate of $z(t)$.

Figure 3-3 graphically illustrates NUPROP's modular design and processes for simulating nonlinear ultrasound waves and image generation.

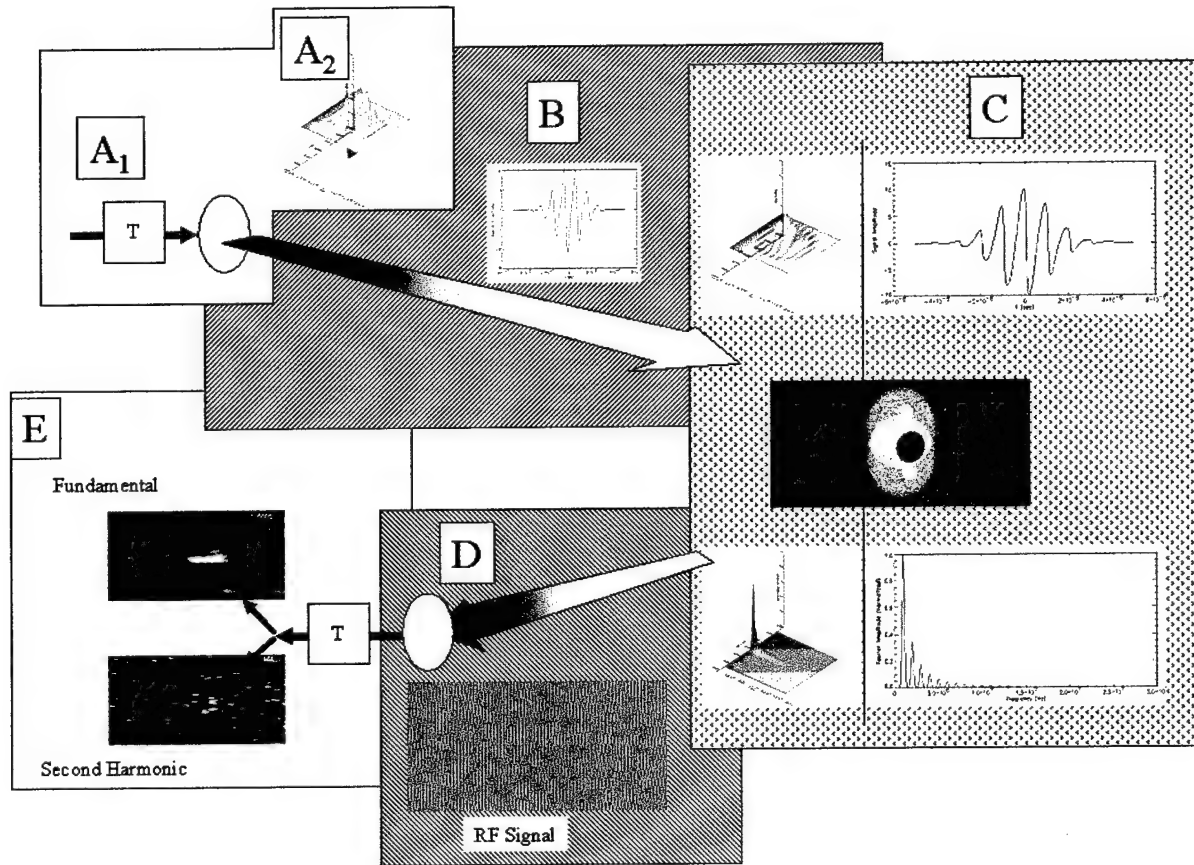


Figure 3-3. Modular design and processes associated with NUPROP: Nonlinear Ultrasound Propagation Modeling. A) Transducer Effects and Input Waveform Generation. B) Nonlinear – Linear Coupled Wave Propagation. C) Wave – Object Interaction and Phantom Generation. D) Linear Propagation. E) Transducer Effects and Image Simulation.

A_1 introduces transducer effects to the input signal. The transducer is modeled as function that introduces beam spatial and temporal shaping. The spatial beam shaping is simple: circular or rectangular geometry, unit amplitude within the boundaries defined by the geometry, non-focused. The temporal beam shaping is simple as well: Gaussian with exponent varying from two to six. Gaussian temporally apodizing functions with exponent of 3 or more are called “Super-

Gaussian” and are characterized by sharper fall-offs approaching the Rect function defined as follows:

$$f(t) = RECT(t) \cong \lim_{n \rightarrow \infty} e^{-\pi|2t|^n} = \begin{cases} 1 & \text{for } |t| < 0.5 \\ 0.5 & \text{for } |t| = 0.5 \\ 0 & \text{otherwise} \end{cases} \quad (3-17)$$

A_2 depicts the pulse “wave-packet” introduced into the system by the transducer. Note that the along-track profile is Gaussian with a particular carrier frequency. The cross-track profile is a “Super-Gaussian” with exponent value of 6. B shows the “wave-packet” propagating through the medium. The medium is assumed to be homogeneous throughout the propagation path. The plot in B shows the along-track profile “slice” indicating the generation of harmonics by the medium manifested as a “sawtooth” waveform. C depicts interaction of the nonlinear wave with the object. Note that the temporal signal shows significant harmonic contributions to the waveform (sawtooth nature of the along-track wave profile). Also, diffraction has changed the cross-track profile to be more and more like a “sombbrero” function for circular transducer geometries. The sombrero function is defined in Easton [1997] as a radially symmetric function proportional to the radius, r , such that

$$SOMB(r) = \frac{2J_1(\pi r)}{\pi r} \quad (3-18)$$

where $J_1(\pi r)$ is the Bessel function of the first kind of order unity. The Fourier domain representation of the spatio-temporal wave is depicted in the lower portion of C . Note that the fundamental and its harmonics are present in the signal, as indicated by signal strength at the harmonic frequencies. After the nonlinear wave interacts with the object, reflection, or echo, signals are generated. These echo signals propagate back toward the sensing transducer. This propagation path is indicated as D . Since the signal strength of the reflections is sufficiently small,

nonlinearities are not reintroduced on the return path through the medium. The RF signal present at the face of the sensing transducer is the coherent summation of each harmonic that propagates back to the sensing transducer after signal interaction with the object. The RF signal is illustrated in *D*. The transducer will introduce its spatio-temporal function as the return signal is sensed. This reintroduction of transducer effects is depicted in *E*. In *E*, the fundamental and second harmonic signals are separated using simple frequency filtering techniques. The fundamental signal is envelope detected at the fundamental frequency. The second harmonic signal is detected at the second harmonic frequency. The images are then constructed as intensity maps of the envelope detected signal.

This modular approach to NUPROP processes allows the user to investigate particular functional dependences relative to the signal at various places within the propagation path.

Post Processing: Statistical Analyses

Statistical analyses are performed on B-scan images by using IDL's internal function, *MOMENT*. The *MOMENT* function computes the mean, variance, and skewness of a sample population contained in an *n*-element vector *X*. If the vector contains *n* identical elements, *MOMENT* computes the mean and variance, and returns the IEEE value NaN (not a number) for the skewness, which is not defined. When $x = (x_0, x_1, x_2, \dots, x_{N-1})$, the various moments are defined as follows:

$$MEAN = \bar{x} = \frac{1}{N} \sum_{i=0}^{N-1} x_i \quad (3-19)$$

$$VARIANCE = \sigma^2 = \frac{1}{N-1} \sum_{i=0}^{N-1} (x_i - \bar{x})^2 \quad (3-20)$$

$$SKEWNESS = \delta^3 = \frac{1}{N} \sum_{i=0}^{N-1} \left(\frac{(x_i - \bar{x})}{\sigma} \right)^3 \quad (3-21)$$

An image is converted from an array of values with double indices, i and j , to its lexicographic representation, x_k , where k ranges from 0 to $N-1 = i \cdot j - 1$. N is the total number of elements in the array (or vector).

Along with the statistics of the fundamental, second harmonics, and third harmonic images, their respective intensity histograms, and thresholded images are presented. The histograms give a graphical representation of the statistical values associated with the images. Simple thresholding of the images show the potential for object detection and segmentation.

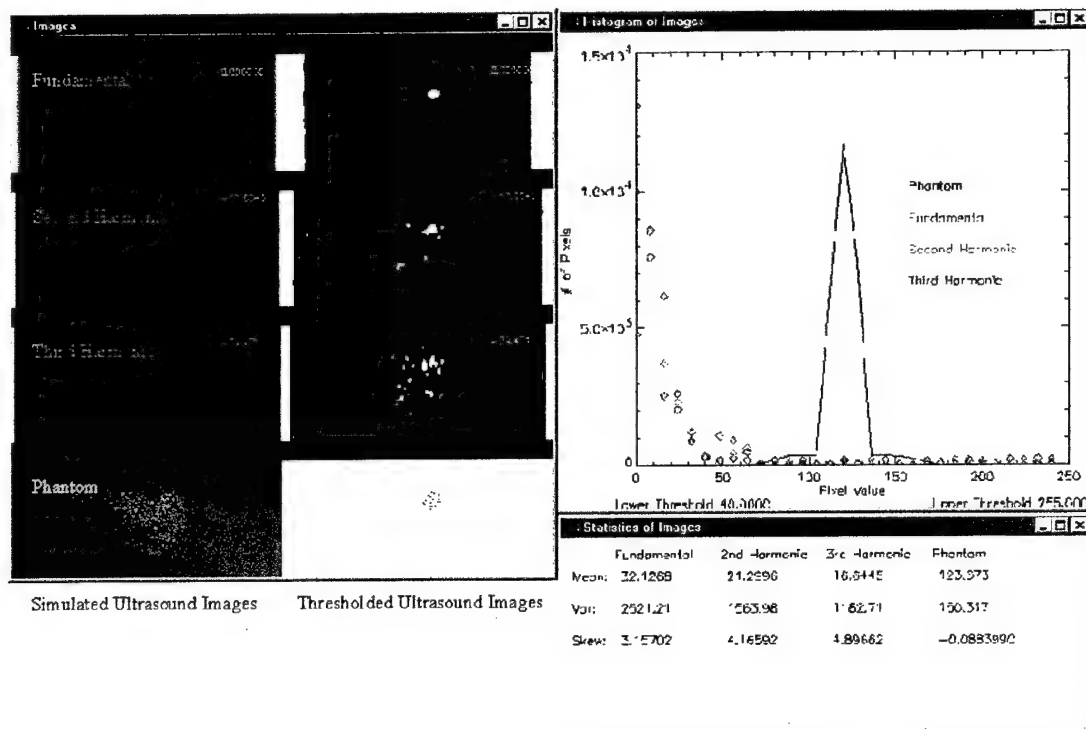


Figure 3-4. Example of statistical analyses from NUIPROP ultrasound simulation widget. The left panel displays the simulated images for the fundamental, second and third harmonics, and the phantom along with their respective thresholded images. For this example, a simple threshold level of 40 was used. The upper right panel displays the histogram plots for each simulation image. The lower right panel displays each simulated image's statistics: mean, variance, and skew.

Chapter 3: Summary

NUPROP is a fairly complex simulation and analysis tool for ultrasound modeling. NUPROP represents an end-to-end modeling environment for studying ultrasound wave propagation and, ultimately, B-Scan image formation. This chapter discussed the generation of objects called phantoms using Bamber's continuous point scatterer concept. The tissue characteristic of interest was acoustic impedance. Input signal waveforms used in NUPROP are either sinusoidal or frequency modulated sinusoidal, either apodized (for image formation) or non-apodized (single frequency or continuous used for code verification and harmonic signal analyses).

Nonlinear propagation was modeled using either the Burgers' equation or Fubini solution approaches. Blackstock developed a closed form solution to the Burgers' equation that possessed the shock distance parameter, L , which is calculated from system parameters of velocity, initial wave amplitude, nonlinear parameter (β), and fundamental frequency. Likewise, the Fubini approach possessed this same shock distance limitation.

Linear propagation was modeled using Angular Spectrum and Lommel. Angular spectrum has the advantages of being applicable throughout the propagation path, accommodate non-radially symmetric transducer geometries, and accurately computes nonlinear or harmonic generation. Angular spectrum requires a trade-off between computational speed/volume and accuracy/precision in computing trans-axial beam profiles. Lommel, on the other hand, computes the on-axis longitudinal beam profile and the trans-axial beam profiles at depth with accuracy and precision. Unfortunately, Lommel formulation suffers from two major limitations: radial symmetry only and linear propagation only. Lommel does not predict harmonic signal formation nor does it accurately compute off-axis beam profiles for non-radially symmetric geometries.

Lommel does not accurately compute the pressure field just in front of the transducer. A minimum propagation distance is required before Lommel can be used.

Image generation is accomplished using the Hilbert transform, which converts a RF signal to an "envelope" detected intensity signal.

Finally, NUPROP performs some rudimentary post processing such as statistical analyses, histogram plotting, and simple image thresholding based on the statistics of the images.

Chapter 4. Code Development and Description

This chapter discusses NUPROP's code development, the use of Interactive Data Language Environment for developing the graphical user interface; describing menu operations, radio button operations, data or parameter input, with computational considerations where appropriate.

NUPROP Hierarchy

The primary tool for modeling wave propagation in biological media is NUPROP. NUPROP is a code developed using Interactive Data Language (IDL), a high-level language environment from Research Systems, Inc. IDL is a complete computing environment for the interactive analysis and visualization of data. IDL integrates a powerful, array-oriented language with numerous mathematical analysis and graphical display techniques.

NUPROP is widget-based in that a graphical user interface (GUI) provides the interactive platform for the user to exercise the physics associated with nonlinear and linear wave propagation. Widgets (or controls, in the terminology of some development environments) are simple graphical objects such as pushbuttons or sliders that allow user interaction via a pointing device (usually a mouse) and a keyboard. IDL graphical user interfaces are constructed by combining widgets in a tree-like hierarchy. Each widget has one parent widget and zero or more child widgets. There is one exception: the topmost widget (called a top-level base) is always a base widget and has no parent.

Figure 4-1 shows the tree-like hierarchy of NUPROP. NUPROP consists of four, first-level bases: Menu, Button, Parameter, and Display.

† See Figure 4-2 for more detail

NUPROP (Top Level Base)

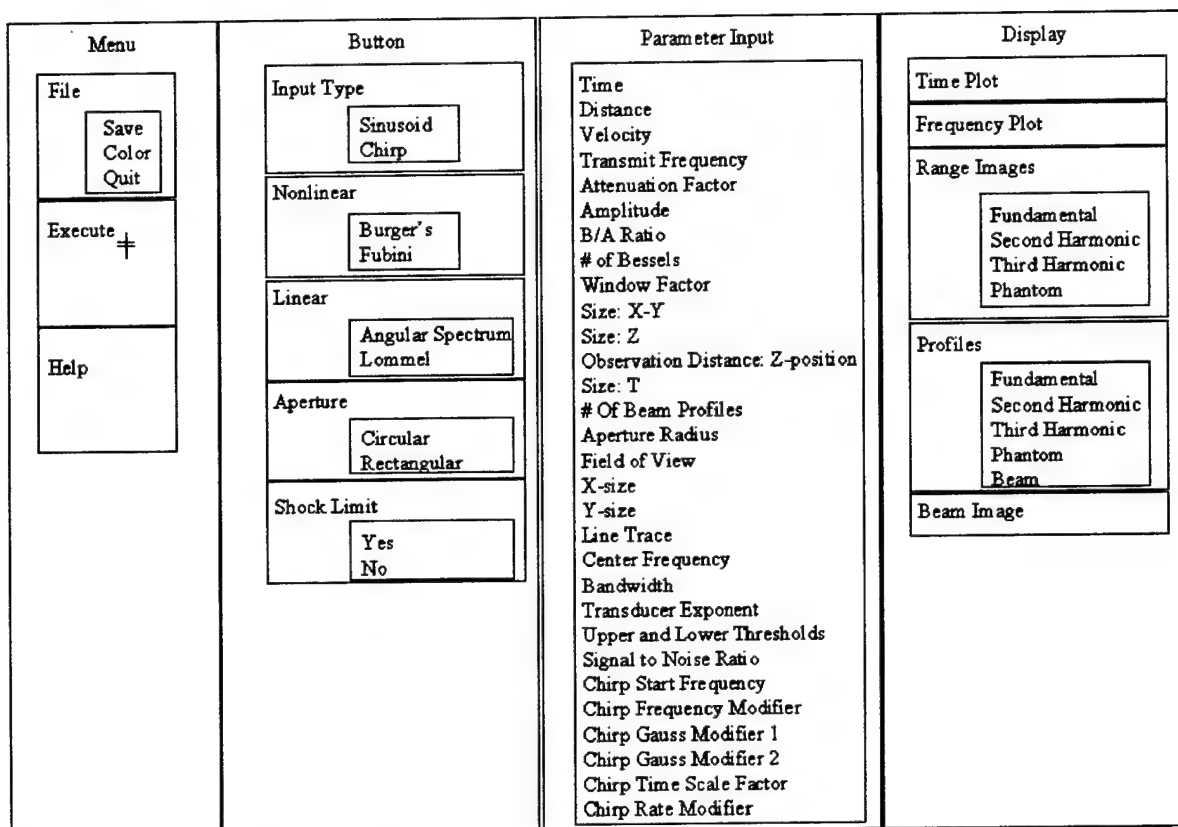


Figure 4-1. NUPROP hierarchy of processing. Each first-level base is designated with an underline: Menu, Radio Button, Parameter Input, and Display. Each second-level base is designated by the origination of an arrow such as File under the Menu Base Operations. Each third-level base is designated by smaller print text such as Sinusoid Chirp of Radio Button Base as well as a termination and origination of an arrow. Each fourth-level base is designated by small print italicized such as Plot Images under Menu Base/File/Save.

The Menu Base Operations consists of three second-level bases: File, Execute, and Help. File consists of three third-level bases: Save, Color, and Quit. Save consists of two fourth-level bases: plots and images. Execute is described later in this section. Help invokes a Windows-based help menu describing NUPROP and its various operations.

The Radio Button Operations Base consists of five second-level bases: Input Type, Nonlinear Process Type, Linear Process Type, Aperture Type, and Shock Limited Processing. Input Type consists of two third-level bases: sinusoid and chirp. Nonlinear Process Type consists of two third-level bases: Burgers' and Fubini. Diffraction Type consists of two third-level bases: Angular

Spectrum and Lommel. Aperture Type consists of two third-level bases: Circular and Rectangular. Shock Limited Processing consists of two third-level bases: Yes and No.

The Parameter Input Base consists of thirty second-level bases:

1. Time: time scale factor over which to display the temporal waveform (in seconds)
2. Distance: maximum ultrasound wave penetration depth (in meters)
3. Velocity: group velocity of the ultrasound wave (in meters per second)
4. Transmit Frequency: oscillation frequency of the ultrasound (in Hertz)
5. Attenuation Factor: media attenuation (in dB per cm per MHz)
6. Amplitude: initial ultrasound wave amplitude (in MPa)
7. B/A Ratio: nonlinear parameter (in $\text{m}^2/\text{s}/\text{kg}$)
8. # of Bessels: number of terms to include in the determination of nonlinearity
9. Window Factor: temporal apodization of waveform
10. Size (X-Y): cross-track resolution (in pixels)
11. Size (Z): along-track resolution (in pixels)
12. Z-Position: observation distance. Actual distance is calculated by multiplying the distance by the Z-position and dividing by the along-track resolution (in pixels)
13. Size (t): number of time intervals within the time scale factor
14. Beam Profiles: number of range intervals over which to determine beam profiles
15. Aperture Radius: radius of the transducer (in meters)
16. FOV: field of view associated with the cross-track resolution (in meters)
17. X-Size: rectangular aperture size in the x-direction (in meters)
18. Y-Size: rectangular aperture size in the y-direction (in meters)

19. Line Trace: used for sinusoid input only. Determines which frequency slices to display in the range versus frequency plots. Also determines which range profiles to use when calculating the propagation distance influence on harmonic amplitudes (in pixel value)
20. Center Frequency: center frequency of the receiver transducer (usually the same transducer as the transmit transducer, in Hz)
21. Bandwidth: bandwidth over which the transducer responds (in Hz)
22. Transducer Exponent: the transducer response is Gaussian. When this exponent is equal to two, then the transducer is the typical Gaussian profile. When the value is three or greater, the Gaussian response changes progressively more toward a RECT function.
23. Lower Threshold: Coupled with Upper Threshold establishes the range over which pixel values are either turned black or white. Used in statistical analyses to determine "ease" of detection based on differential acoustic impedance
24. Signal to Noise Ratio: Value associated with the power ratio of signal to noise
25. Chirp Start Frequency: start frequency of the chirp input signal (in Hz)
26. Chirp Frequency Modifier: value that modifies (increase or decreases) the starting chirp frequency
27. Chirp Gauss Modifier 1: the chirp input signal is apodized. In combination with the second Chirp Gauss Modifier, this Chirp Gauss Modifier determines the overall shape of the Gaussian apodization function
28. Chirp Gauss Modifier 2: See Chirp Gauss Modifier 1
29. Chirp Time Scale Factor: determines the temporal window over which the chirp signal is displayed
30. Chirp Rate Modifier: modifies the chirp rate.

The Display Base consists of five second-level bases: Temporal Plot, Frequency Plot, Range Images (X-Z), Profiles, and Angular Image (X-Y). Range Image (X-Z) consists of four third-level bases: Fundamental, Second Harmonic, Third Harmonic, and Phantom. Profiles consists of five possible third-level bases: Fundamental, Second Harmonic, Third Harmonic, Phantom, and Beam.

Figure 4-2 shows the continuation of the Execute option under Menu. Execute consists of six third-level bases: phantom generation, waveform generation, image generation, image profiles, movies, and statistical analyses. Image profiles consists of three fourth-level bases: x-z image profile, x-y image profile, and aperture or beam profiles (X-Y Images). Movies option consists of two fourth-level bases: temporal movies and spatial movies. Temporal movies option consists of two fifth-level bases: time and frequency movies. Spatial movies option consists of two fifth-level bases: beam profile and image movies. Image movies option is not currently active.

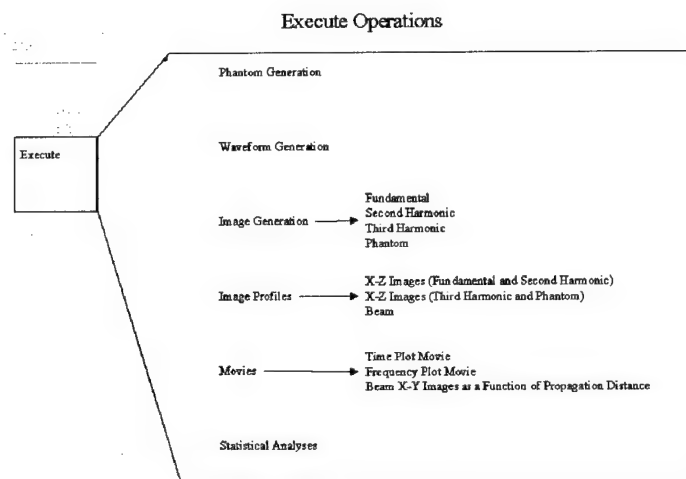


Figure 4-2. The Execute Base. Execute is the “heart” of NUPROP. Through the Execute Base all NUPROP processes are activated. All the parameters set in the Parameters Base are used to generate the waveforms necessary to simulate nonlinear ultrasound propagation and, consequently, image formation.

Menu Operations

File

Under Files Operations, the user can implement the Save routines for either the plots or images generated from the Execute operations. Plots consist of the temporal signals (whether time displayed or frequency displayed). The angular beam profiles are also saved, if generated during the Execute operations. Color option allows the user to choose one of over 41 different color schemes built into IDL. The color option also allows the user to change the color table by introducing a user defined color mapping. The Quit option is self-explanatory.

Execute

The user can generate complex phantoms using the phantom generate option under execute. This operation initiates a module called NUPROP_Phantom_Generate. This module allows the user to modify settings for three elliptical objects: nominal acoustic impedance, variation in acoustic impedance, size, shape, and orientation of the objects. The user can change the variation in acoustic impedance for the background as well. The simulation phantom and its pristine representation are displayed. The user can save the simulation phantom and its pristine representation by selecting the save option under file. The user can terminate this module by selecting quit from the file menu. To simulate tissue, digital representations are generated using Bamber's concept of continuous array of point sources representing the phenomenon of interest. NUPROP simulates acoustic impedance by generating a complex image of point sources as follows:

1. Determine the number and size of scatter regions
2. Determine the strength of acoustic impedance for each scatter region

3. Determine each region's variation in acoustic impedance
4. Generate the image based on these determinations using an IDL code called NUPROP_Tissue_Generate. NUPROP_Tissue_Generate is a module incorporated into NUPROP.

Figure 4-3 shows an example of a complex phantom generated by NUPROP. NUPROP generates three elliptical objects based on the parameters set by the user. The average value of the tissue simulated image is zero. This prevents the introduction of an artificially induced acoustic impedance difference. So, the variation is the only parameter that distinguishes each scatter region. The nominal levels are used to generate the pristine image so the user can visually cue the anomalous scatter region(s). The major and minor axis modifiers and the object extent modifier determine the overall size of the object. The object rotation angle (in degrees), object shift in x, and object shift in y determine the positioning and orientation of the objects in the 256x128 array. This tissue simulation phantom is equivalent to Bamber's continuous array of point scatterers.

Three elliptical objects, placed and oriented in a 256x128 array

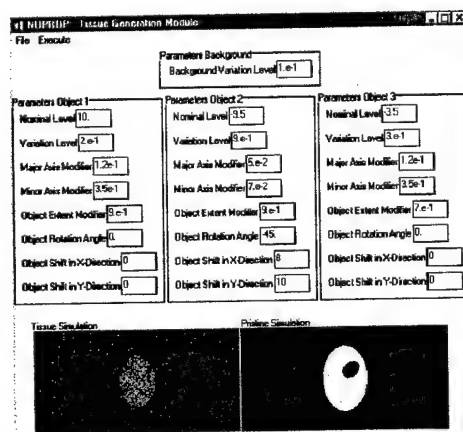


Figure 4-3. Example of NUPROP's generation of tissue phantoms. Three elliptical objects are oriented and inter-dispersed within a 256x128 array. The variation determines the regional distinction in the tissue simulation (left bottom image). The nominal levels determine the distinction between regions in the pristine simulation (bottom right image). The pristine image is used strictly for visually cueing of anomalous region(s). This example shows one hypo-echoic region (cyst).

The waveform execute operation begins the process of generating nonlinear waveforms. Input from the Radio Button settings and parameter values determine how the waveform will be generated. Figure 4-4 illustrates the NUPROP widget.

NUPROP Widget-Based Graphical User Interface

NUPROP: Nonlinear Ultrasound Wave Propagation _ | □ | X

File Execute Help

Input

☒ Sinusoid

☐ Chirp

Nonlinear

☐ Burger's

☒ Fubini

Diffraction

☒ Ang. Spect.

☐ Lommel

Aperture

☒ Circular

☐ Rectangular

Shock Limited

☒ Yes

☐ No

Status

Parameters

Time: 4.e-5

Distance: 10.e-2

Amplitude: 0.5

Xmit Freq: 1.75e6

Windw Fact: 5e-1

Velocity: 1500.

Atten. Factor: 1e-9

B/A Ratio: 7.0

Size: X-Y: 256

Size: Z: 256

Z-Position: 110

Size: t: 512

Beam Profiles: 8

of Bessels: 4

Apert. Radius: 6.5e-3

FOV: 10.e-2

X Size: 225

Y Size: 15

Line Traces: 70

Center Frequency: 3.5e6

Bandwidth: .5e6

Transducer Exponent: 2

Lower Threshold: 40

Upper Threshold: 255

Signal to Noise Ratio: 5e9

Chirp Start Freq: 1.5e6

Chirp Frequency Modifier: 1.

Chirp Gauss Modifier1: 3.5e9

Chirp Gauss Modifier2: 1.

Chirp Time Scale: 1.

Chirp Rate: 8.5e11

TEMPORAL SIGNAL

RANGE IMAGE: (X:Z)

ANGULAR IMAGE: (X:Y)

FLAQUENTIAL

2ND HARMONIC

3RD HARMONIC

PHANTOM

Figure 4-4. Example of NUPROP Widget-Based Graphical User Interface. This example illustrates the basic widget configuration including the radio buttons, parameter input section, display regions, and the status bar.

The radio button settings determine the type of input signal (single frequency sinusoid or chirp), nonlinear processing (Burgers' or Fubini), linear or diffraction processing (angular spectrum or Lommel), aperture type (circular or rectangular), and whether or not the shock distance limitation will be invoked.

The parameter settings determine the fundamental characteristics of the output signal. The general scenario is determined by the time and distance parameters. The material type is

determined by velocity, B/A Ratio, and attenuation factor parameters. To determine computational size, # of Bessels, Size X-Y, Size Z, Size t, and Beam Profiles parameters are used.

Depending on the radio button settings, different parameter sets within the parameter widget are used. If the input signal is a single frequency sinusoid, transmit frequency, window factor, center frequency, bandwidth, transducer exponent, and line trace parameters are used. If the input signal is the chirp, then chirp start frequency, chirp frequency modifier, chirp Gauss modifiers 1 and 2, chirp time scale, chirp rate modifier, and transducer parameters are used. If the transducer geometry is circular, then the aperture radius and FOV are used. If the transducer geometry is rectangular, then the X-Size and Y-Size are used along with the FOV parameter.

The user can generate simulated ultrasound images by selecting image generate under the execute option. NUPROP will use the parameter settings that generated the waveforms. The simulated ultrasound images will be displayed within the RANGE IMAGE (X-Z) region of the widget (see Figure 4-4) for the fundamental, second and third harmonics, and the phantom used. The transducer geometry is displayed within the ANGULAR IMAGE (X-Y) region.

Statistical analyses can be performed on the images by selecting Statistical Analyses in the execute menu. A display of the statistics (mean, variance, skew), a histogram of the intensity values, and a rudimentary threshold segmentation of the fundamental, second and third harmonics, and the phantom images are presented. Figure 4-5 (repeat of Figure 3-4) illustrates an example statistical analyses.

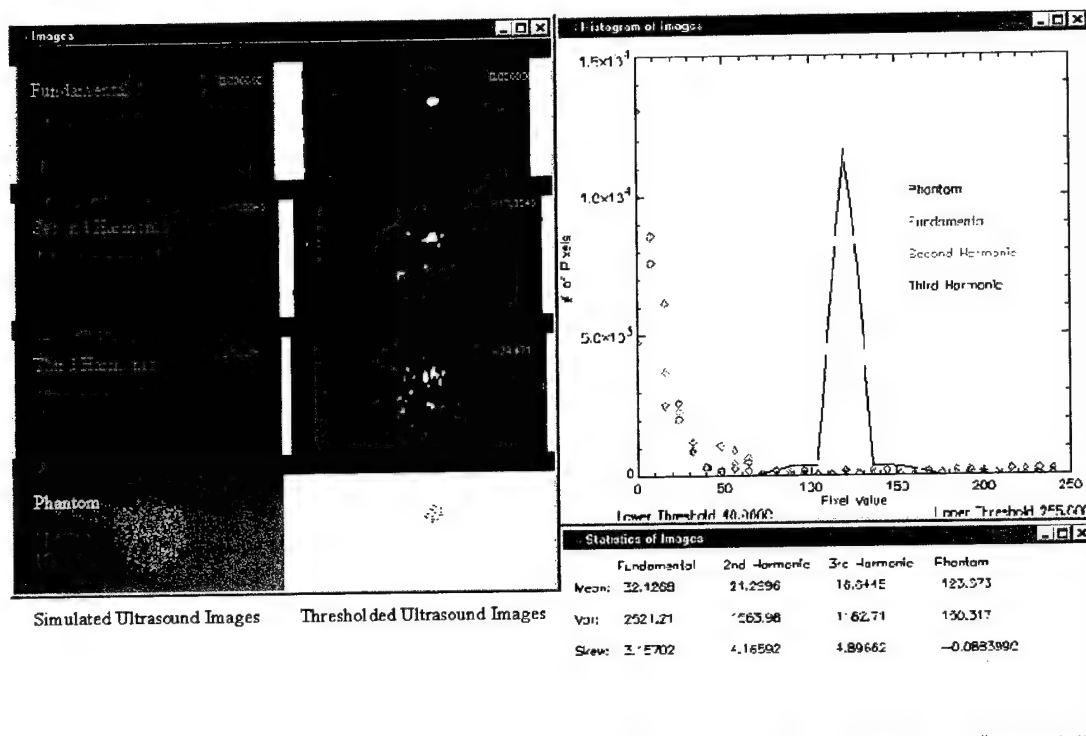


Figure 4-5. Example of statistical analyses from NUPROP ultrasound simulation widget. The left panel displays the simulated images for the fundamental, second and third harmonics, and the phantom along with their respective thresholded images. For this example, a simple threshold level of 40 was used. The upper right panel displays the histogram plots for each simulation image. The lower right panel displays each simulated image's statistics: mean, variance, and skew.

Computational Considerations Associated with Radio Button Selections

Input Type

If the windowing factor is sufficiently small, on the order of 0.00005 , then a single sinusoid input is essential continuous. However, if the windowing factor is on the order of 0.5 , then the single sinusoid input is pulsed (finite temporal duration). A pulsed, single sinusoid input is no longer monotonic but is comprised of a "band" of frequencies centered on the fundamental frequency. This characteristic significantly impacts the computational results: onset distances for second and third harmonics, and image formation. For the chirp, if the windowing factor is on the order of 5×10^{-13} , then the input signal is essentially continuous. If the windowing factor is on the

order of 5×10^{-5} , then the chirp becomes an apodized or pulsed chirp which translates to a "low passed" chirp signal in the frequency domain.

Nonlinear Processing: Burgers' or Fubini

Equation 3-4 gives the closed form solution to Burgers' equation as derived by Blackstock. This solution incorporates the limitation of the shock distance in the calculation of the distorted waveform. NUPROP will not compute the waveform unless the shock distance limitation is turned off. Once the shock distance limitation is turned off, then NUPROP computes the waveform. The user should realize that the waveform computed is no longer valid. The Fubini approach also possesses this shock distance limitation.

Linear Processing: Lommel

Computationally, Lommel is significantly faster than angular spectrum. However, the Lommel formulation approach is strictly a linear processing technique and cannot be used for forward propagation of the ultrasound wave, since the medium introduces nonlinearities, provided the scenario parameters are conducive to harmonic wave formation. To correctly predict the waveform in the outbound direction, a step by step (small increments) approach is required. Angular spectrum provides this incremental determination of the waveform. The field at a propagated distance, z_n , depends on the waveform frequency content at the previous step, z_{n-1} . Once the field has interacted with the target region, the return signal is sufficiently small that nonlinearities are not introduced on the return or inbound direction. Lommel can be used for the inbound or return propagation. Additionally, the Lommel formulation used in NUPROP requires circular (radial) symmetry. Under very restricted conditions, however, the Lommel formulation can produce reasonable approximations for on-axis signal amplitudes for rectangular arrays.

Shock Limited Distance Calculation

As mentioned previously, the shock distance limits the range over which valid computations can be made. NUPROP allows the user to circumvent this limitation with the understanding that observation distances beyond the shock distance will produce invalid results.

Computational considerations associated with parameters

Format Size

The format size greatly impacts the computational speed of NUPROP. NUPROP generates volumetric data: x-y-z and t. The waveforms generated using NUPROP's nonlinear module are dependent on z and t. The images generated using NUPROP's image generation module(s) are dependent on x, y, z, and t. As an example, if the user chooses an angular array size of 256 x 256 and a number of beam profiles of 64, then a 256 x 256 x 64 "data cube" will be generated. This data cube is for storing the necessary information for several other operations such as beam movies and angular spectrum displays. A data cube of this size, given 8-bit precision results in a 3.36 Mbyte data cube. If the angular array size is doubled, then the data cube size becomes 13.42 Mbytes. Care must be exercised when generating large computational arrays. Memory allocation limitation as well as computational time must be considered.

Line Trace

The line trace feature allows the user to pick a set of frequency traces from the nonlinear waveform generated data set. Line trace is applicable to single frequency input only. Usually, the line trace is an integer divisor of the fundamental frequency. For instance, using a sinusoidal input at 2 MHz, 1500 m/s wave velocity, time of 20 μ s, line trace to use is 20. The list below provides

the appropriate values for the line trace given the input frequency, with a wave velocity of 1500 m/s, time of 20 μ s.

Frequency (MHz)	Line Trace (Pixel Number)
0.8	8
1.0	10
2.0	20
3.0	30
4.0	40

The user has the option of picking any line trace with the following limitation: the highest harmonic line trace must be less than the array size allotted for frequency computations. For example, if the frequency computational array is set to 512, and the number of frequency terms to compute is three, then the third harmonic cannot exceed 512, which, in turn, limits the line trace value to 170.

Number of Bessel Terms.

The number of Bessel terms impacts the computation of the nonlinear waveform. NUPROP uses the number of Bessel terms to determine the number of frequency terms to compute. This process is relatively fast, but is platform dependent. For a 350MHz Pentium II, the runtime for computing 30 frequency components (each component waveform vector size: 512) is approximately 35 seconds. Additionally, the number of Bessel terms computed must take into account the temporal frequency array size. If the array size is too small, then higher order Bessel terms will be aliased. Typical computational size settings are as follows:

1. # of Bessels: 3 – since, for most harmonic signal generation conditions, 90% or more of the wave energy is captured in the first three terms – fundamental, second and third harmonics
2. Size X-Y: 256 – this array size yields reasonably accurate cross-track beam profiles

3. Size Z: 256 – this vector size, combined with Size X-Y, yields a reasonably sized volumetric array for accuracy, computational memory requirements, and computational time
4. Size t: 512 – this vector size yields reasonably accurate temporal and frequency plots, especially for # of Bessels parameter size in excess of 10
5. Beam Profiles: 8 – this vector size is suitable for “gross” approximations of down-range, on-axis profiles. For better accuracy, a Beam Profiles value of 128 is appropriate. The computational time will greatly increase (on the order of five to six minutes to compute the beam profile).

Chapter 4: Summary

In summary, NUPROP is a modularly design IDL code that models, end-to-end, nonlinear ultrasound wave propagation and ultrasound image formation. NUPROP is based on “widgets,” or controls, in the terminology of some development environments. Widgets are simple graphical objects such as pushbuttons or sliders that allow user interaction via a pointing device (usually a mouse) and a keyboard. IDL graphical user interfaces are constructed by combining widgets in a tree-like hierarchy. Each widget has one parent widget and zero or more child widgets. There is one exception: the topmost widget (called a top-level base) is always a base widget and has no parent. So, NUPROP is a graphical user interface (GUI) providing the interactive platform for the user to exercise the physics associated with nonlinear and linear wave propagation.

NUPROP is built with modules (operations that are, essentially, stand-alone in that they do not need the GUI to work) and functions (modular code that requires parameter values passed through the GUI to operate). The complexity of each module or function determines the computational requirements, hence the computational time, accuracy, and precision.

Chapter 5. NUPROP Verification

This chapter describes the verification of NUPROP as compared to existing data, other code simulations, and conditions required to generate nonlinearly/linearly propagated ultrasound waves. Sections are divided into Longitudinal Signal Formation (nonlinear propagation), Trans-axial Signal Formation (linear or diffraction), and Image Formation.

Longitudinal Signal Formation.

Figure 5-1 shows the comparison between NUPROP's Fubini and Burgers' solutions for wave propagation in water at 23°C, at 5 centimeters and 9.52 centimeters from the transducer (2.58 MHz, circular) and data from Ryan, 1963.

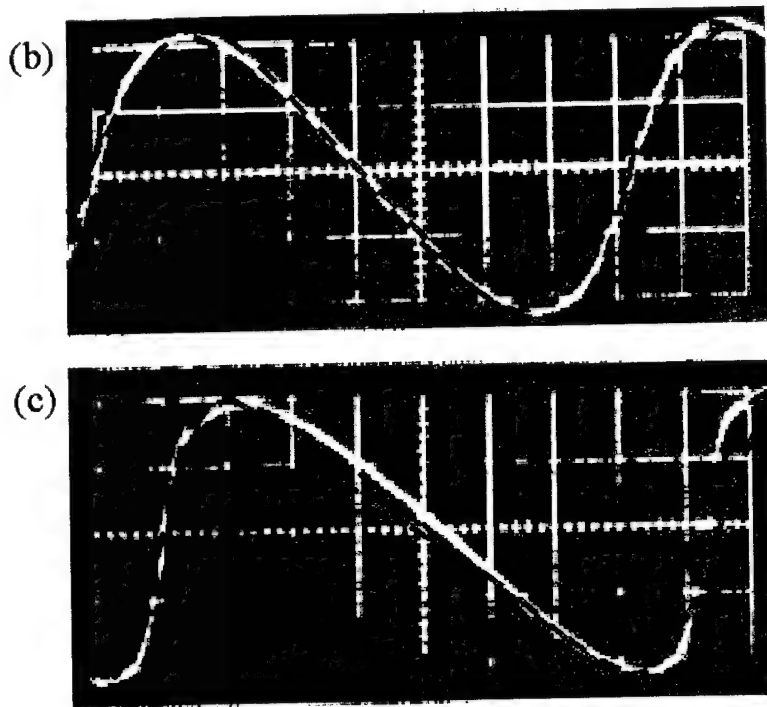


Figure 5-1. Comparison of NUPROP output and data from Ryan, R. P., Ph.D. thesis, Brown University, 1963. The underlying image is data captured from photographing the oscilloscope output at two penetration depths: 5 and 10 cm. The overlaying traces are NUPROP predictions using Fubini (black dotted) and Burgers' (dotted red) under the same (5 cm penetration depth) or similar conditions (9.52 cm vice 10 cm). Note that under conditions prescribed for (b), NUPROP predicts the nonlinear waveform precisely. For condition (c), NUPROP predicts the waveform at the shock distance (9.52 cm), comparing favorably with Ryan's data at 10 cm.

Ryan defined σ as the ratio of the observation distance to the shock distance. In the case of condition (c) $x = 10$ centimeters, σ is 1.05, slightly passed the computed shock distance, 9.52 centimeters. NUPROP checks to see if the observation distance exceeds the shock distance. If it does, then NUPROP will not compute the waveform since the model is invalid beyond the shock distance. However, the user can bypass this limitation by selecting "no" for shock limit (radio button option in NUPROP), realizing that the results are not valid. For condition (b), NUPROP results (Fubini and Burgers') are nearly an overlay of the experimental data. NUPROP used 15 frequency components to generate the waveform. According to Christopher (personal communications, 1998), no less than 20 to 25 terms should be used to reduce any "wavy" artifact in the reconstruction. For condition (c), NUPROP produced results within 1% error using Fubini or Burgers'.

Figure 5-2 shows the growth and decay of harmonics for 2.5MHz ultrasound in water. The comparison is between data collected by Ryan, et. al. (left graph) and results from simulations with NUPROP (right graph). Ryan's theoretical predictions are the solid curves. The other data in Ryan's graph are (x) digital analysis; (λ) analyzer measurement. Digital analysis was accomplished via photographing waveforms on the oscilloscope and digitizing the photographs. Analyzer measurements were accomplished by passing detected signal through electric circuit tuned to the appropriate harmonic. The graph on the right is from NUPROP under the same conditions from Ryan, et. al.: 2.5 MHz ultrasound wave in water. NUPROP settings were wave velocity: 1550 m/s; number of Bessel terms: 4; B/A ratio: 5.3. NUPROP predictions are less than 1 percent deviation from Ryan's predicted growth and decay for the fundamental, second, and third harmonics.

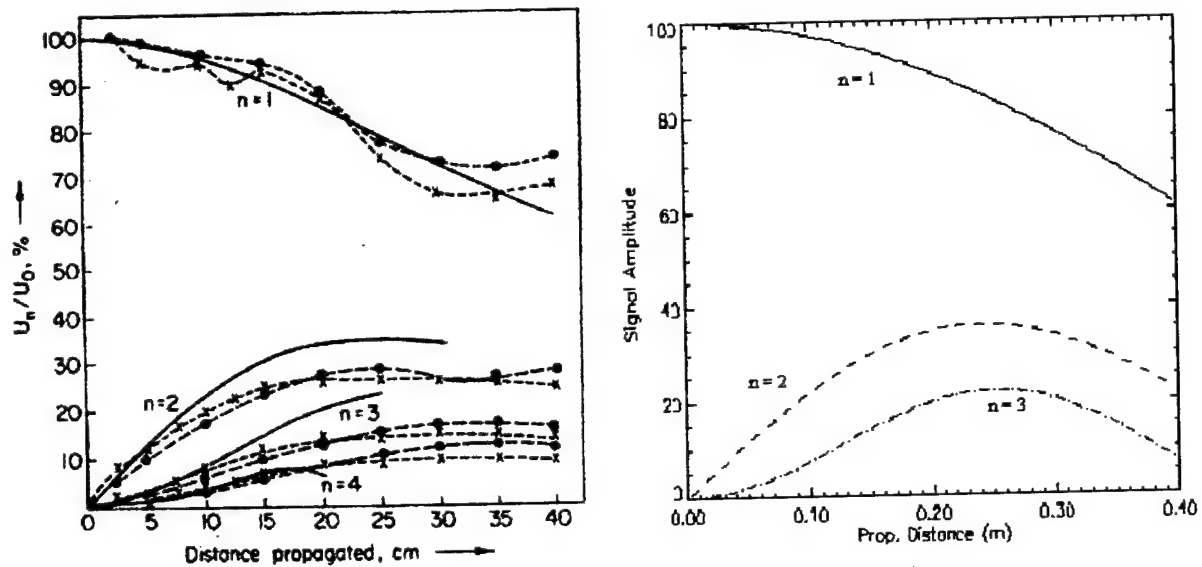


Figure 5-2. Comparison of fundamental decay and harmonic growth. Data on the left is from Ryan, R. P., A. Lutsch, and R. T. Beyer, *J. Acoust. Soc. Am.*, 34, 31, (1962).

Figure 5-3 shows NUPROP's predicted on-axis longitudinal signal amplitude (fundamental and second harmonic) as a function of propagation distance in comparison to data from Averkiuo, Roundhill, and Power, 1997. Averkiuo, et. al. assumed that a circular transducer with equivalent area to a rectangular transducer would produce equivalent on-axis, longitudinal signal amplitude profiles. The solid black line represents Averkiuo's 2 MHz fundamental on-axis longitudinal profile for a P3-2 geometry. The thick dashed line is NUPROP's prediction using an actual P3-2 transducer configuration. Likewise, the thin dashed line is Averkiuo's second harmonic on-axis longitudinal profile. The thin dotted line is NUPROP's second harmonic axial amplitude profile using a P3-2 transducer configuration.

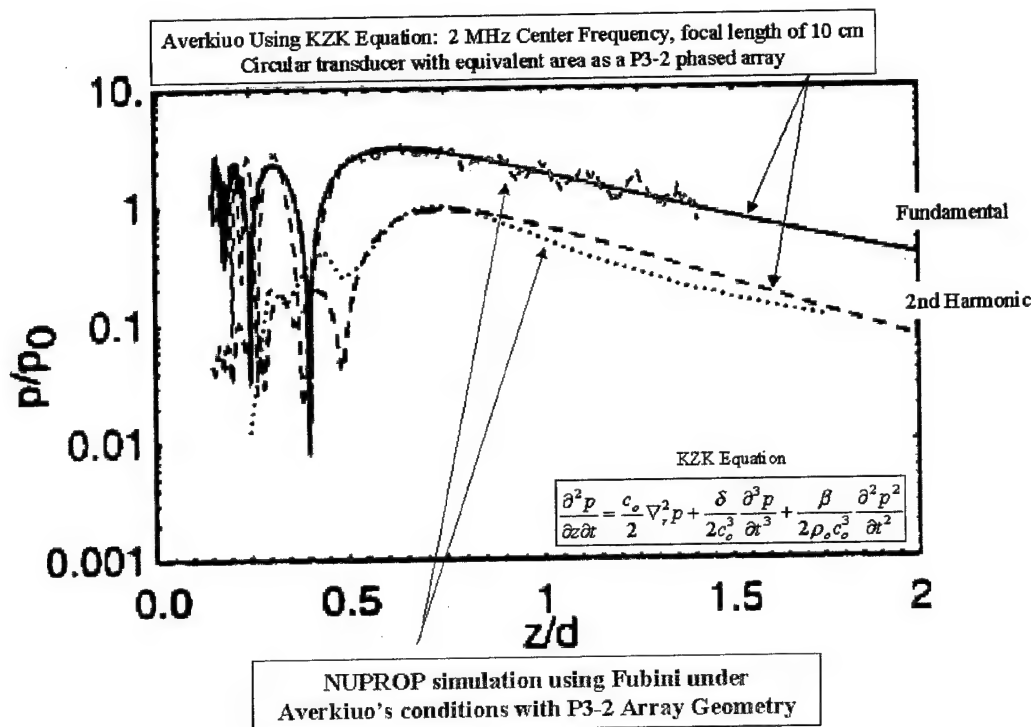


Figure 5-3. Comparison of data from Averkiuo et. al. and NUPROP for a P3-2 rectangular geometry transducer on-axis signal strength as a function of propagation distance. The solid line represents Averkiuo's on-axis signal amplitude at the fundamental frequency of 2 MHz, 10 cm focal length, circular transducer with equivalent area to the P3-2 rectangular transducer.

Averkiuo assumed a circular aperture of equivalent area would produce an equivalent on-axis signal attenuation as an actual P3-2 geometry. The difference in second harmonic traces is due to the differences in using circular equivalence and an actual P3-2 configuration. For the fundamental, the difference is minimal, whereas the difference in second harmonic is more significant, ranging upwards of 20 percent. The "wavy" nature of the fundamental for NUPROP is due largely to wrap-around effects (or spatial errors). It should be noted that the spatial wavefront is not attenuated at the edges, as in both Averkiuo's and Christopher's implementations. The spatial apodization will eliminate the "wavy" nature of the fundamental as well as correct for the differences shown for the second harmonic in Figure 5-3. This data supports Averkiuo's supposition of equivalence, but does reveal potentially large errors, especially for second harmonic amplitudes.

Figure 5-4 further reveals the danger of Averkiou's equivalence approximation. As aperture size increases, errors slightly decrease: 8 pixels diameter produced a maximum error of 23.0469%, 16 pixels produced a maximum error of 22.1680%, and 32 pixels produced a maximum error of 21.6553%.

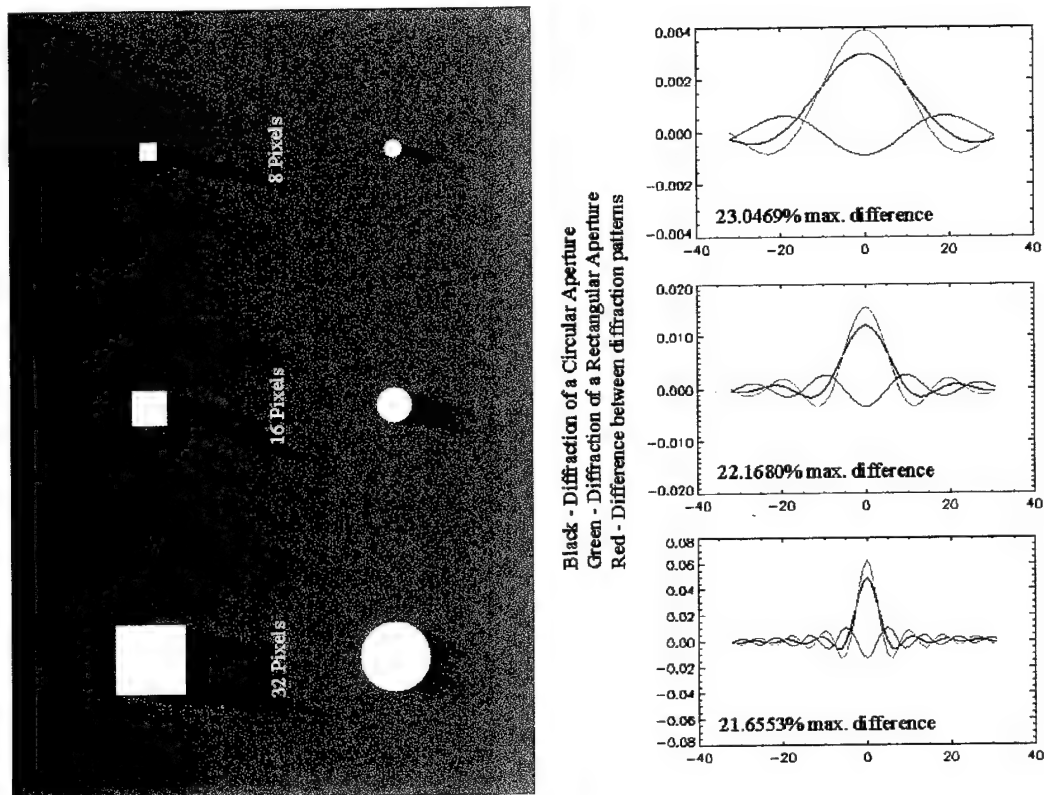


Figure 5-4. Demonstration of difference between circular and rectangular aperture diffraction patterns and its effect on signal strength. As the size of the aperture increases, the maximum signal difference, in percent, slightly decreases: 8 pixels produced a maximum difference of 23.0469%; 16 pixels produced a maximum difference of 22.1680%; 32 pixels produced 21.6553% difference.

Figure 5-5a,b shows a comparison between NUPROP's angular spectrum and Lommel formulation longitudinal on-axis signal attenuation as a function of propagation distance. Angular spectrum technique has a computational limitation that requires a minimum angular resolution of 256 by 256 pixels. Figure 5-5a illustrates the effect on increasing the angular resolution from 32 pixels to 256 pixels, keeping the range resolution fixed at 8 pixels. The solid black curve is the Lommel formulation solution for on-axis signal strength as a function of propagation distance. A

circular piston transducer with 1.0 cm diameter, center frequency 0.956 MHz, range of 23.9 cm, and the wave group velocity of 1200 m/s was used. At coarse range resolution (8 datapoints over the entire range), the angular spectrum technique appears to “follow the average value” of Lommel formulation quite well (256 x 256 cross-track resolution). It should be noted that the Lommel curve used 1024 datapoints in the down-range dimension (z-direction). However, as the cross-track resolution decreases, the angular spectrum representation begins to deviate substantially. Figure 5-5b shows the effect of increasing down-range resolution while maintaining the cross-range resolution fixed. As is readily apparent, the down-range resolution has little effect on the overall accuracy of the angular spectrum. Cross-track resolution significantly impacts the fidelity of the representation relative to the Lommel formulation values.

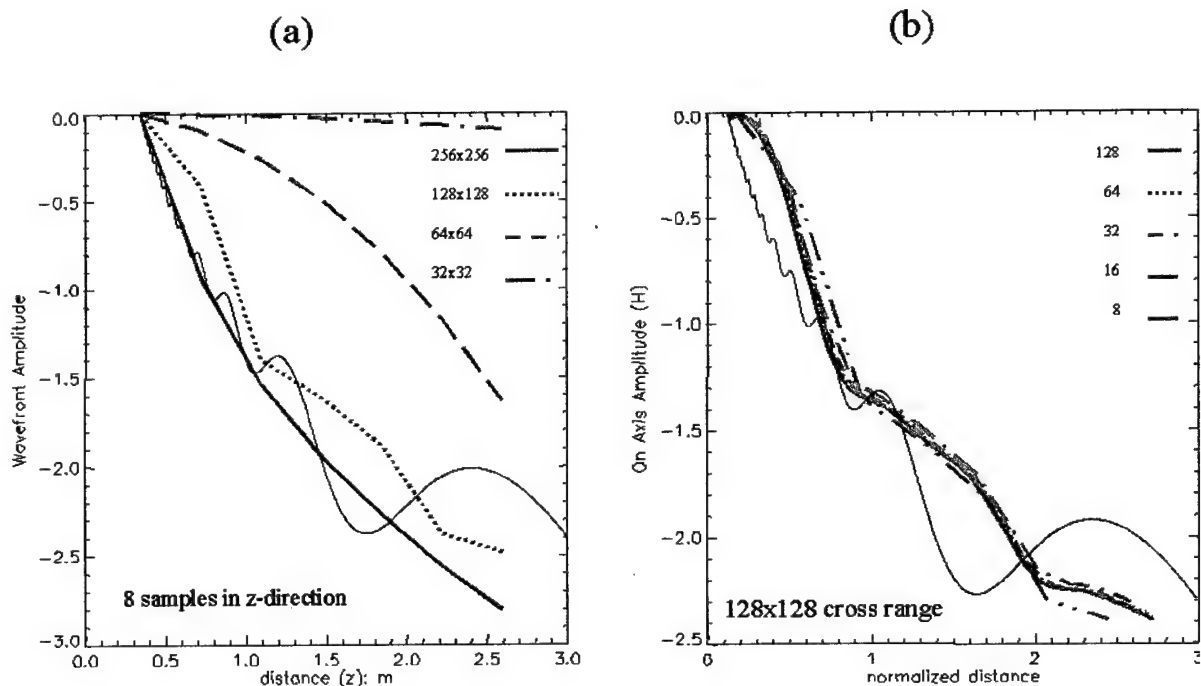


Figure 5-5 Comparison of angular spectrum (Red Curves) and Lommel (Black Curve) formulation accuracy. (a) Effects of increasing cross-track resolution on angular spectrum accuracy. (b) Effects of down-range resolution on angular spectrum accuracy.

Trans-Axial Signal Formation

Trans-axial signals are formed, primarily, by diffraction. Figure 5-6 compares NUPROP's generation of trans-axial beam profiles and results from Christopher's NLP code. The black curves correspond to Christopher's NLP code and the red curves correspond to NUPROP's Fubini-Angular Spectrum Technique. For trans-axial distances less than 1.5 cm, NUPROP and NLP are within a few percent. Beyond 1.5 cm, NUPROP and NLP results differ as much as 50% in amplitude value. The side lobe termination points (valley points) are the same for both NUPROP and NLP. The differences in amplitude values for trans-axial distances greater than 1.5 cm is due to the finite extent in the NUPROP calculations. NUPROP assumes a finite boundary, or distance, over which to calculate the trans-axial beam profile. This boundary is manifested by the field of view parameter causing a "wall effect" or wrap-around to occur, thus altering the overall amplitude of beam profile outside of 1.5 cm. This difference is more prominent in the second harmonic beam profile than the fundamental. These differences can be corrected by using a spatial apodization to smooth out the edges, thus eliminating the wrap-around in the calculations.

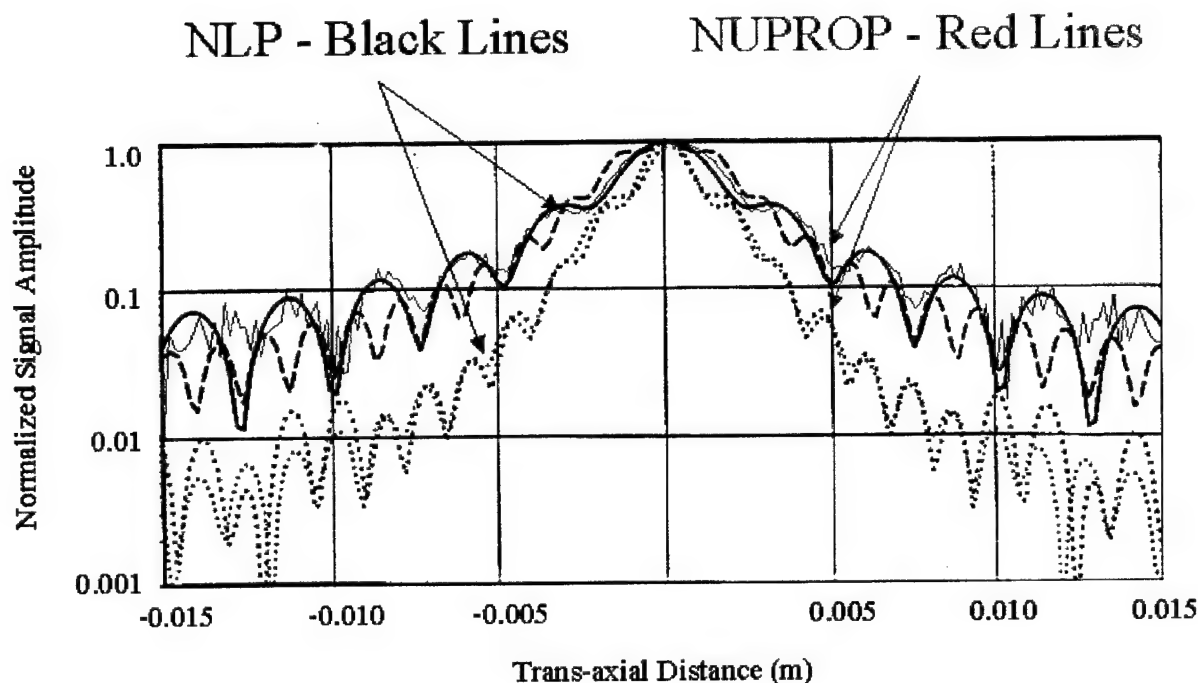


Figure 5-6. Comparison of NUPROP's Fubini-Angular Spectrum technique with Christopher's NLP Code for trans-axial signal formation (Beam Profile). Conditions: 2 MHz fundamental with harmonic at 4 MHz, P3-2 transducer in water, at 4 cm penetration. The black curves were generated by Christopher's NLP code. The red curves were generated using NUPROP's Fubini-Angular Spectrum Technique.

Another feature readily apparent from Figure 5-6 is the trans-axial distance associated with the main lobes of the fundamental and harmonic beam profiles. The second harmonic main lobe's trans-axial extent is approximately half of the fundamental, suggesting that the second harmonic will yield improved lateral resolution. It should be noted that the second harmonic is normalized relative to its maximum value, readily comparing the main lobe beam widths. Typically, the second harmonic signal strength is several dB's lower than the fundamental.

Image Formation

Figure 5-7 shows a comparison of NUPROP's image generation for a point source under the conditions specified in Bamber and Dickinson [1980]. The images on the left are for envelope detected signal and RF signal (top and bottom, respectively). The images on the right are from NUPROP's simulation of point source images, envelope detected and RF (top and bottom,

respectively). The white boundaries designate the 3dB, or half power, contour for the envelope and RF signals, assuming symmetric pulse shape. Bamber and Dickinson's data exhibit a "skewed" distribution because of the non-symmetric rise and fall time of their temporal apodization function. The inscribed contour is associated with the more gradual fall off. NUPROP assumes a symmetric rise and fall time for its temporal apodization function. As is readily apparent by this comparison, NUPROP produced RF and envelope detected signals comparable with Bamber and Dickinson.

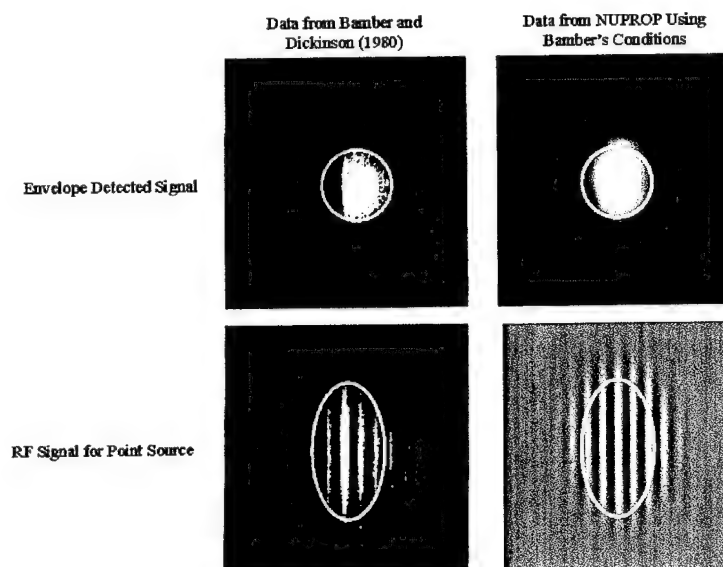


Figure 5-7. Comparison of NUPROP simulation of a point source signal using conditions described in Bamber and Dickinson [1980] and data from Bamber and Dickinson [1980]. The inscribed boundaries (white circle [top] and ellipse [bottom]) are associated with the 3dB, or half power, contours.

Chapter 5: Summary

NUPROP's nonlinear wave generation and propagation results compared favorably with data found in literature, having less than one percent difference comparing NUPROP's Fubini implementation with existing data (Ryan, [1963] and less than a few percent between NUPROP's Burgers' solution and existing data. NUPROP also accurately predicted on-axis wave amplitude for propagation distances comparable to Averkiuo's simulation conditions. Additionally,

NUPROP confirmed Averkiuo's supposition that, for equivalent areas, circular transducers produce equivalent on-axis longitudinal amplitudes as rectangular arrays (P3-2 geometry). However, NUPROP also showed that for wave or field amplitudes off-axis, Averkiuo's assumption is invalid.

In comparing trans-axial beam profiles derived from diffraction coupled with nonlinear propagation, NUPROP compared very favorably with literature (Christopher, [1997]), having less than a few percent difference in trans-axial beam profile amplitudes for 2 MHz and its second harmonic at 4 MHz, within 1.5 cm radial distance from the axis.

Comparing NUPROP's RF and envelope detection simulated images with Bamber's technique for a point source. Bamber's simulation used a "skewed" or non-symmetric temporal pulse shape, whereas NUPROP assumes a temporally symmetric beam apodization. Comparing the 3 dB point for the most gradual fall-off, NUPROP is within one percent in computing the half power point, or 3 dB down from maximum intensity.

Given the favorable comparison of NUPROP's simulations of nonlinear wave generation and propagation using Fubini or Burgers' partial differential equation solutions, linear wave propagation (diffraction) using angular spectrum or Lommel formulation, and image formation using Bamber's technique, verification of NUPROP's viability as a simulation code is complete.

Chapter 6. Exercising NUPROP

This chapter discusses variations of NUPROP parameters and the effect of variations on signal and image generation. Parameters of interest include computational, scenario or environmental, object, and system parameters as depicted in Figure 6-1.

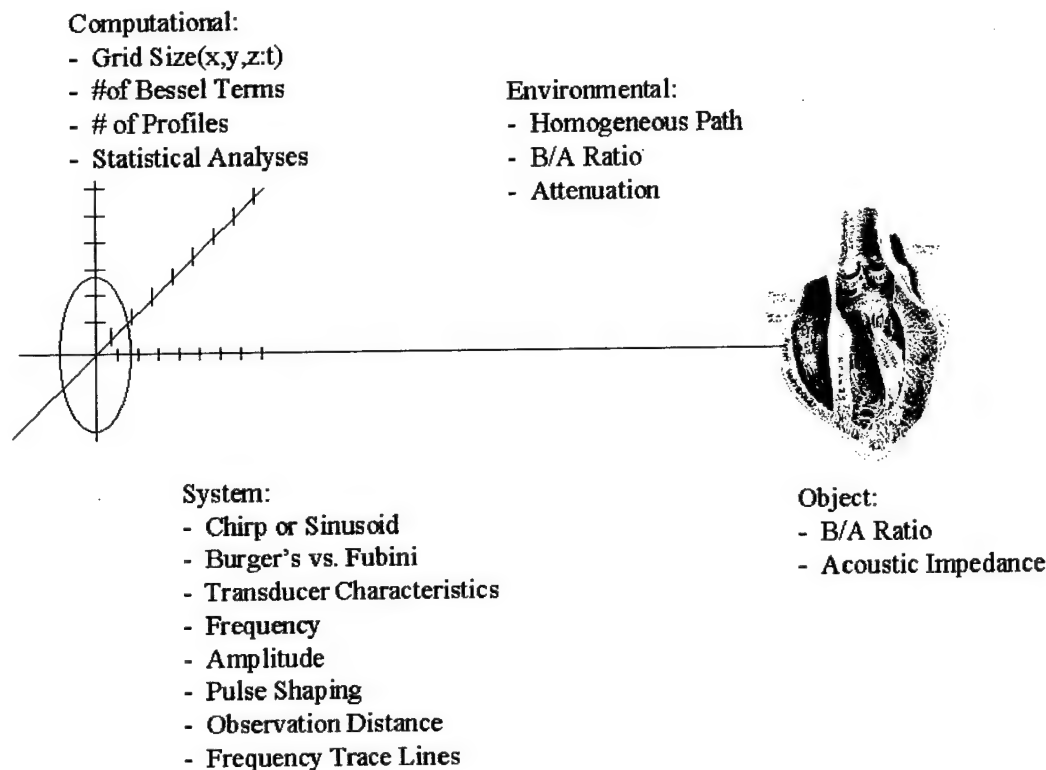


Figure 6-1. Graphical representation of NUPROP variables. Computational variables govern the size of the computational space allocated for signal and image generation. Environmental variables govern path constituency and attenuation. Object variables govern signal interaction. System variables govern input type, nonlinear and linear propagation modeling types, transducer characteristics, path observation depth, and trace lines for frequency representational graphs. Image of heart from *Gray's Anatomy*, New York: Bounty Books, p. 467, 1977.

For signal generation results, namely onset distance computations, no longitudinal or temporal apodization effects are imposed. Thus, the input signal is a single frequency sinusoid. For image formation results, a pulsed or narrowband sinusoid input signal is used. Care is taken to ensure that the narrowband results do not possess frequency overlapped signals.

By this, the second and subsequent harmonic signals are band limited in such a way as to reduce the potential of transferring energy between frequencies. Figure 6-2 illustrates this concept. Assuming that the temporal apodization is Gaussian with exponent 2, then the band about each frequency must be constructed such that the overlap between frequency bands is minimized. This will ensure that the assumption of coherent addition applies to the sum signal for the overall signal comprised of fundamental, second, and subsequent harmonics.

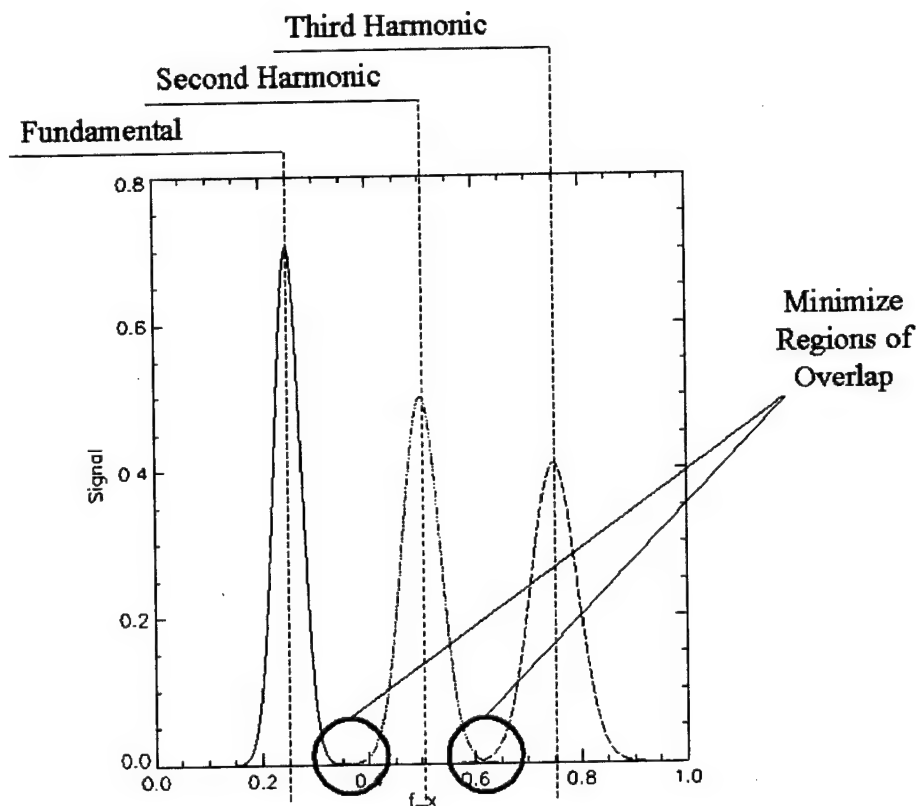


Figure 6-2. Illustration of minimizing frequency band overlap to ensure minimum energy cross-over between frequencies. By minimizing the overlaps, the coherent summation of frequency components within the nonlinearly generated signal is valid.

Single Frequency Sinusoid: Onset Distance Computation

This section discusses the effects of varying B/A ratio and path attenuation on signal and image generation. For examples in this section, the following parameters were held constant and

constituted a point of reference for signals and images generated varying B/A ratio and path attenuation:

Parameter	Value
Time:	40 μ s
Distance:	10 cm
Velocity:	1500 m/s
Transmit Frequency:	1.0 MHz
Amplitude:	0.5 MPa
# of Bessel Terms:	4
Window Factor:	0.5
XY Size:	256
Z Size:	256
Observation Distance:	32
T Size:	512
# of Beam Profiles:	8
Aperture Radius:	6.5 mm
FOV:	10 cm
X-Size:	22.5 cm
Y-Size:	15 cm
Line Trace:	50
Transducer	
Center Frequency:	2.5 MHz
Bandwidth:	1.5 MHz
Exponent:	2
SNR	5×10^9
Chirp	
Start Frequency	0.5 MHz
Gauss Modifier	3.5×10^4
Time Scale Factor	1.0
Rate Modifier	1.5×10^{11}
Continuous Wave	

Effects of B/A Ratio and Path Attenuation Variation on Onset Distances for Second and Third Harmonic Signal Generation

One measure of harmonic frequency generation is the onset distance. Onset distance is defined as the distance at which a given harmonic signal first reaches five percent of its maximum value. Figures 6-3 through 6-5 are log-linear plots. If changes in parameter values produce linear dependence of onset distance in this representation space, then the process is said to be first order,

with the slope of the trace being a measure of the rate constant. First order processes can be represented as a negative exponential

$$f(\beta) = e^{-\frac{\beta}{\beta_c}} \quad (6-1)$$

Taking the natural logarithm of both sides yields

$$\ln[f(\beta)] = -\frac{\beta}{\beta_c} \quad (6-2)$$

where β_c is the process rate constant. So, graphing the logarithm of $f(\beta)$ as a function of β yields plots represented in figures 6-3 through 6-5, where the slope is inversely proportional to the rate constant associated with the process.

Figure 6-3 shows the effect of varying B/A ratio on the onset distance for a pulsed sinusoid, 1MHz center frequency, 10 μ s pulse duration. Path attenuation was set to 1×10^{-9} dB/cm/MHz. B/A ratio was varied from 5.0 to 12.0.

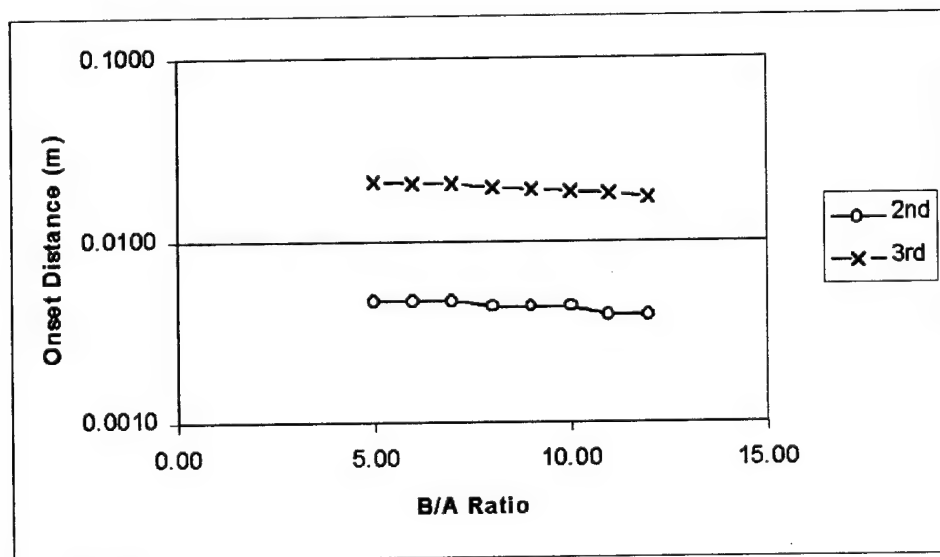


Figure 6-3. Effect of varying B/A ratio on harmonic signal onset distance. B/A ratios range from 5.0 to 12.0, typical range of biological medium (distilled water to fat). Onset distances range from 4.7 mm to 3.9 mm for second harmonic signal. Onset distances range from 2.1 cm to 1.7 cm for third harmonic signal.

These results suggest that onset distance for second and third harmonics of 1 MHz fundamental insonification are not strongly dependent on B/A ratio for typical biological medium nonlinear parameter values.

Figure 6-4 shows the effect of varying path attenuation from 1×10^{-9} to 2.0 dB/cm/MHz and B/A ratio from 5.0 to 12.0.

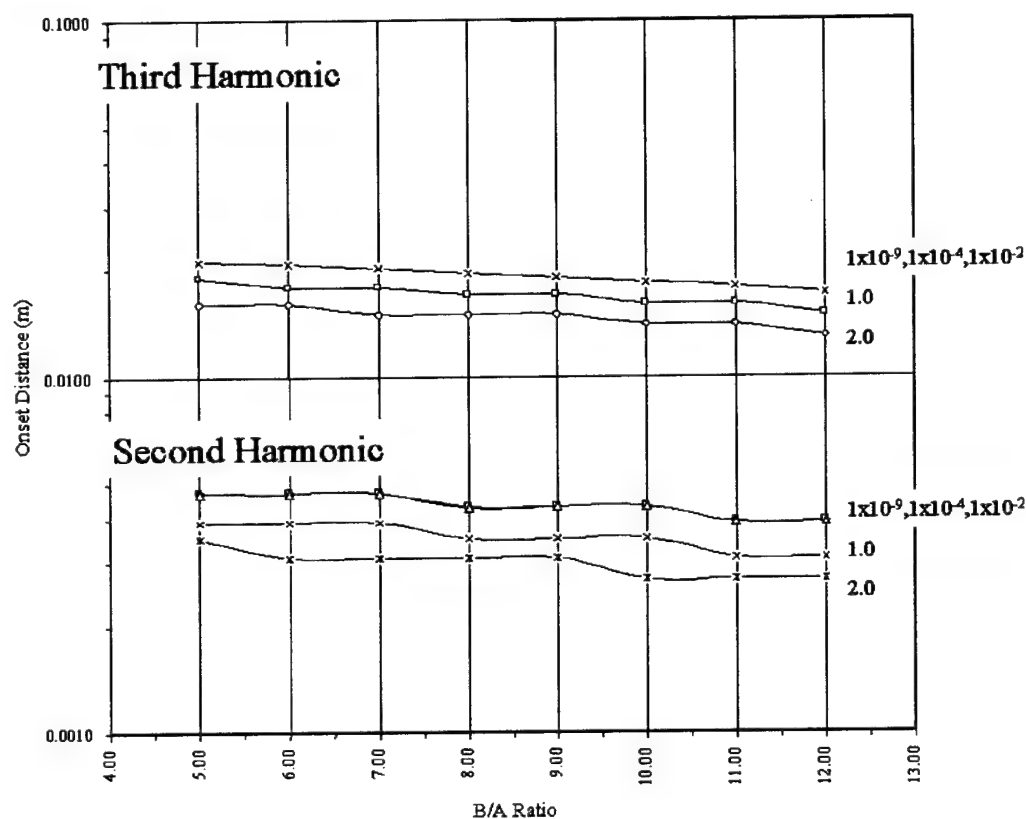


Figure 6-4. Effect of varying B/A ratio from 5.0 to 12.0, for varying path attenuation, on onset distance for pulsed sinusoid with center frequency of 1.0 MHz, pulse duration of 10 μ s.

These results suggest that as the path attenuation increases, the onset distances decrease, but only after attenuation reaches or exceeds unity. Though the curves for each path attenuation decrease as B/A ratio increases, the slope is relatively shallow, average slope of -0.034 for the second harmonic and -0.032 for the third harmonic. Again, this indicates a weak dependence of onset distance on the nonlinear parameter, a medium determined property.

Figure 6-5 illustrates the effect of varying path attenuation from 1×10^{-9} to 10, for varying B/A ratios, on onset distance of second and third harmonic signals from a fundamental frequency signal of 1.0 MHz, 10 μ s pulse duration.

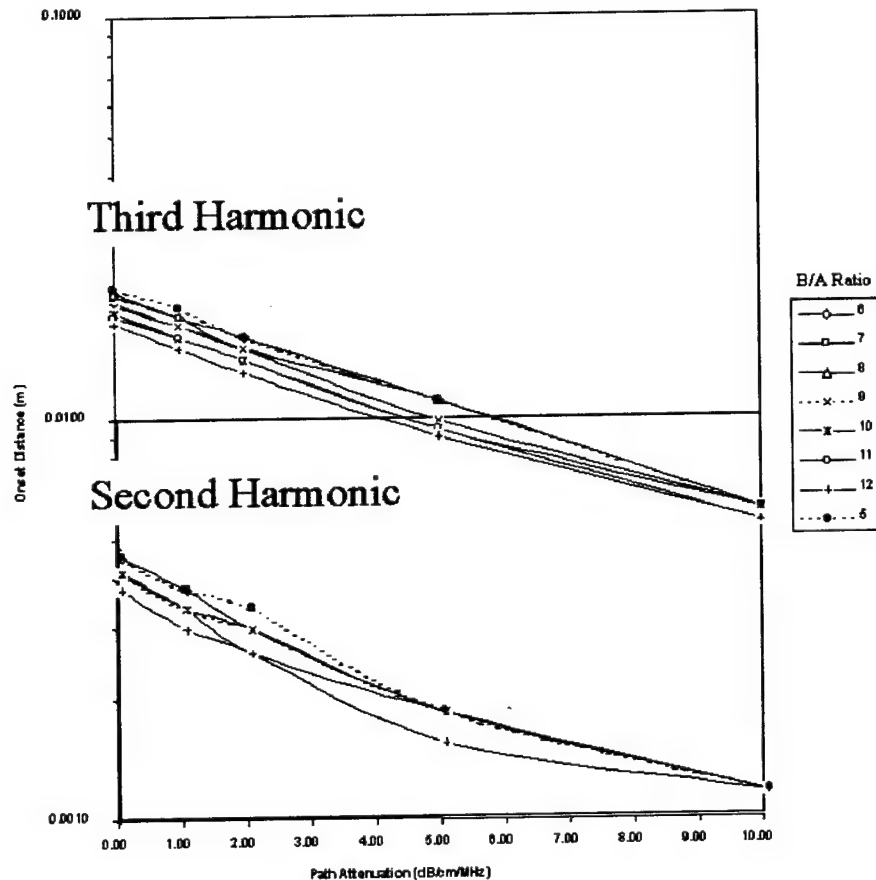


Figure 6-5. Effects of varying path attenuation on onset distance for second and third harmonic signal from a pulsed sinusoid of 1.0 MHz, 10 μ s pulse duration. Note that as path attenuation increases, onset distance decreases in a "pseudo-first order" manner as a function of path attenuation.

As the results in Figure 6-5 suggest, the onset of the third harmonic is a first order process, whereas the onset distance for the second harmonic appears to be higher order, perhaps second order. Apparently, there are at least two competing mechanisms for second harmonic onset distance. The first mechanism dominates the process for path attenuation less than 5.00 dB/cm/MHz and the second mechanism dominating for path attenuation greater than 5.00 dB/cm/MHz. Further investigation is warranted for this condition.

Effects of Varying Input Signal Strength on Onset Distance

Figure 6-6 shows the effects of varying input signal strength on the formation of harmonics in simulated biological medium: system parameters set to the following values: wave velocity: 1500 m/s; signal attenuation: 1×10^{-9} dB/cm/MHz; B/A ratio: 7.0; signal frequency: 1.75 MHz; observation distance: 5.25 cm. As input signal strength increases, the onset distance for second and third harmonics decreases. The dependence, as suggested by the curvature of the plots, is most likely higher than first order. However, if first order is assumed, then the slopes are indicated by the dashed lines: -0.53 and -0.50 for second and third harmonics, respectively.

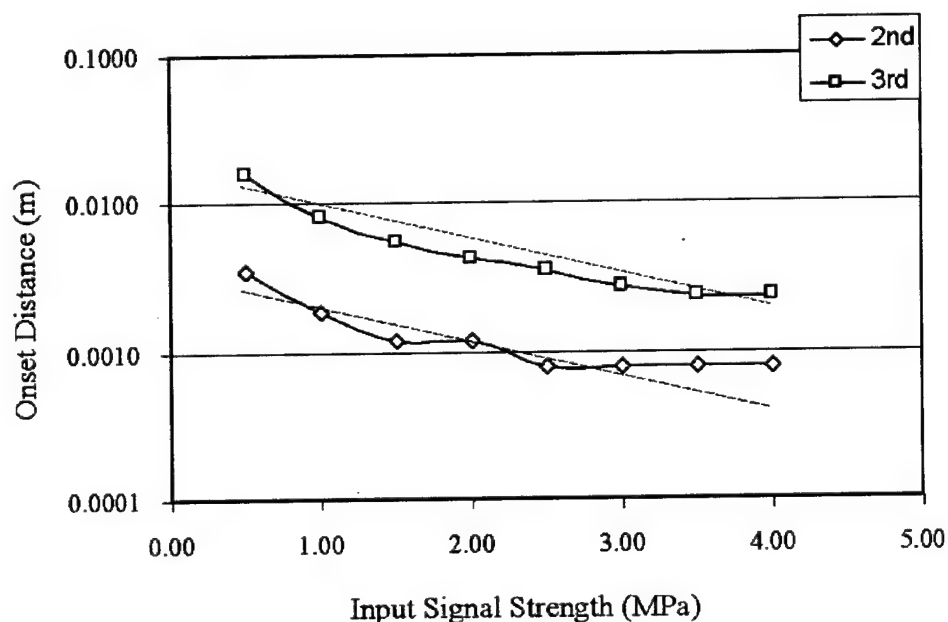


Figure 6-6. Effects of varying input signal amplitude on harmonic onset distances. Input signal strength varies from 0.5 MPa to 4.0 MPa. System parameter settings: wave velocity: 1500 m/s; frequency dependent attenuation: 1×10^{-9} dB/cm/MHz; B/A ratio: 7.0; signal frequency: 1.75 MHz; observation distance: 5.25 cm.

Effects of Varying Input Signal Frequency on Onset Distance

Figure 6-7 shows the effects of varying input signal frequency on the formation of harmonics in simulated biological medium: system parameters set to the following values: wave velocity: 1500 m/s; signal attenuation: 1×10^{-9} dB/cm/MHz; B/A ratio: 7.0; signal amplitude: 0.5 MPa; observation distance: 5.25 cm.

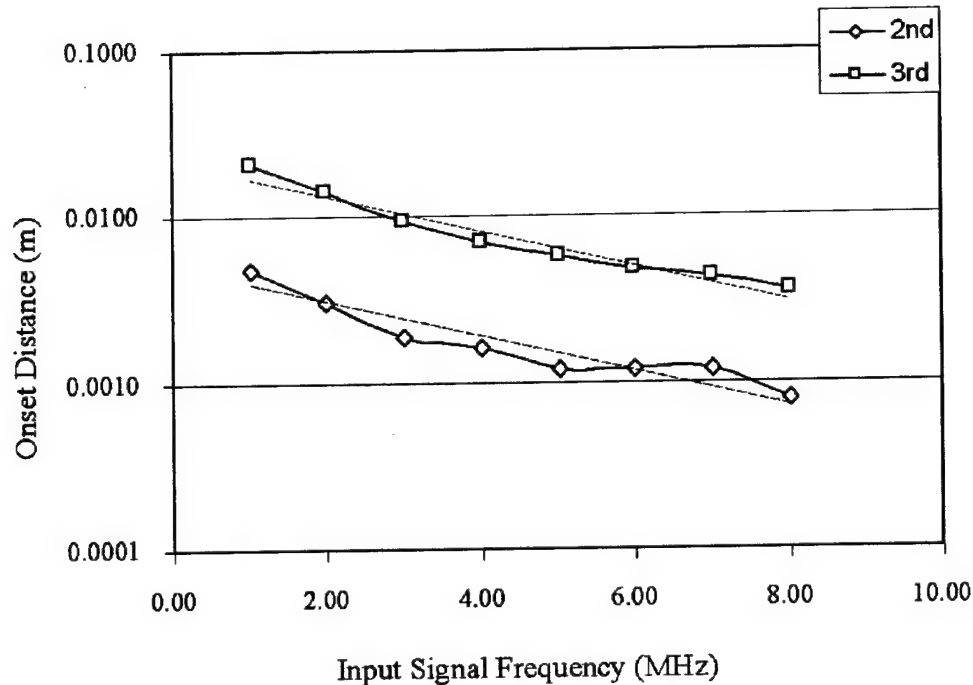


Figure 6-7. Effects of varying input signal frequency on harmonic onset distance. System parameter settings: wave velocity: 1500 m/s; frequency dependent attenuation: 1×10^{-9} dB/cm/MHz; B/A ratio: 7.0; signal input amplitude: 0.5 MPa; observation distance: 5.25 cm.

The plots in Figure 6-7 exhibit slight curvature for third harmonic onset distance dependence on input signal frequency, with significant curvature for second harmonic onset distance dependence. If first order process is assumed, then the slopes are indicated with the dashed lines: -0.45 and -0.47 for second and third harmonics, respectively.

Narrowband Sinusoid: Image Formation

This section discusses the effects of parameter variation on the formation of ultrasound B-scan images using the same computational parameters as in onset distance computation, except where the particular parameter of interest is varied.

Effects of Frequency Variation on Image Generation

Figure 6-8 shows the NUPROP phantom generation module (see also Figure 4-3). The phantom consists of three ellipses. The first ellipse (Object 1) is the largest structure (white) and

is positioned as the center of the 256x128 array, no rotational orientation. The second ellipse (Object 2) is the smallest structure (black), is rotated by -45 degrees (positive angles measured counterclockwise) and positioned 8 pixels right of center, 10 pixels above center. The third ellipse (Object 3) is the mid-sized structure (gray), centered within the 256x128 array, no rotational orientation.

Settings for Generating Ultrasound Phantom Used in Figure 6-5 Sequence

The screenshot shows the 'NUPROP: Tissue Generation Module' window. It has a menu bar with 'File' and 'Execute'. Below the menu bar, there are three main parameter sections: 'Parameters Background', 'Parameters Object 1', 'Parameters Object 2', and 'Parameters Object 3'. Each section contains several input fields for numerical values. At the bottom, there are two side-by-side simulation windows: 'Tissue Simulation' and 'Pristine Simulation'.

Parameter	Object 1	Object 2	Object 3
Nominal Level	10.	9.5	3.5
Variation Level	2.e-1	9.e-1	3.e-1
Major Axis Modifier	1.2e-1	5.e-2	1.2e-1
Minor Axis Modifier	3.5e-1	7.e-2	3.5e-1
Object Extent Modifier	9.e-1	9.e-1	7.e-1
Object Rotation Angle	0.	-45.	0.
Object Shift in X-Direction	0	8	0
Object Shift in Y-Direction	0	10	0

The 'Tissue Simulation' window shows a grayscale ultrasound image of a complex, ovoid structure with a thick, speckled outer wall and a darker, more uniform inner core. The 'Pristine Simulation' window shows a similar ovoid structure, but with a distinct, bright white outer ring and a dark, solid black center, representing the individual components of the phantom.

Figure 6-8. NUPROP Tissue Generation Module. Settings used to generate simulated ultrasound images for sequence in Figure 6-9. Three elliptical objects were generated, forming the complex tissue object. Object 1 is the outer ellipse (white). Object 2 is the small ellipse at a 45 degree angle (black). Object 3 is the inner ellipse (gray).

The tissue phantom depicts an ovoid tissue structure possessing a thick membranous wall, a tissue filled core, and a small cyst in relative positions shown in the pristine simulation. This module, with the settings shown in Figure 6-8, was used to generate the ultrasound phantom that produced the image sequence in Figure 6-9.

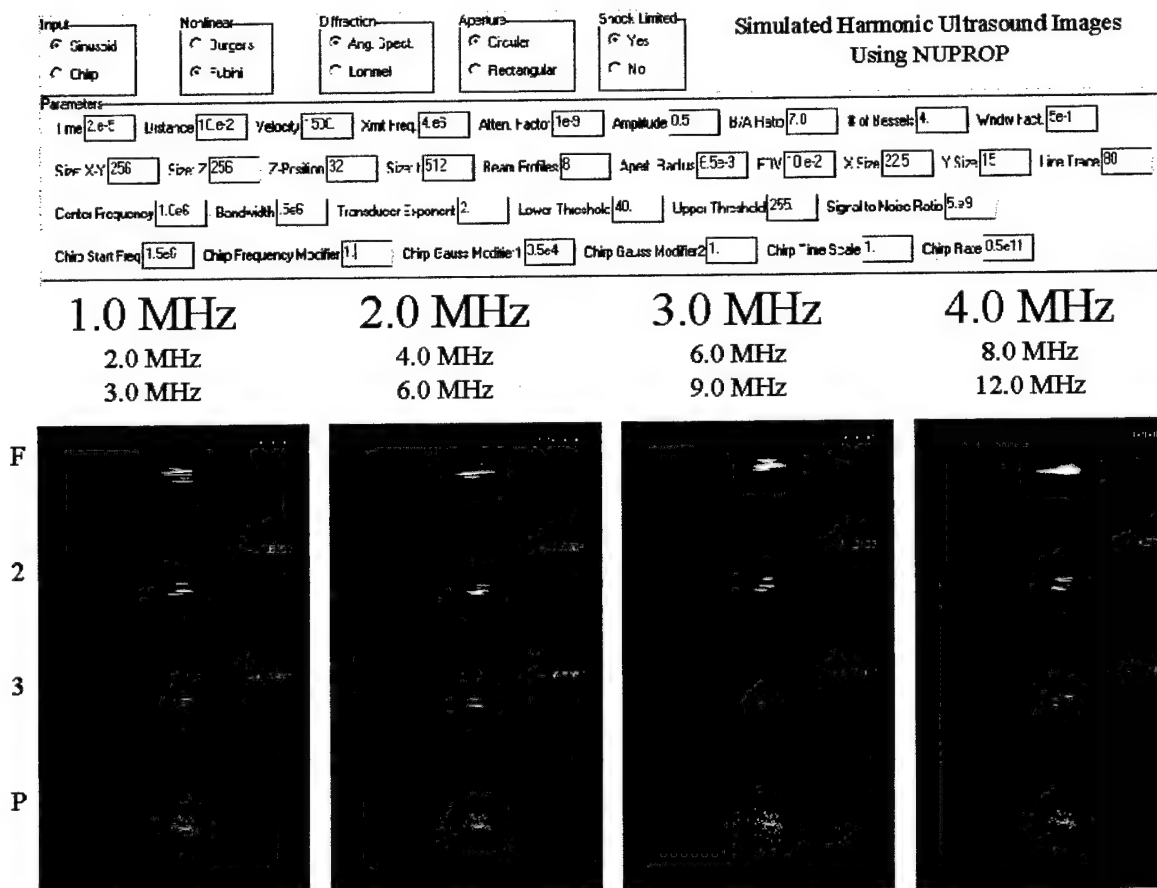


Figure 6-9. Effects of varying center frequency of a narrow-band sinusoidal ultrasound pulse on simulated image formation. Conditions that generated this sequence of images are specified. Frequency was varied from 1.0 MHz to 3.0 MHz. Fundamental (F); Second Harmonic (2); Third Harmonic (3); and Phantom (P).

Figure 6-9 shows that, as the initial center frequency (Fundamental) increases from 1.0 MHz to 4.0 MHz, the image resolution improves. The structure's membranous wall is resolved at 4.0 MHz. The membranous wall is also resolved at the 2.0 MHz second harmonic frequency. This suggests, for this particular phantom, that the membranous wall possesses a high correlation with 4.0 MHz signals.

The target cyst is detectable at all four fundamental frequencies, with the "best" detectability at 3.0 MHz. Detectability, in this case, is defined as the highest, localized intensity "spot" in the image. The cyst is localized in the harmonic images of each frequency as well, with the "best" localization occurring at 1.0 MHz second harmonic and 3.0 MHz second harmonic.

The 2.0 MHz second harmonic image (4.0 MHz) shows marked improvement in longitudinal resolution over the 4.0 MHz fundamental image. This result is not unexpected, since literature is replete with actual experimental results suggesting this improvement. The average signal strength of the second harmonic image, from 1.0 MHz to 4.0 MHz, is -14.3 dB. The average signal strength of the third harmonic image, over the same frequency spread, is -21.4 dB.

Effects of Varying B/A Ratio on Image Generation.

Figure 6-10 shows the effect of varying B/A ratio on image generation using a narrowband sinusoid with center frequency of 1.75 MHz, initial amplitude of 0.5 MPa, velocity of 1500 m/s, and frequency dependent attenuation of 1×10^{-9} dB/cm/MHz. The phantom used is shown in the upper right corner. Images associated with the fundamental, second harmonic, and third harmonic are represented in columns 1, 2, and 3, respectively. B/A ratios of 5, 6, and 10 were used (rows 1, 2, and 3 respectively). Images associated with the difference between B/A ratio 5 and 6, 5 and 10, and 6 and 10 for the fundamental, second harmonic, and third harmonic simulations are presented in rows 4, 5, and 6, respectively. Difference images are presented in dB scale.

The B/A ratio has very little effect on the fundamental image, as is readily apparent in the difference images in Figure 6-10. The effect is most prominent for the third harmonic difference images, with the second harmonic exhibiting some small differences as well. In each case for the fundamental and second harmonic image differences, however, the differences are negligible.

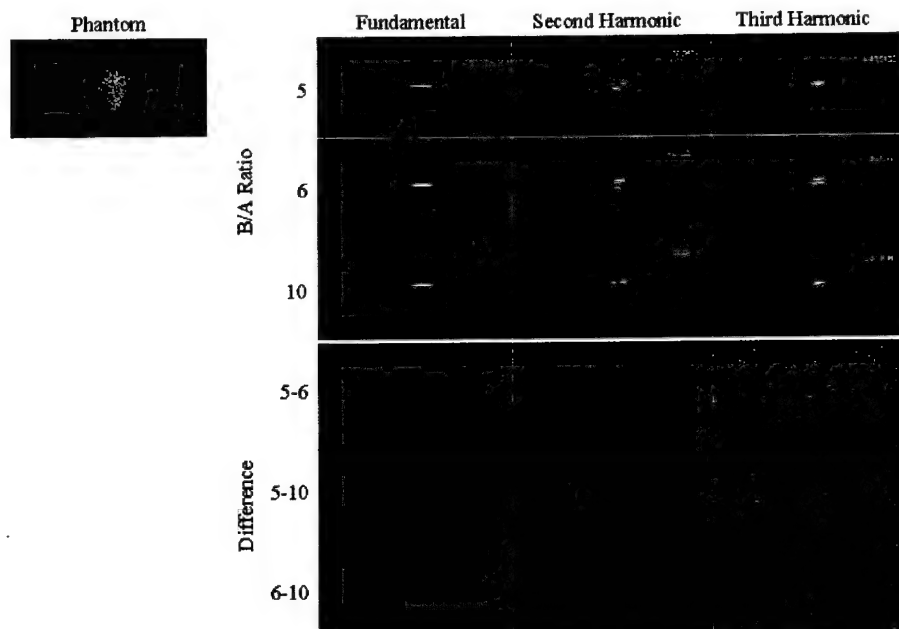


Figure 6-10. Effects of varying B/A ratio on simulated ultrasound images. The phantom used is shown in upper right corner. Images associated with fundamental, second harmonic, and third harmonic are shown in columns 1, 2, and 3, respectively. B/A ratios of 5, 6, and 10 are rows 1, 2, and 3, respectively. Difference images 5 - 6, 5 - 10, and 6 - 10 are shown in rows 4, 5, and 6, respectively. Difference images are presented in dB.

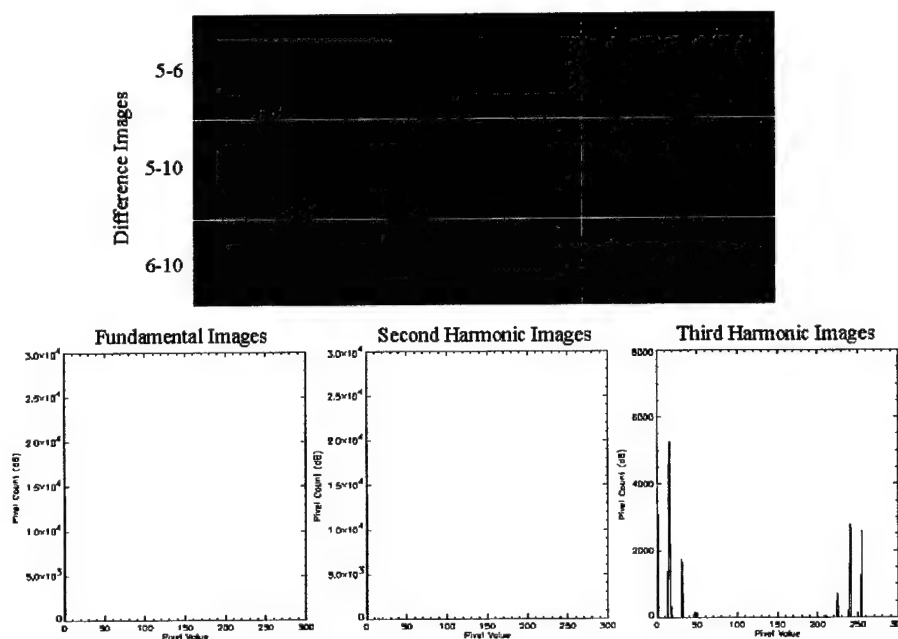


Figure 6-11. Histogram of Difference images in Figure 6-8. The difference images from Figure 6-7 are redisplayed. The histogram of the fundamental image differences, second harmonic image differences, and third harmonic image differences are presented. The third harmonic difference image histogram shows appreciable distribution, whereas the fundamental and second harmonic difference image histograms essentially show no difference.

Figure 6-11 shows the histogram of the difference images, further confirming the negligible differences between fundamental images and second harmonic images, with appreciable differences appearing in the third harmonic difference images. It should be noted that, for third harmonic images, the maximum signal levels range from -44.56 to -40.77 dB over the span of B/A ratios presented in Figure 6-10.

The effect of varying B/A ratio is manifested in the overall dB level for the second and third harmonic images. As the B/A ratio increases, the relative signal strength increases as shown in Figure 6-12.

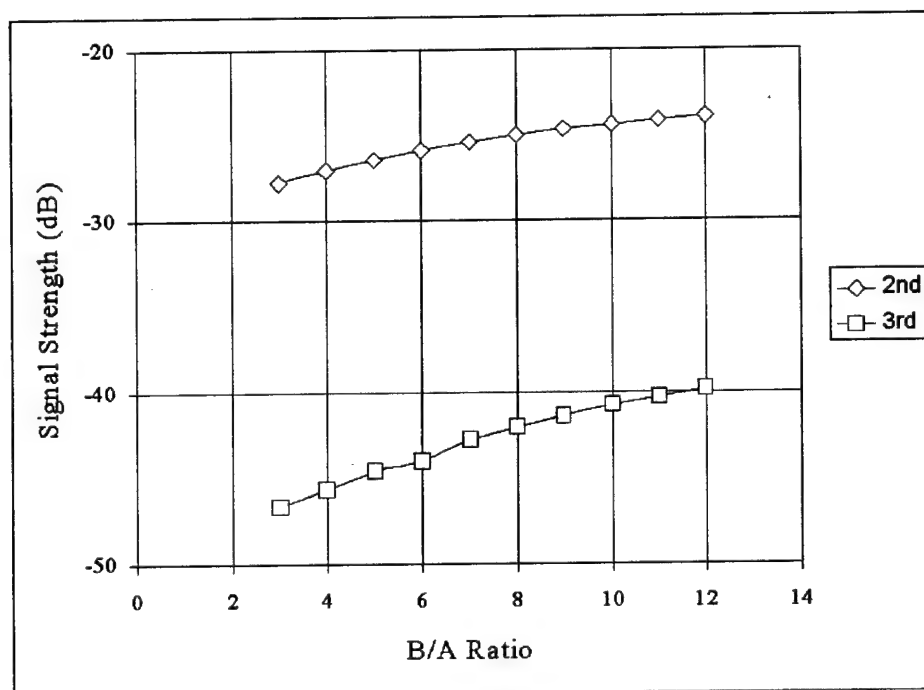


Figure 6-12. Effect of varying B/A ratio on signal strength for images generated using 1.75 MHz center frequency, narrowband sinusoid insonification: signal amplitude: 0.5 MPa; observation depth: 4.2 cm; velocity: 1500 m/s; no appreciable frequency dependent attenuation.

Figure 6-12 suggests that for typical biological tissue types, the second and third harmonics will require at least -27.79 to -23.92 dB and -46.67 to -39.79 dB of gain compensation, respectively, to produce comparable ultrasound images as shown in Figure 6-10, given the phantom used.

Effects of Varying Signal Amplitude on Image Formation

Figure 6-13 shows the effects of varying the input signal amplitude on image formation. Signal amplitudes of 1.0, 2.0, and 3.0 MPa with wave velocity of 1500 m/s, signal attenuation of 1×10^{-9} dB/cm/MHz, observation distance of 2.5 cm. The images generated at each frequency were pair-wise differenced: 1.0 – 2.0 MPa, 1.0 – 3.0 MPa, and 2.0 – 3.0 MPa. As can be readily seen, signal amplitude has little apparent visual effect on the fundamental and second harmonic difference images, as is confirmed by the difference images' histogram plots. The primary effect is in the overall signal strength, in dB. The second harmonic images have signal strengths of -19.6 dB, -22.0 dB, and -23.0 dB for 1.0, 2.0, and 3.0 MPa input signal amplitudes, respectively.

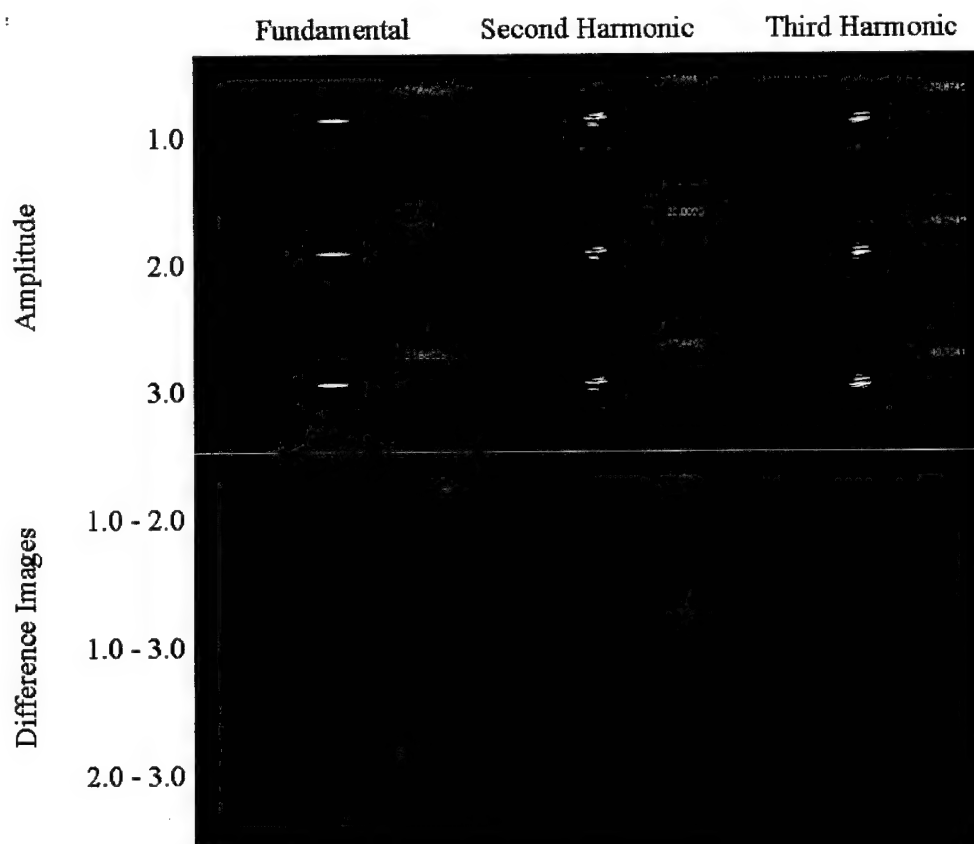


Figure 6-13. Effects of varying signal amplitude on image formation. Input signal strengths of 1.0 MPa, 2.0 MPa, and 3.0 MPa were used. System parameters were set as follows: wave velocity: 1500 m/s; B/A ratio: 7.0; observation distance: 2.5 cm; frequency dependent attenuation; 1×10^{-9} dB/cm/MHz.

Differences in images can be detected at the third harmonic, where the histogram plot reveals at the high and low ends of the intensity levels, as evidenced in Figure 6-14. Again, the primary difference between the three input signal strength images is manifested in the overall signal strength: -29.3 dB, -39.5 dB, and -40.3 dB for 1.0, 2.0, and 3.0 MPa input signal strengths, respectively.

Difference Images for Amplitudes of 1.0, 2.0, and 3.0 MPa

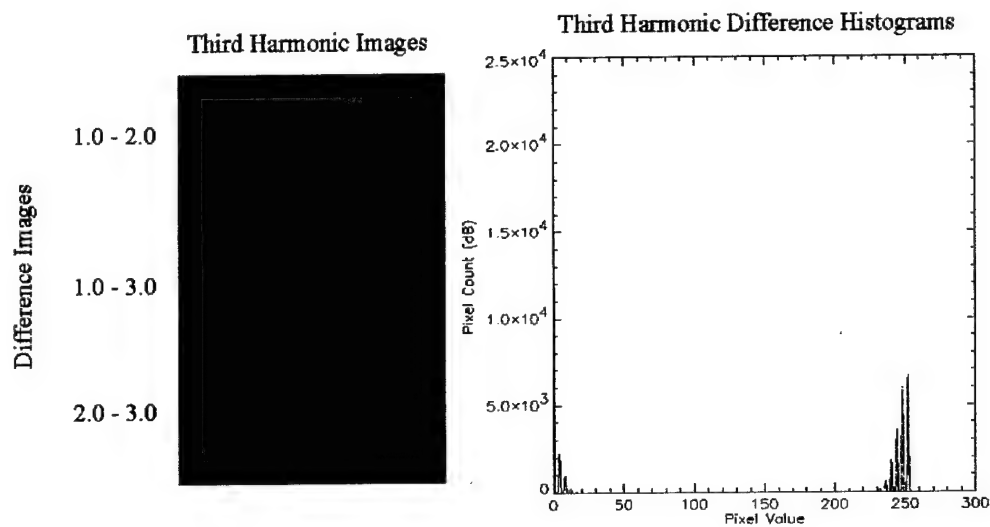


Figure 6-14. Difference images and histograms associated with third harmonics for 1.0, 2.0, and 3.0 MPa signal amplitudes. Differences between fundamentals and second harmonics were negligible. System parameters were set as follows: wave velocity: 1500 m/s; B/A ratio: 7.0; observation distance: 2.5 cm; frequency dependent signal attenuation: 1×10^{-9} dB/cm/MHz.

The histogram in Figure 6-14 suggests that the differences are primarily due to noise at the lower end of the pixel value distribution, whereas differences at the high end of the pixel distribution may be attributable to actual image differences. In either case, the range of values where little to no differences occur in the third harmonic difference images, namely 15 to 230 in a range from 0 to 255, suggests that these differences are negligible as well.

Effects of Varying Wave Velocity on Image Formation

Figure 6-15 shows the effects of varying wave velocity on the formation of fundamental, second, and third harmonic simulated images using the phantom (cyst image) generated by NUPROP (see Figure 6-8). The system parameters were as follows: input signal amplitude: 0.5 MPa; B/A ratio: 7.0, observation distance: 2.5 cm; frequency dependent attenuation: 1×10^{-9} dB/cm/MHz. Wave velocity was varied from 1400 to 1600 m/s, in 100 m/s increments. As is apparent from the images in Figure 6-15, there is very little visual difference between fundamental images (1400 – 1500 m/s, 1400 – 1600 m/s, and 1500 – 1600 m/s) and second harmonic images (fundamental at 1400 minus fundamental at 1500 m/s, fundamental at 1400 minus fundamental at 1600 m/s, and fundamental at 1500 minus fundamental at 1600 m/s) and second harmonic images (second harmonic at 1400 minus second harmonic at 1500 m/s, second harmonic at 1400 minus second harmonic at 1600 m/s, and second harmonic at 1500 minus second harmonic at 1600 m/s).

Differences are apparent at the third harmonic as illustrated in Figure 6-16. Although the actual difference images do not exhibit much variation, the histograms of the difference images reveal significant difference in third harmonic at 1400 m/s minus at 1500 m/s third harmonic, third harmonic at 1400 m/s minus third harmonic at 1500 m/s, and third harmonic at 1500 m/s minus third harmonic at 1600 m/s. The differences occur at the periphery of the distributions, suggesting, at the lower end of pixel values, the differences are approaching the noise floor of the process, whereas, at the high end of the pixel value distribution, the variation is due to actual differences in image content. So, over a relatively broad range of pixel values, approximately 40 to 180 in a range from 0 to 255, the differences in third harmonic images for the combinations of the three velocities is negligible.

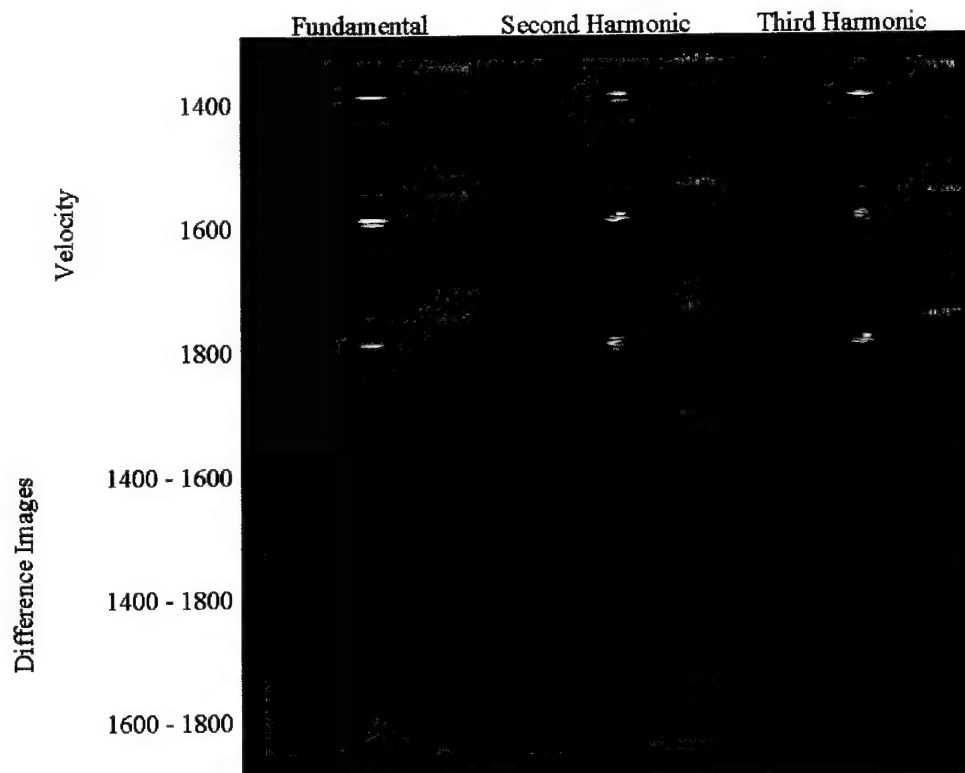


Figure 6-15. Effects of varying wave velocity on image formation. As apparent in the images, very little difference exists between the fundamental and second harmonic images of varying velocities. Differences are manifested in the third harmonic image.

Difference Images for Velocities of 1400, 1500, and 1600 m/s

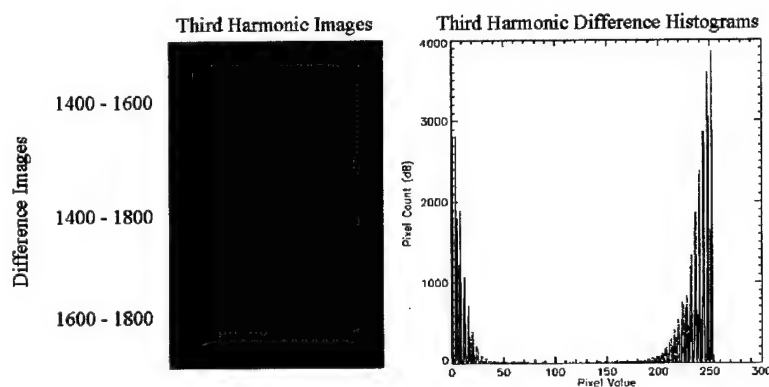


Figure 6-16. Difference images and histograms associated with third harmonics for 1400, 1500, and 1600 m/s wave velocities. Differences between fundamentals and second harmonics were negligible.

The Apodized Chirp: Experiment versus NUPROP modeling

Up to this point, discussions have either been concerned with single frequency sinusoidal input signals to determine fundamental characteristics such as harmonic onset distances and beam profiles at various penetration depths; or with narrowband (multi-frequency) sinusoidal input signals typically used for tissue imaging (B-Scan formation).

One novel approach is the use of a linear frequency modulated sinusoid or the chirp. Appendix III discusses NUPROP's implementation of nonlinear chirps and their efficacy. This section compares NUPROP simulation of an apodized chirp with experimental data.

Figure 6-17 shows the basic frequency modulated sinusoid or chirp signal. Each signal represented exhibits the characteristic "sawtooth" structure indicative of harmonics present in the waveform. Note also that the "real" signals have a higher maximum positive value than maximum negative value whereas the "imaginary" signals are symmetric about zero amplitude. Even so, the mean amplitude value for either "real" or "imaginary" signals is zero.

Each harmonic frequency within the propagated chirp signal adds "in-phase" such that the zero crossings remain fixed throughout the harmonic generation process. Another indicator that the harmonics are adding "in-phase" is that, within each chirp cycle, the waveform is sawtoothed. In other words, if any appreciable dispersion existed within the propagated chirp signal, the coherent nature of the waves would necessarily possess destructive interference, causing the waveform to be severely disrupted. Figure 6-18 illustrates this point. The smaller circled areas show where the zero crossings are changed. The larger circled area shows where the signal exhibits destructive interference.

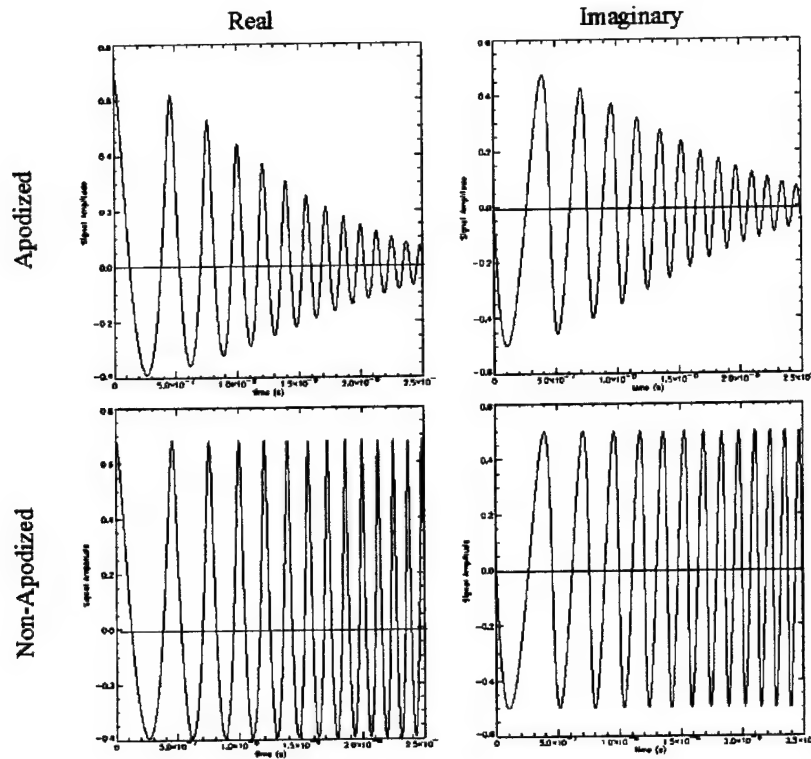


Figure 6-17. Examples of apodized and non-apodized linear frequency modulated sinusoids. Initial frequency: 1.5 MHz, sweep rate of 1.5×10^{12} . Repeat of Figure 3-2.

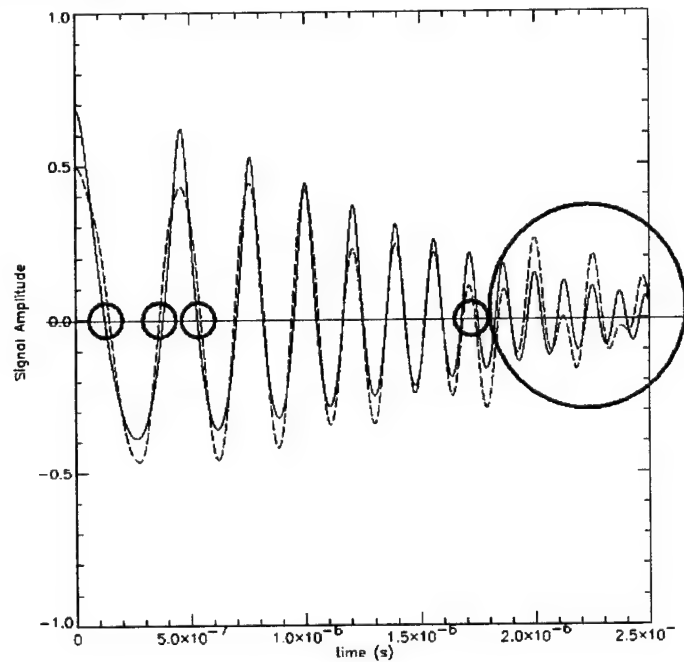


Figure 6-18. Illustration of the effects of dispersion or phase shifting and destructive interference on coherently added harmonic signals. Dispersion is indicated within the small circles. In this example, a small phase shift was added to each harmonic signal causing the harmonics to eventually add out of phase, manifested in the destructive interference at the higher frequencies, depicted in the larger circle.

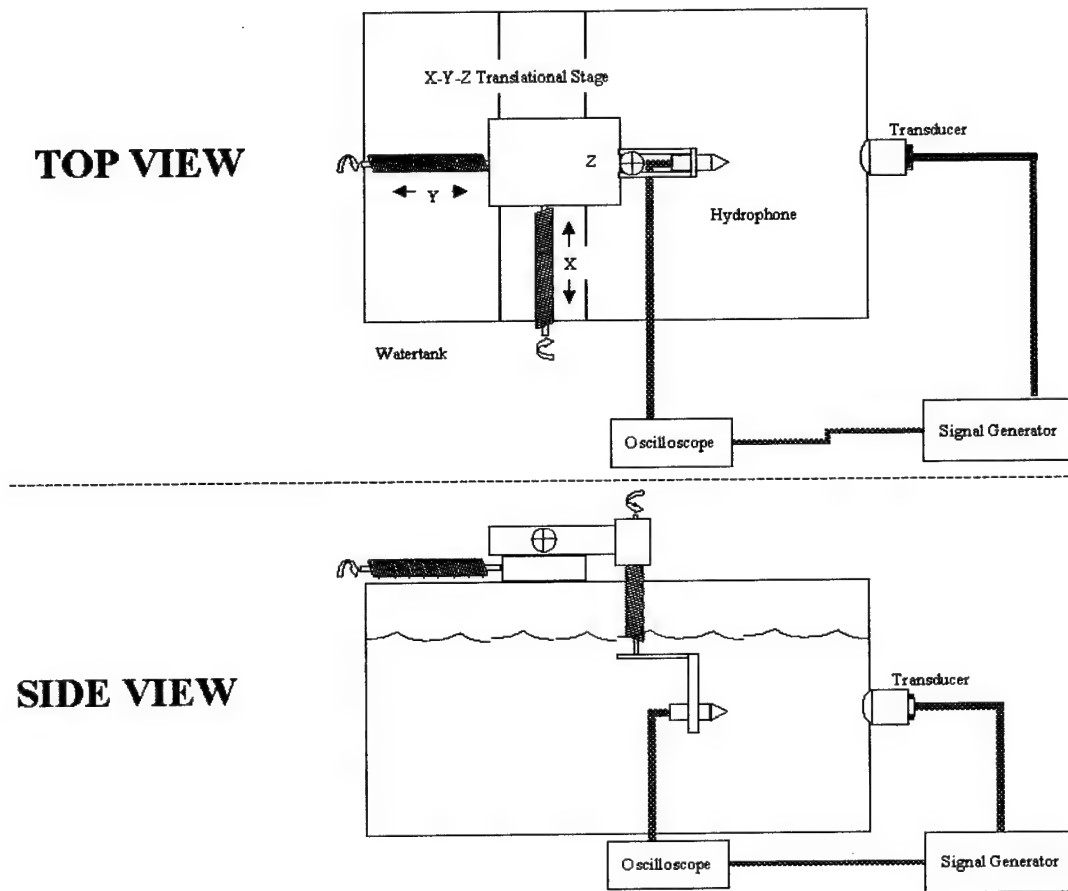


Figure 6-19. Experimental apparatus used to collect chirp signal data. The apparatus consists of a 2.5 MHz transducer acoustically coupled to the wall of the water tank. The hydrophone is attached to a X-Y-Z electronically actuated stage for precise positioning within the water tank (9.5 cm on-axis from the face of the transducer). The signal from the hydrophone and the signal generator are displayed on an oscilloscope. The signals are digitized and sent to a computer for storage (digitizer and computer not shown)

Figure 6-19 is a cartoon rendition of the apparatus used to collect the one way, on axis wave propagation data. The transducer used was a Type 280 2.5 MHz circular transducer (1.5 cm diameter). The hydrophone used was a Medisonics Mark II, gain set to zero. A Polynomial Wave Synthesizer Model 2020 was used to generate the input chirp waveform. The equation to generate the input to the transducer was

$$U(t) = 3.5 \cdot \sin \left(\int_0^{15M} \left(1.5M + \frac{1.5M}{2\mu} \right) \cdot t \, dt \right) \quad (6-3)$$

where M is 1×10^6 and μ is 1×10^{-6} .

The signal from the hydrophone was displayed using a HAME 13, 60 MHz Model HM604 Oscilloscope: x-settings: $0.1 \mu\text{s}$ delay, time division: $10 \mu\text{s}$; y-settings: $20 \text{ mV}/0.1$ division. Data was digitized using a Data Precision Model 6100B with the following settings:

x: offset: $5.40 \mu\text{s}$; scale: x1

y: offset: 0.00v ; scale: x2; $\pm 500 \text{ mV}$; AC coupled

timebase: 256 to 400 points; period: 27.7 ns ; $-1.662 \mu\text{s}$ delay

NUPROP simulation settings were as follows:

Parameter	Value
Initial Frequency, f_o	1.5 MHz
Sweep Rate, $sweep$	2.9×10^{12}
Wave Velocity, c_o	1500 m/s
Nonlinear Parameter, β	5.0
Initial Wave Amplitude, U_o	3.5 MPa
Rayleigh Distribution Factor, α	1.1×10^6

The shock parameter distance, L , was calculated using equation 3-8. Each distance dependent amplitude modifier was calculated using

$$A_n = \frac{2 \cdot U_o \cdot L}{n \cdot z} \cdot J_n \left(\frac{n \cdot z}{L} \right) \quad (6-4)$$

where n is the frequency subscript (i.e. fundamental equals 1, second harmonic equals 2, etc.) and z is the observation distance.

Each constituent chirp was computed using

$$U_n = A_n \cdot U_o \cdot e^{-i2\pi n(f_o + sweep \cdot t) \cdot t} \quad (6-5)$$

The experimental data, waveform at the observation distance of 9.5 cm, exhibited a skewed distribution introduced by the transducer. So, an apodization function based on the Rayleigh distribution was used such that

$$Apodization = \frac{t}{\alpha^2} e^{-\frac{t^2}{2\alpha^2}} STEP(t) \quad (6-6)$$

where $STEP(t)$ is defined as

$$STEP(t - t_o) = \begin{cases} 1, & \text{for } t > t_o \\ 0.5, & \text{for } t = t_o \\ 0, & \text{for } t < t_o \end{cases} \quad (6-7)$$

with t_o equal to zero for this example. The final relationship for each chirp constituent then was computed using

$$\begin{aligned} CHIRP_n &= Apodization \cdot U_n \\ &= \frac{t}{\alpha^2} e^{-\frac{t^2}{2\alpha^2}} STEP(t) \cdot \frac{2 \cdot U_o^2 \cdot L}{n \cdot z} J_n\left(\frac{n \cdot z}{L}\right) \cdot e^{-i2\pi(f_o + sweep \cdot t) \cdot t} \end{aligned} \quad (6-8)$$

To generate the composite signal, each constituent chirp signal, U_n , was coherently added, producing the results in Figure 6-20. The near overlay of NUPROP's simulation with experimental data confirms the hypothesis that each frequency within a given chirp sweep adds coherently and "in phase" to produce the sawtoothed waveform indicative of the presence of harmonics. Additionally, the hypothesis that the chirp could be substituted as the bases functions for the Fubini solution using the same amplitude weighting Bessel functions is confirmed.

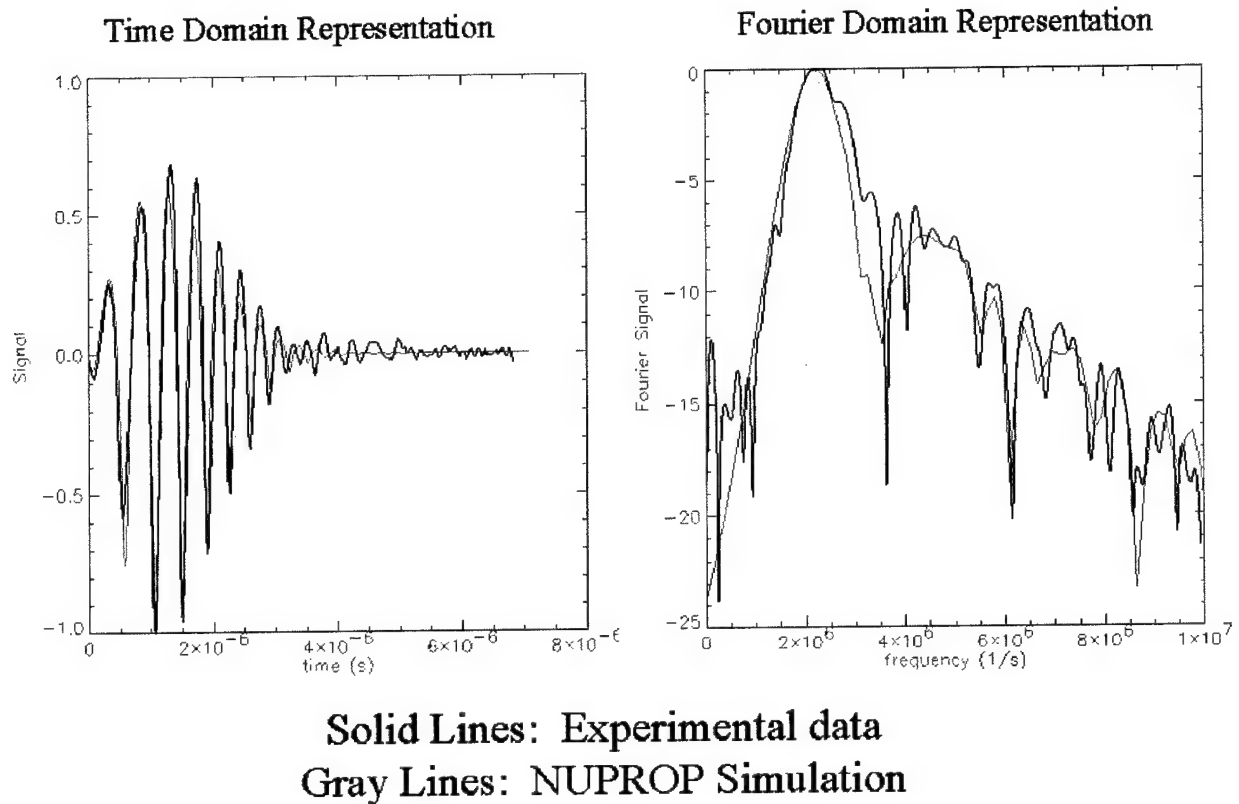


Figure 6-20 Comparison of NUPROP's simulated, apodized chirp signal and experimental data. Gray trace is NUPROP simulation, black trace is experimental data.

Figure 6-21 shows the reconstructed constituents of the chirp signal from experimental data. Each constituent within the experimental data was reconstructed from correlations between the experimental data (penetration depth of 9.5 cm) and NUPROP's apodized constituents (1.5 MHz initial frequency for the fundamental, 3.0 MHz initial frequency for the second harmonic, and 4.5 MHz initial frequency for the third harmonic) at a penetration depth of 9.5 cm. As is evident in Figure 6-21, the "fundamental" chirp (initial frequency 1.5 MHz) dominates the signature, with sufficient contributions from higher harmonics to produce the "sawtoothed" nature of nonlinearly propagated waves.

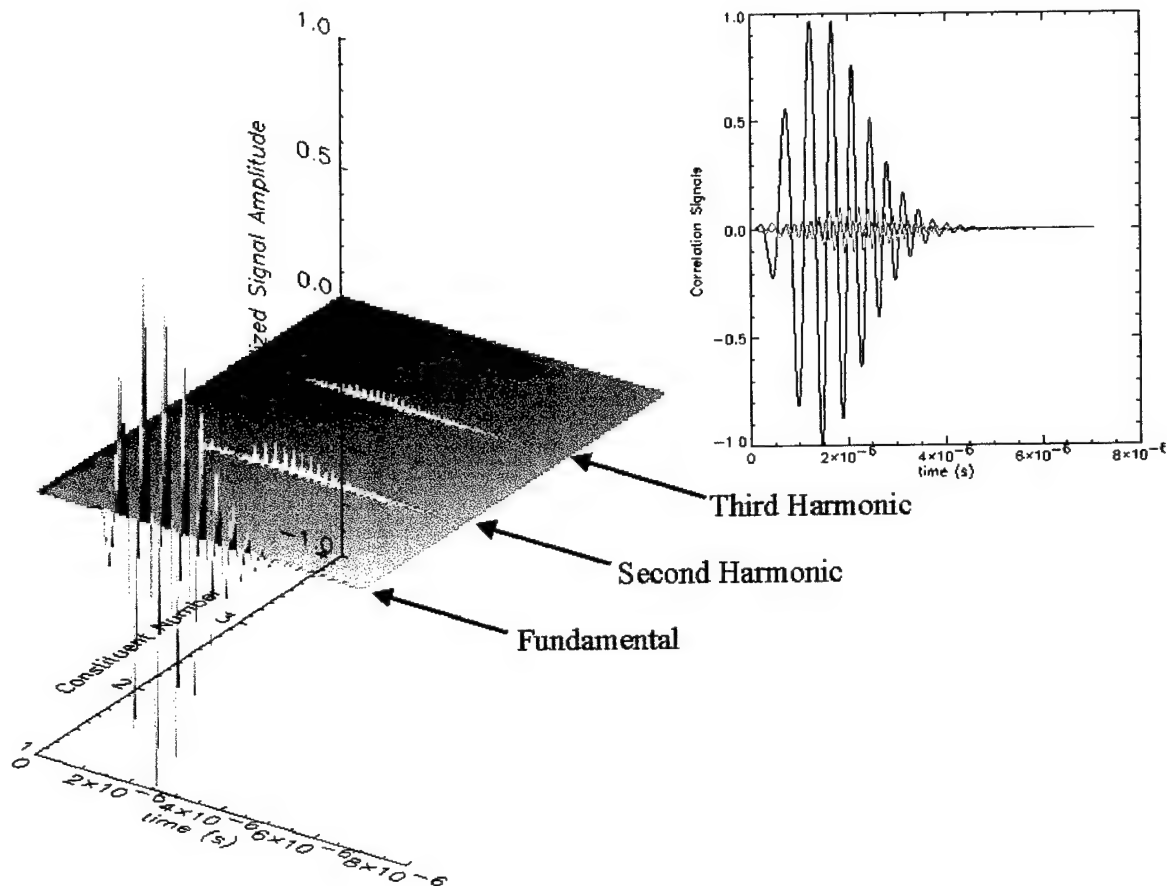


Figure 6-21. Reconstruction of experimental data's chirp constituents. Each constituent chirp is produced by correlating the experimental data with a NUPROP generated apodized chirp: fundamental chirp initial frequency, f_0 : 1.5 MHz with a sweep rate of 2.7×10^{12} , second harmonic chirp beginning at twice f_0 , and the third harmonic at three times f_0 .

Simulation: Narrowband Sinusoid versus Apodized Chirp

This section presents a comparison between the narrowband sinusoidal input signal and the apodized chirp for image reconstruction, simulations only. Figure 6-22 compares a narrowband sinusoid and an apodized chirp signal. The center frequency of the narrowband sinusoid is chosen to match the average frequency of the chirp. Additionally, the apodization of the narrowband sinusoid and the chirp produce matched bandwidths.

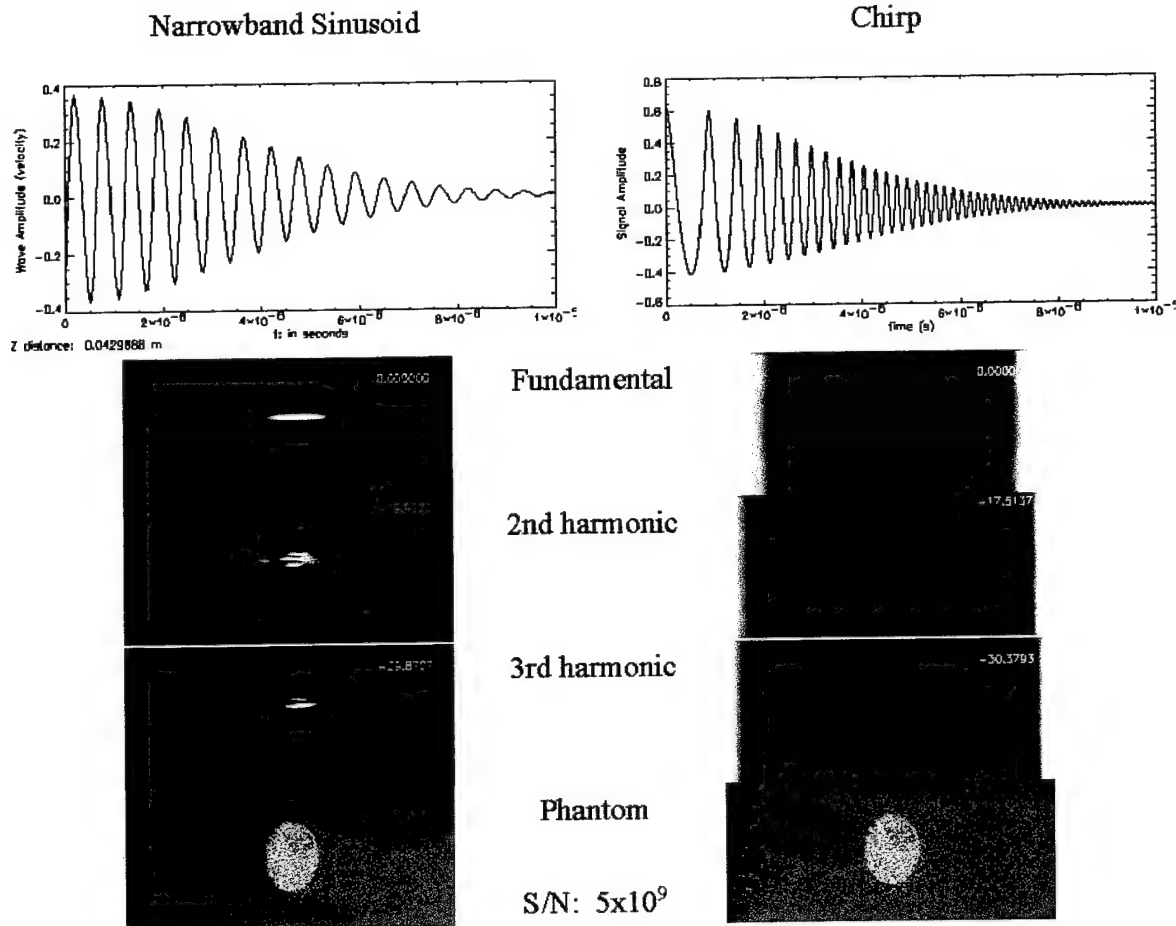


Figure 6-22. Comparison of narrowband sinusoid and apodized chirp signal simulate B-scan images with signal to noise ratio of 5×10^9 .

There is a slight gain improvement when comparing the narrowband sinusoid second harmonic image to its chirp counterpart, approximately 2 dB gain improvement. Though this may seem significant, the reconstructed B-Scan images reveal that the narrowband sinusoid produces a better quality image, where quality is measured by two properties: 1) preservation of structural integrity, where the harmonic image shows strong indicators of structure present in the phantom, and 2) detection of significantly different object types within the phantom, object discrimination. The second harmonic image for the narrowband sinusoid input exhibits strong signature returns from the cyst object within the phantom. The second harmonic image for the apodized chirp does not show such indicators. In fact, the chirp images tend to look "blurred," without strong

structural integrity, nor little to no detection between the larger ovular shapes and the cyst. So, for relatively high signal to noise ratios, the narrowband sinusoid tends to produce “better quality” B-Scan images.

The question arises, “when does the chirp produce a reasonably significant gain in image quality versus the narrowband sinusoid?” Signal to noise ratio plays a crucial part in answering this question. A block diagram of signal noise sources is illustrated in Figure 6-23.

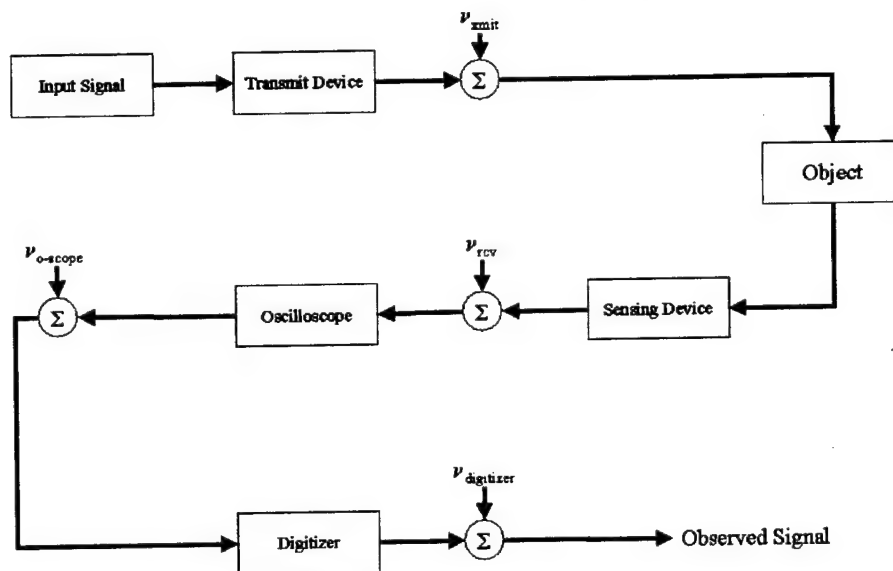


Figure 6-23. Block diagram of potential additive noise sources for an ultrasound imaging system. Noise can be introduced at each electronic device within the image reconstruction process: transmit device, sensing device, oscilloscope, and digitizer.

NUPROP models noise as a single additive quantity given by

$$V_{total} = V_{xmit} + V_{rcv} + V_{o-scope} + V_{digitizer} \quad (6-9)$$

The noise from the oscilloscope is minimal whereas the transmit, receive, and digitizer noise are significant.

Figure 6-24 illustrates the effect of decreasing signal to noise ratio on the reconstruction of images using narrowband sinusoidal and apodized chirp input. Signal to noise ratio ranges from 5×10^9 to 750.

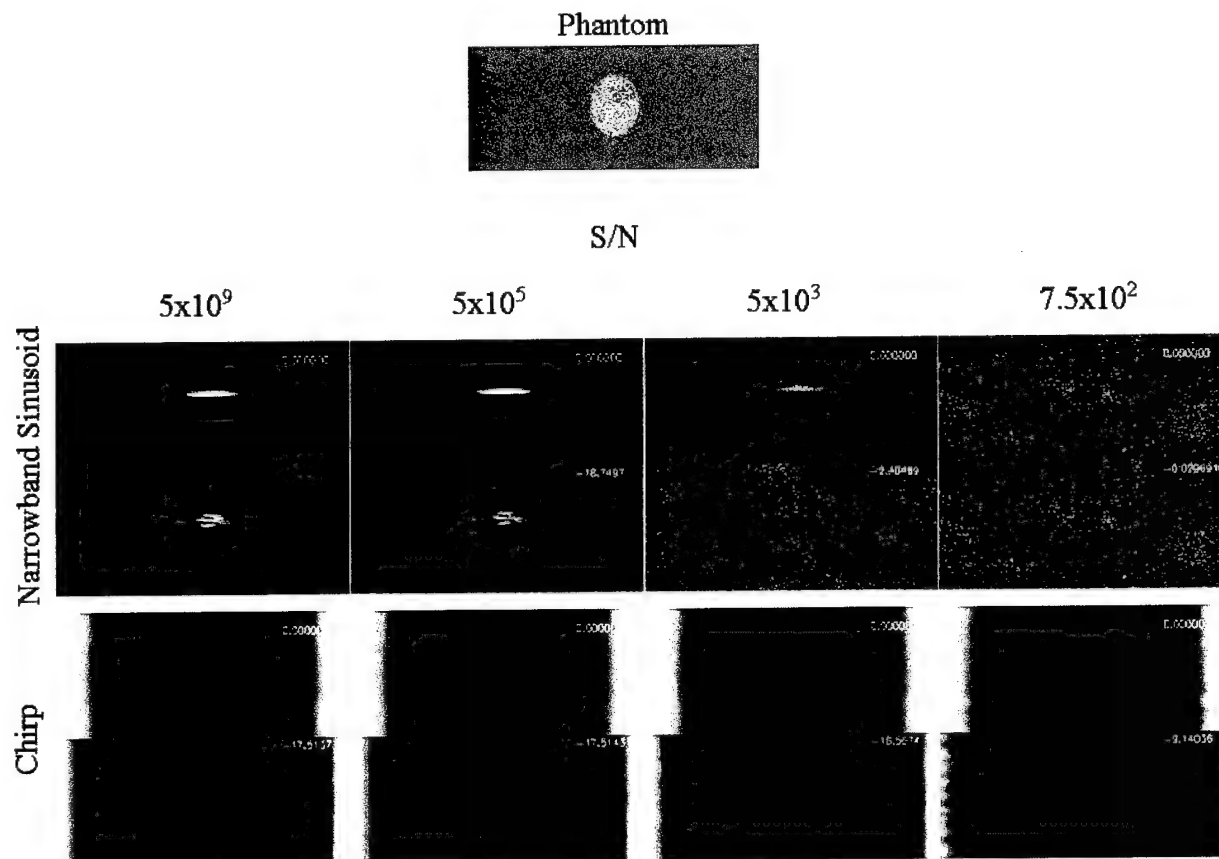


Figure 6-24. Effects of signal to noise ratio on image formation for narrowband sinusoid and apodized chirp. Noise source: signal electronics at the input and output.

As noise increases, the ability for the narrowband sinusoid to form a B-Scan image decreases whereas the apodized chirp continues to form an image throughout the signal to noise ratio range investigated. These results suggest that the apodized chirp can potentially image structures under very poor imaging conditions: objects deeply buried or highly occluded objects.

Figure 6-25 shows the effect of increasing the chirp sweep rate on B-Scan image reconstruction. Increasing the sweep rate while maintaining the apodization constant effectively increases the time-bandwidth product. The center frequency of the narrowband sinusoid had to be increased to match the average frequency of the apodized chirp to make the comparison.

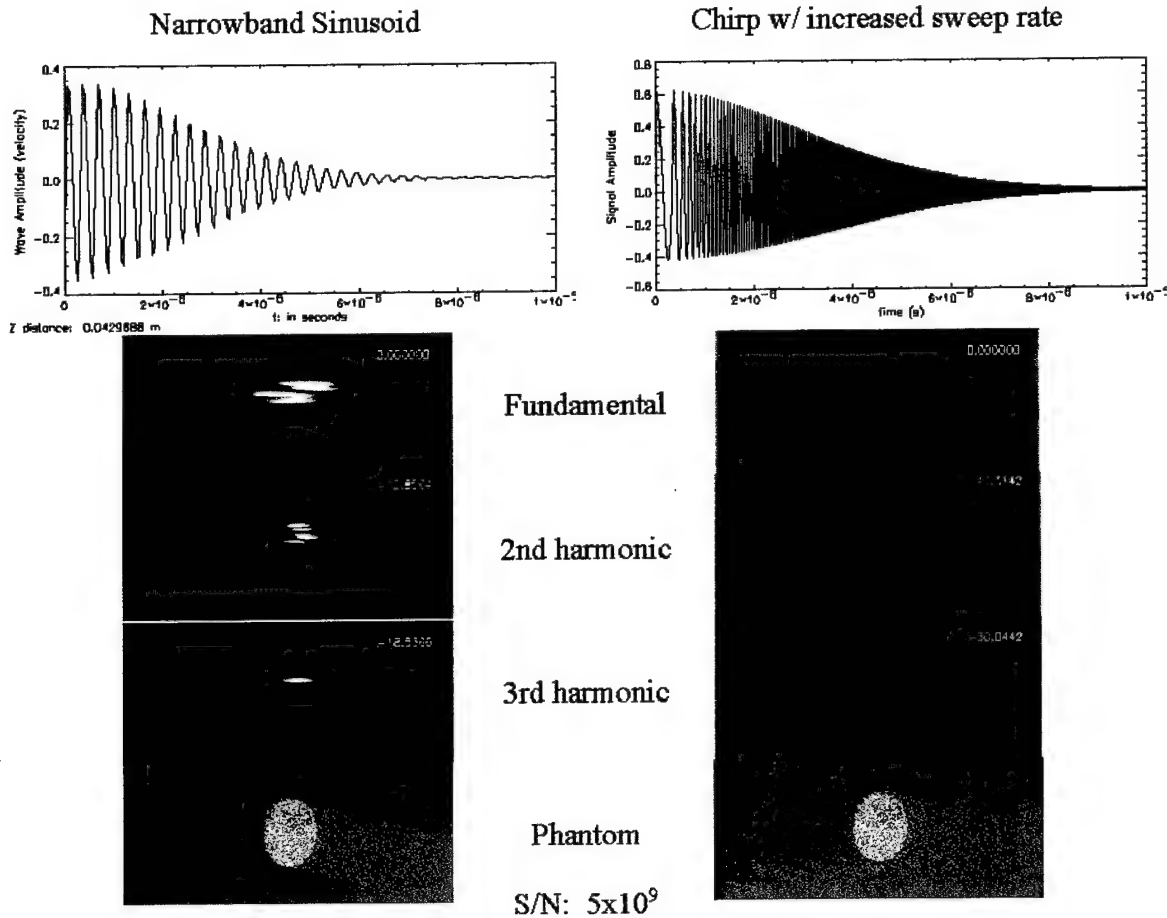


Figure 6-25. Effect of increasing chirp sweep rate while maintaining appropriate apodization and comparable center to average frequencies.

The increase in sweep rate produces improved apodized chirp B-Scan images (fundamental, second and third harmonics), with structural integrity and discrimination. These results suggest that the apodized chirp possesses additional flexibility in design over the narrowband sinusoid.

Chapter 6: Summary

The concept of onset distance is introduced. Onset distance is the propagation distance associated with the first time a frequency component reaches five percent of its maximum value. From the computations presented, the formation of harmonics is not strongly dependent on B/A ratio. Figures 6-3 and 6-4 tend to support Christopher's contention that the B/A ratio, β , is not significant to nonlinear wave formation results, with slopes of -0.034 and -0.032 for second and

third harmonics, respectively. Figure 6-5 suggests a stronger dependence on path attenuation than on B/A ratio, with slopes of -0.1030 and -0.0916 for second and third harmonics, respectively.

Figure 6-6 suggests that onset distance is strongly dependent on input signal amplitude, where the second and third harmonic onset distance "rate constants" are -0.53 and -0.52 , respectively. Likewise, Figure 6-7 shows a similar dependence on signal frequency is given as -0.45 for the second onset distance dependence and -0.47 for the third harmonic onset distance dependence.

When varying input frequency, image formation is significantly different, as evidenced in Figure 6-9. As the input frequency increases from 1 MHz to 4 MHz, different parts of the simulation phantom are accentuated. For instance, the "structural wall" is highlighted at the second harmonic of 2 MHz and at the fundamental of 4 MHz, suggesting that, for this particular phantom, the "structural wall" contains a fair amount of "4 MHz" energy to return to the sensing transducer. Also apparent is the "improved" image resolution at all second harmonic frequencies, improved over the fundamental of each frequency tested. The mottled image quality is typical of coherent imaging system output.

When varying B/A ratio, input signal amplitude, or wave velocity, there seems to be very little effect on image formation at the fundamental and second harmonic frequencies as evidenced in Figures 6-10, 6-11, 6-13, 6-14, 6-15, and 6-16. Differences appear to become significant at the third harmonic level. The primary effect of varying these parameters is manifested in the overall signal level for each harmonic. Figure 6-12 shows that the signal level increases as the B/A ratio increases, suggesting a "rule of thumb" for setting gain levels for various material types to be tested.

Results in Figure 6-20 shows that NUPROP's chirp model closely approximates the experimental data collected using the apparatus in Figure 6-19, using a Rayleigh distribution apodization function. The results also indicate that the original hypothesis that the chirp functions can be substituted as the bases functions in the Fubini solution to nonlinear wave propagation.

The results of comparing the narrowband sinusoid and apodized chirp, Figures 6-22 through Figure 6-25 suggest that, under typical ultrasound imaging conditions, the chirp provides very little image improvement. Only when the conditions deteriorate significantly will the chirp's efficacy become apparent: detecting structures deeply buried or highly occluded.

Chapter 7. Chapter Summaries and Recommendations

This chapter compiles all the chapter summaries and provides recommendations for future work related to this dissertation.

Chapter Summaries

From Chapter 2, the literature is replete with examples of ultrasound modeling techniques that capture aspects of the overall process. For nonlinear wave propagation, two models in literature are prominent: Christopher's NLP and the Khokhlov-Zabolotskaya-Kuznetsov (KZK) Implementation. Christopher's NLP is based on solutions to Burgers' equation and is implemented using a C-based code. Averkiou's Implementation is based on the KZK equation, that includes diffraction, attenuation, and nonlinearities in a single, third order partial differential equation.

For linear propagation, two methods are presented: angular spectrum and Lommel formulation. Angular spectrum implements a planar geometry derived mathematical convention using a propagation factor that accounts for complex field changes over small incremental distances. Angular spectrum suffers from computational size limitations, thus reducing its angular resolution capabilities. Also, since angular spectrum is developed using planar calculus, focused beam geometries are not easily accommodated.

Angular spectrum is applicable throughout the propagation path, from just in front of the transducer to as far as the user wished to compute the field. Additionally, angular spectrum is suitable for computing field propagation from non-radially symmetric geometries.

Lommel formulation implements planar as well as focused beam transducer geometries. However, Lommel is applicable for circularly symmetric geometries only. Additionally, Lommel

is strictly a linear propagation process. Therefore, any process that introduces nonlinearities, i.e. generation of harmonics, will necessarily be inaccurately predicted by Lommel.

Ultrasound image generation models dependent strongly on the tissue characterization or tissue construction model used. One model has found considerable favor in literature: Bamber and Dickinson's continuous array of point scatterers. If the tissue characteristic of interest can be modeled as an array of continuous point scatterers, then Bamber's technique is reasonably accurate in predicting linear ultrasound effects. Bamber's technique involves the convolution of the tissue array with the point spread function of the ultrasound pulse. Bamber accomplishes the convolution by taking the process to the Fourier domain and multiplying the Fourier transforms of the tissue array and the point spread function, then inverse Fourier transforming the product.

Though models exist for the various aspects of the ultrasound process, no single model encompasses all aspects of ultrasound propagation and, ultimately, ultrasound imaging. A new model, Nonlinear Ultrasound Propagation (NUPROP), is introduced that captures aspects of nonlinear wave generation and propagation, linear wave generation and propagation, and image generation.

From Chapter 3, NUPROP is a fairly complex simulation and analysis tool for ultrasound modeling. NUPROP represents an end-to-end modeling environment for studying ultrasound wave propagation and, ultimately, B-Scan image formation. This chapter discussed the generation of objects called phantoms using Bamber's continuous point scatterer concept. The tissue characteristic of interest was acoustic impedance. Input signal waveforms used in NUPROP are either sinusoidal or frequency modulated sinusoidal, either apodized (for image formation) or non-apodized (single frequency or continuous used for code verification and harmonic signal analyses).

Nonlinear propagation was modeled using either the Burgers' equation or Fubini solution approaches. Blackstock developed a closed form solution to the Burgers' equation that possessed the shock distance parameter, L , which is calculated from system parameters of velocity, initial wave amplitude, nonlinear parameter (β), and fundamental frequency. Likewise, the Fubini approach possessed this same shock distance limitation.

Linear propagation was modeled using Angular Spectrum and Lommel. Angular spectrum has the advantages of being applicable throughout the propagation path, accommodate non-radially symmetric transducer geometries, and accurately computes nonlinear or harmonic generation. Angular spectrum requires a trade-off between computational speed/volume and accuracy/precision in computing trans-axial beam profiles. Lommel, on the other hand, computes the on-axis longitudinal beam profile and the trans-axial beam profiles at depth with accuracy and precision. Unfortunately, Lommel formulation suffers from two major limitations: radial symmetry only and linear propagation only. Lommel does not predict harmonic signal formation nor does it accurately compute off-axis beam profiles for non-radially symmetric geometries. Lommel does not accurately compute the pressure field just in front of the transducer. A minimum propagation distance is required before Lommel can be used.

Image generation is accomplished using the Hilbert transform, which converts a RF signal to an "envelope" detected intensity signal.

Finally, NUPROP performs some rudimentary post processing such as statistical analyses, histogram plotting, and simple image thresholding based on the statistics of the images.

From Chapter 4, NUPROP is a modularly design IDL code that models, end-to-end, nonlinear ultrasound wave propagation and ultrasound image formation. NUPROP is based on "widgets," or controls, in the terminology of some development environments. Widgets are simple graphical

objects such as pushbuttons or sliders that allow user interaction via a pointing device (usually a mouse) and a keyboard. IDL graphical user interfaces are constructed by combining widgets in a tree-like hierarchy. Each widget has one parent widget and zero or more child widgets. There is one exception: the topmost widget (called a top-level base) is always a base widget and has no parent. So, NUPROP is a graphical user interface (GUI) providing the interactive platform for the user to exercise the physics associated with nonlinear and linear wave propagation.

Menu driven, NUPROP is built with modules (operations that are, essentially, stand-alone in that they do not need the GUI to work) and functions (modular code that requires parameter values passed through the GUI to operate). The complexity of each module or function determines the computational requirements, hence the computational time, accuracy, and precision.

From Chapter 5, NUPROP's nonlinear wave generation and propagation results compared favorably with data found in literature, having less than one percent difference comparing NUPROP's Fubini implementation with existing data (Ryan, [1963]) and less than a few percent between NUPROP's Burgers' solution and existing data. NUPROP also accurately predicted on-axis wave amplitude for propagation distances comparable to Averkiuo's simulation conditions. Additionally, NUPROP confirmed Averkiuo's supposition that, for equivalent areas, circular transducers produce equivalent on-axis longitudinal amplitudes as rectangular arrays (P3-2 geometry). However, NUPROP also showed that for wave or field amplitudes off-axis, Averkiuo's assumption is invalid.

In comparing trans-axial beam profiles derived from diffraction coupled with nonlinear propagation, NUPROP compared very favorably with literature (Christopher, [1997]), having less

than a few percent difference in trans-axial beam profile amplitudes for 2 MHz and its second harmonic at 4 MHz, within 1.5 cm radial distance from the axis.

Comparing NUPROP's RF and envelope detection simulated images with Bamber's technique for a point source. Bamber's simulation used a "skewed" or non-symmetric temporal pulse shape, whereas NUPROP assumes a temporally symmetric beam apodization. Comparing the 3 dB point for the most gradual fall-off, NUPROP is within one percent in computing the half power point, or 3 dB down from maximum intensity.

Given the favorable comparison of NUPROP's simulations of nonlinear wave generation and propagation using Fubini or Burgers' partial differential equation solutions, linear wave propagation (diffraction) using angular spectrum or Lommel formulation, and image formation using Bamber's technique, verification of NUPROP's viability as a simulation code is complete.

From Chapter 6, the concept of onset distance is introduced. Onset distance is the propagation distance associated with the first time a frequency component reaches five percent of its maximum value. From the computations presented, the formation of harmonics is not strongly dependent on B/A ratio. Figures 6-3 and 6-4 tend to support Christopher's contention that the B/A ratio, β , is not significant to nonlinear wave formation results, with slopes of -0.034 and -0.032 for second and third harmonics, respectively. Figure 6-5 suggests a stronger dependence on path attenuation than on B/A ratio, with slopes of -0.1030 and -0.0916 for second and third harmonics, respectively.

Figure 6-6 suggests that onset distance is strongly dependent on input signal amplitude, where the second and third harmonic onset distance "rate constants" are -0.53 and -0.52 , respectively. Likewise, Figure 6-7 shows a similar dependence on signal frequency is given as -0.45 for the second onset distance dependence and -0.47 for the third harmonic onset distance dependence.

When varying input frequency, image formation is significantly different, as evidenced in Figure 6-9. As the input frequency increases from 1 MHz to 4 MHz, different parts of the simulation phantom are accentuated. For instance, the "structural wall" is highlighted at the second harmonic of 2 MHz and at the fundamental of 4 MHz, suggesting that, for this particular phantom, the "structural wall" contains a fair amount of "4 MHz" energy to return to the sensing transducer. Also apparent is the "improved" image resolution at all second harmonic frequencies, improved over the fundamental of each frequency tested. The mottled image quality is typical of coherent imaging system output.

When varying B/A ratio, input signal amplitude, or wave velocity, there seems to be very little effect on image formation at the fundamental and second harmonic frequencies as evidenced in Figures 6-10, 6-11, 6-13, 6-14, 6-15, and 6-16. Differences appear to become significant at the third harmonic level. The primary effect of varying these parameters is manifested in the overall signal level for each harmonic. Figure 6-12 shows that the signal level increases as the B/A ratio increases, suggesting a "rule of thumb" for setting gain levels for various material types to be tested.

Results in Figure 6-20 shows that NUPROP's chirp model closely approximates the experimental data collected using the apparatus in Figure 6-19, using a Rayleigh distribution apodization function. The results also indicate that the original hypothesis that the chirp functions can be substituted as the bases functions in the Fubini solution to nonlinear wave propagation is valid.

The results of comparing the narrowband sinusoid and apodized chirp, Figures 6-22 through Figure 6-25 suggest that, under typical ultrasound imaging conditions, the chirp provides very

little image improvement. Only when the conditions deteriorate significantly will the chirp's efficacy become apparent: detecting structures deeply buried or highly occluded.

Recommendations

This section discusses additional experiments that could be conducted to further validate the IDL code as well as code related activities and potential improvements to NUPROP. Though couched in terms of NUPROP code validation and improvements, these recommendations also serve as potentially fruitful research areas in their own right and should be pursued whether or not they are part of NUPROP improvements. Code improvements include the addition of the diffraction integral and shift-and-add methods for computing linearly propagated wavefronts, complementing angular spectrum and Lommel; addition of indices commonly used in clinical diagnoses, namely the mechanical index which is an indicator of cavitation and the two thermal indices (cranial and soft tissue), which are indicators of thermal stress and potentially dangerous thermal loading. The use of more complex phantoms such as the piecewise homogeneous model or the addition of phase aberration are warranted.

NUPROP Code Validation

This section describes potential experimentation to validate NUPROP code for single frequency sinusoid cross-track beam profiling and pulse sinusoid image formation (B-Scan).

Single Frequency Sinusoid

NUPROP represents the culmination of a considerable body of research on nonlinear and linear propagation modeling. Considering nonlinear propagation first, the Fubini solution code has been verified against existing data and results from other simulation codes and validated against experimental data. The Burgers' computational model has been verified but not validated.

For linear propagation, the Lommel formulation module has been verified against existing data but is rudimentary, at best. This module requires more work to include angular or cross-track beam formation similar to the angular spectrum module. The angular spectrum module has been verified, but not validated with experimental data. Experiments similar to the apodized chirp should be conducted to determine the off axis (cross-track) beam profiles at the observation distance.

Figure 7-1 illustrates a cartoon of the experimental apparatus required to conduct beam profile determination.

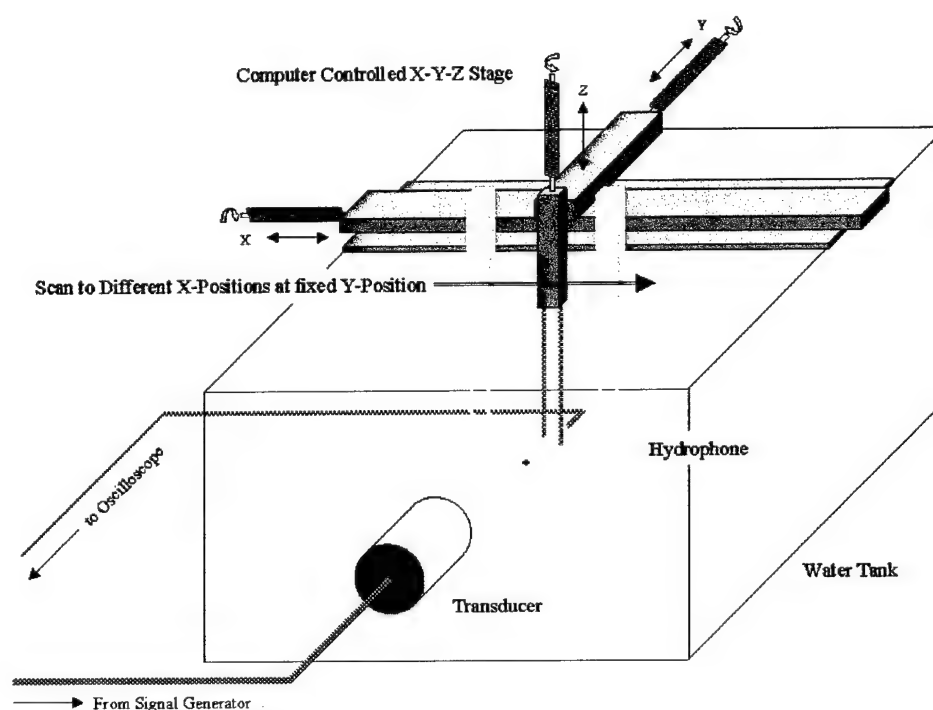


Figure 7-1. Cartoon rendition of beam profile measurement apparatus. Waveform from the signal generator drives the transducer (single frequency sinusoid). The hydrophone is accurately positioned using the computer controlled X-Y-Z stage. The Y-Position is fixed as the X-Position scans in micron steps across the ultrasound beam. Signals from the hydrophone are displayed on an oscilloscope, with further processing and data capture using a signal digitizer and computer (not depicted in this cartoon).

The transducer is driven by a signal from the signal generator: a single frequency sinusoid. The signal generator signal is sent to an oscilloscope for display. The hydrophone is positioned accurately using the computer controlled X-Y-Z stage. The Y-Position is fixed while the X-

position scans in micron steps. The signal from the hydrophone is sent to the oscilloscope for display. Both the original signal and the hydrophone signal are sent to a digitizer for data capture and then to the computer for processing and storage. The average signal strength at each X-Position is computed and plotted as a function of cross-track displacement. The computed cross-track beam profile is then compared with NUPROP's predicted cross-track beam profile for validation.

Pulse Sinusoid Image Formation (B-Scan)

Figure 7-2 depicts a cartoon rendition of the experimental apparatus used for pulse sinusoid image formation (B-Scan).

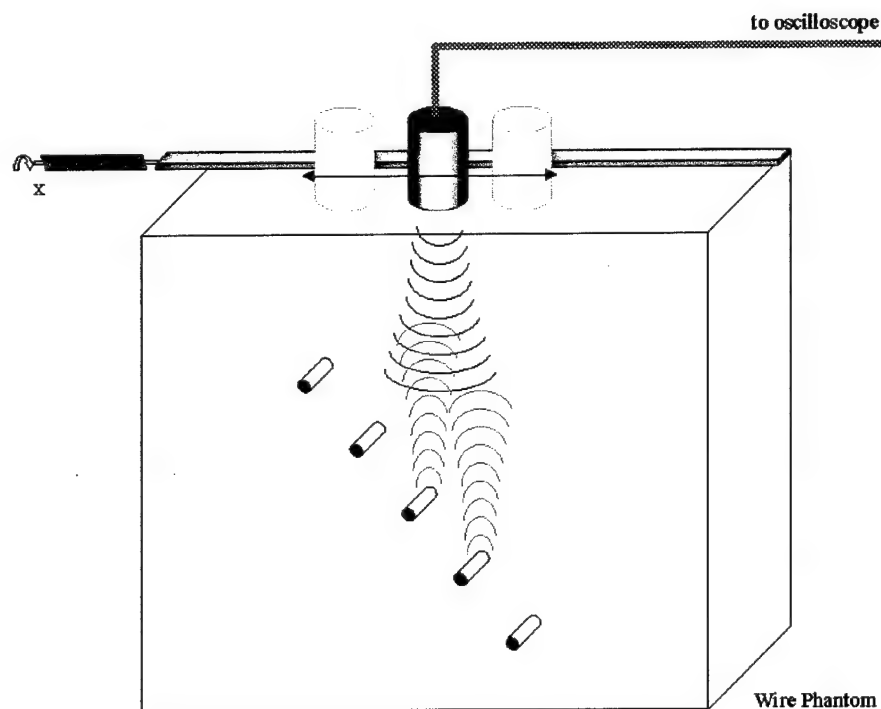


Figure 7-2. Illustration of experimental apparatus used for ultrasound B-scan imaging. A transducer is attached to a single stage computer controlled actuator for precision placement along the scan direction. A wire phantom containing several wires spatially displaced is insonified. The reflected ultrasound energy is captured by the transducer. The B-scan image is generated from A-line scans of the wire phantom at various points along the scan path.

Energy introduced by the transducer at each position interacts with structure along the propagation path. Energy reflected from the structures in the propagation path is collected over

the dwell time of the transducer. The time signal is commonly referred to as an A-Line scan. A-Line scans comprise the B-scan image after envelope detection.

Code Improvements

NUPROP currently models planar wavefronts. A significant improvement would be the introduction of focused wavefronts. This can be accomplished using an angular-spatial phase filter and employing angular spectrum. However, this method is not efficient as pointed out by Liu and Waag [1997]. The introduction of the diffraction integral method or the more empirical shift and add method, as mentioned in the Liu and Waag [1997] article, are more efficient and would complement the Angular Spectrum and Lommel techniques currently incorporated in NUPROP.

Diffraction Integral Method

The diffraction integral method relies on the fact that the pressure field satisfies the Helmholtz equation such that, at any arbitrary point, the value of the pressure field can be expressed as a surface integral

$$p(\vec{r}) = \iint_{S_o} \left[G(\vec{r}/\vec{r}_o) \frac{\partial p(\vec{r}_o)}{\partial \vec{n}_o} - p(\vec{r}_o) \frac{\partial G(\vec{r}/\vec{r}_o)}{\partial \vec{n}_o} \right] d\vec{r}_o \quad (7-1)$$

where S_o is an arbitrary surface enclosing the point \vec{r} , \vec{r}_o is a point on S_o , and \vec{n}_o is the outward pointing normal vector of S_o at \vec{r}_o . The Green's function, $G(\vec{r}/\vec{r}_o)$, is a general solution to the Helmholtz equation such that

$$G(\vec{r}/\vec{r}_o) = g(R) + \chi(\vec{r}) = \frac{e^{ikR}}{4\pi R} + \chi(\vec{r}) \quad (7-2)$$

where $R = |\vec{r} - \vec{r}_o|$ is the distance between \vec{r} and \vec{r}_o , $g(R)$ is the free-space outgoing Green's function as defined, and $\chi(\vec{r})$ is an arbitrary function satisfying the Helmholtz equation $(\nabla^2 + k^2)\chi(\vec{r}) = 0$ in the volume surrounded by the surface, S_o . So, the field at an arbitrary point in space can be computed using the field at a known point in space, namely on the surface surrounding the point, given two conditions: 1) the surface is comprised of a plane $z=0$ and the hemisphere at infinity enclosing the upper half space, and 2) the behavior of the pressure field at infinity is specified to satisfy the Sommerfeld radiation condition in Goodman [1968]. The pressure field at $p(x,y,z)$ is given as

$$p(x, y, z) = \frac{z}{2\pi} \iint_{\pm\infty} p(x_o, y_o, 0) \left(\frac{1}{R} - ik \right) \frac{e^{ikR}}{R^2} dx_o dy_o \quad (7-3)$$

or

$$p(x, y, z) = -\frac{1}{2\pi} \iint_{\pm\infty} \left. \frac{\partial p(x_o, y_o, z_o)}{\partial z_o} \right|_{z_o=0} \frac{e^{ikR}}{R} dx_o dy_o$$

where $R = \sqrt{(x - x_o)^2 + (y - y_o)^2 + z^2}$.

Shift-and-Add Method

The Shift-and-Add method can be derived from the diffraction integrals by an inverse Fourier transform of (7-3) with respect to time followed by a discretization of the integrals in space. Usually, the distance R is sufficiently large compared to the wavelength, λ , such that

$$p_\omega(x, y, z) = -\frac{ikz}{2\pi} \iint_{\pm\infty} p_\omega(x_o, y_o, 0) \frac{e^{ikR}}{R^2} dx_o dy_o \quad (7-4)$$

omitting the $1/R$ term from (7-3) and signifying that the equation applies to a single frequency component, ω . The inverse Fourier transform of (7-4) becomes

$$p(x, y, z, t) = \frac{z}{2\pi c} \iint_{\pm\infty} \dot{p}(x_o, y_o, 0, t - R/c) \frac{1}{R^2} dx_o dy_o \quad (7-5)$$

where $p(x, y, z, t)$ is the temporal pressure variation at point (x, y, z) and \dot{p} denotes the differentiation of p with respect to time. The subsequent discretization with respect to x_o and y_o yields

$$p(x, y, z, t) = \frac{z}{2\pi c} \Delta x_o \Delta y_o \times \sum_m \sum_n \dot{p}(x_{om}, y_{on}, 0, t - R_{mn}/c) \frac{1}{R_{mn}^2} \quad (7-6)$$

with $R_{mn} = \sqrt{(x - x_{om})^2 + (y - y_{on})^2 + z^2}$.

Both the Diffraction Integral and the Shift-and-Add methods accommodate focused wavefronts, and are computationally more efficient than Angular Spectrum in this respect. Since Fubini provides a linear approximation of a nonlinear process, namely, harmonic signal generation, coupling nonlinear and linear propagation using either the diffraction integral or shift-and-add methods is relatively simple.

Mechanical Effects: Cavitation and mechanical Index (MI)

The problem of cavitation has long been of interest in hydrodynamics, where it is primarily responsible for the destruction of propellers, turbines, and other moving parts. A fundamental problem is understanding the mechanism for cavitation, conditions that promote the onset of cavitation. As the name suggests, cavitation is the formation of "holes" in the liquid, usually under tensile stress. Depending on the conditions, the "holes" may be filled by dissolved gases in the liquid. However, for ideally "pure" liquids, cavitation indicates a ripping apart of the structure of the liquid. One potential measure of cavitation is the mechanical index (MI). In principle, the use of the mechanical index gives the user a means of judging the safety of clinical applications of ultrasound. Unfortunately, experimental evidence for mechanical damage within soft tissues from

diagnostic ultrasound is limited, at best. With the possible exception of lung hemorrhage, it is difficult to relate values of MI to specific hazards.

Mechanical Index is calculated from the measured peak negative pressure, p^- , in MPa as

$$MI = \frac{p^-}{\sqrt{f}} \quad (7-7)$$

where f is the frequency, in MHz. Peak negative pressure is calculated by reducing the acoustic pressure, measured in water, using an attenuation coefficient of $0.3 \text{ dB cm}^{-1} \text{ MHz}^{-1}$. This coefficient of attenuation is an approximate model of biological tissue, assuming homogeneous, single layer medium. MI indicates the amplitude of the ultrasonic pulses being used at any time. Increased pulse amplitudes result in proportionally higher MI values. The rationale is that increased amplitudes will potentially cause cavitation, or mechanical damage. Hence, MI becomes the measured parameter for determining potential mechanical damage in biological tissue. The formation of harmonics signals produces the potential for very high, localized velocity differentials. Compression and expansion within a very small distance can cause severe localized distortion. Figure 7-3 illustrates this condition. As the wave becomes more and more "sawtoothed" due to harmonic signal formation, the wavefront can exhibit near instantaneous maximum positive to maximum negative velocity within a few microns, introducing sufficient energy to break chemical bonds.

Nonlinear Wavefront

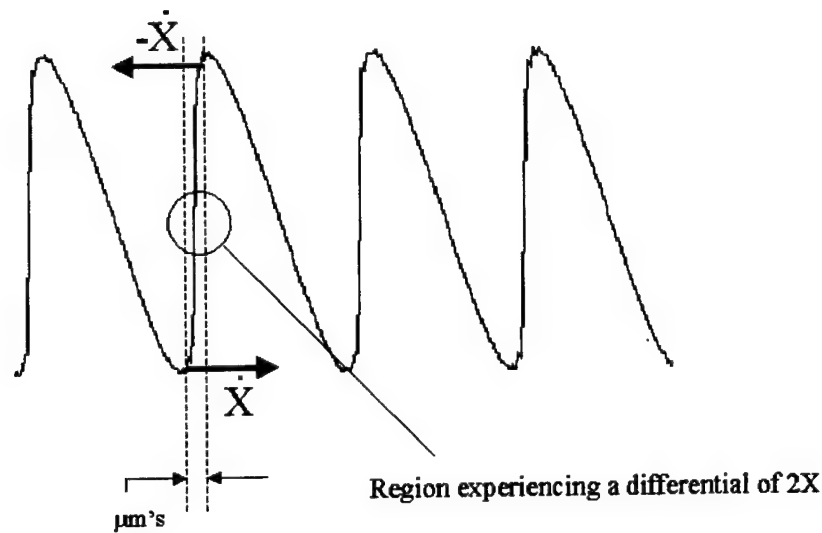


Figure 7-3. Potential wave differential. Region within a few microns has the potential of experiencing a nearly instantaneous velocity differential of $2\dot{X}$.

Nonlinear effects influence the achievable peak rarefactional pressure used in calculating MI. This peak negative pressure tends to saturate in water at the highest diagnostic outputs. For unfocused transducers, Carstensen's [1996] nonlinear propagation models underestimate the peak negative pressure by as much as 20%, even at relatively low source intensities. Christopher's nonlinear model [1997] showed an underestimation of 8% for the same transducer studied. Christopher employed a more sophisticated nonlinear model based on Burgers' equation. The accuracy and executability achieved with these computational techniques are critical to precise estimates of MI *in vivo*.

The source intensity tends to shift the beam focus closer to the source, even in "lossless" medium of water. The current protocol for derating clinical applications of ultrasound tends to shift the maxima closer to the source. Nonlinear propagation produces a strange absorption coefficient that increases in magnitude with distance from the source. As a consequence, the shift of the maximum pulse intensity becomes significant, resulting in a discontinuity, or potentially

damaging mechanical condition within the tissue. Even with this potentially damaging condition, it is still impossible to draw general conclusions on the MI error magnitudes introduced by nonlinearities. The field regime in which these discontinuities exist have little to no nonlinear effects. Underestimates as great as a factor of two have been demonstrated in specific experimental configurations.

Thermal Index (TI)

The second biophysical mechanism of interest is tissue heating, "quantified" using thermal index (TI), an estimate of the tissue temperature rise in °C which might occur under "reasonable worst-case conditions." Three thermal indices have been defined in literature: 1) soft tissue index (TIS), 2) bone index close to the transducer (Cranial conditions, TIC), and 3) bone index at or near the transducer focus (TIB). Thermal index is defined as the ratio of the acoustic power emitted to the power required to heat a particular target tissue by 1 °C, allowing time for thermal equilibrium.

Nonlinearities will limit the amplitude of fields distant from the source, but they also increase local absorption. These factors oppose each other's biological effects giving rise to nonlinear propagation either increasing or decreasing localized heating, depending on which mechanism is dominant under the observation conditions.

Thermal indices (TIs) are designed to estimate spatial maximum, steady-state temperature increments. For homogeneous tissue, the thermal index is defined as TIS and is given as the temperature increment at a fixed distance of ~2 cm from the source, not at the focus. At this distance, nonlinear propagation enhances local thermal increment by 10%. TIS for a given transducer configuration is expressed by one of two mathematical relationships

$$TIS = \frac{I_{0.3}(z)f}{210} \quad (7-8)$$

where $I_{0.3}(z)$ is the local, derated, temporal average intensity in mW/cm^2 , f is frequency, or

$$TIS = \frac{W_{0.3}(z)f}{210} \quad (7-9)$$

where $W_{0.3}(z)$ is the total, derated acoustic power at or near the focus where the effective area of the beam is less than 1 cm^2 .

When bone is the target tissue, nonlinear propagation has no effect on its absorption. The only effect of importance is the reduction of local fields and, thus, reduction of thermal loading or heating. Thermal Index for bone (TIB) is computed using

$$TIB = \frac{\sqrt{W_{0.3}(z)I_{0.3}(z)}}{50} \quad (7-10)$$

where z , in this case, is the depth that maximizes TIB.

Thermal indices used in clinical applications depend on total acoustic power, tissue absorption coefficient, frequency, beam size, tissue thermal capacity, tissue thermal conductivity, and estimates of blood perfusion for tissue cooling. Thermal index computational constants (210 for TIS, 50 for TIB) are derived from these properties. Since the propagation distance is very small for determining cranial thermal index (TIC), nonlinear propagation is a non-player.

By in large, nonlinear wave propagation plays a minor role in the TI Output Display Standard (ODS) because of the way thermal indices are defined and because of the protocols recommended for measuring acoustic power. In contrast to mechanical index (MI), thermal indices (TIs) were developed using well-understood heat generation and diffusion theories. The theories are straightforward and have been studied extensively. Although the theory may predict certain thermal characteristics, significant uncertainties still exist in clinical applications resulting in less

than desirable correlation between onscreen TI values and actual temperatures within the biological medium. However, TIs were designed to be conservative and, for the informed user, onscreen TI values can be useful in determining the potential for heat damage during examinations.

Wavefront "Movies"

From a display viewpoint, X-Z multiframe "movies" can help in understanding the qualitative nature of ultrasound wave interaction with the medium, objects, and other structures. Such models exist in literature and would make a useful addition to NUPROP. For instance, Wojcik, Mould, Ayter, and Carcione [1998] use a model based on the pseudospectral code that eliminate the use of lower order space and time derivative approximations which ultimately lead to greater versatility and efficiency at the expense of numerical accuracy. Also, their model relies on accurate modeling of abdominal wall morphology to capture the critical phase aberrant nature of biological interfaces. Such data exists. Careful measurements of abdominal wall section was accomplished by Hinkelman, Liu, Metlay, and Waag [1994] and Hinkelman, Mast, Orr, and Waag [1997].

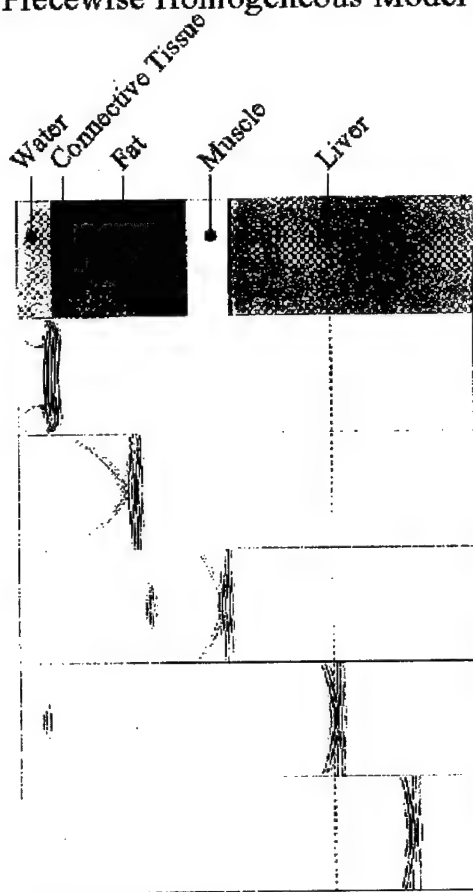
The pseudospectral method provides an extremely accurate approximation of spatial derivatives in homogeneous media using FFTs on a uniform Finite Difference (FD) grid. For a more detailed treatise on the pseudospectral method, see Fornberg [1996]. The price of high spatial accuracy is the necessity for space periodic construct. In other words, solutions exhibit a "wraparound" effect at the boundaries, whereby a wave exiting one side of the computational space appears on the other side. One way to circumvent wraparound is invoking Berenger's [1994] boundary condition, which forces boundary values to be "periodically small" at the

boundaries. Domain periodicity possesses another challenge in that waves are introduced as initial conditions rather than boundary conditions.

Accurate time-domain calculations use explicit time integrators such as the 4th order Runge-Kutta and the 4th order Adams-Bashforth. The pseudospectral technique uses multiple frequencies to accurately model power law frequency dependence. A least squares fitting procedure chooses model parameters for an optimal fit over a specified frequency range.

The pseudospectral technique facilitates the generation of 2-D simulations such as X-Z multiframe imaging. Such methods allow the user to watch the progression of a wavefront through a series of piecewise homogeneous layers as illustrated in Figure 7-4. Snapshots of a pulse propagation through a piecewise homogeneous abdominal wall is presented: Wojcik, et. al. [1998].

Piecewise Homogeneous Model



Piecewise Homogeneous w/ Fine Structure

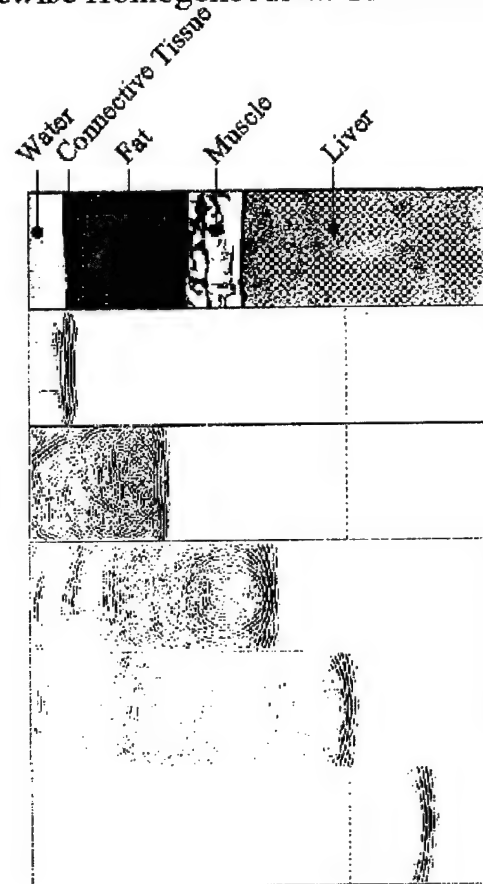


Figure 7-4. Snapshots of wave propagating through piecewise homogeneous layer models (Left: without fine structures, Right: with fine structures). The fine structure added to the model on the right is based on actual histological slices of abdominal wall structures. The fine structures introduce considerable diffuse scattering relative to the ideal model.

As is expected, the fine structure produces considerable diffuse scattering as illustrated in Figure 7-4: right. As the wave propagates through the fine structure, multiple reflections and, consequently, constructive and destructive interference on the reflection signal from these piecewise sections. This brings up another fruitful area of improvement: development of more complex, more realistic phantoms of tissue models.

More Complex Phantoms

However accurate a propagation model is, its “Achilles” heel is still the fidelity of the tissue model. More realistic models are crucial for simulating ultrasound images for qualitative and quantitative diagnostics.

Piece-wise Homogeneous (modeling inhomogeneity)

As previously mentioned, Wojcik, et. al. [1998] provides several piecewise homogeneous models for abdominal wall and multi-tissue structures based on histological slices and measured acoustic signals (Hinkelman, et. al. [1997]). Figure 7-3 shows the piecewise homogeneous model used by Wojcik, et. al. [1998]. Each section or structure possesses its own set of tissue parameters as given

Tissue/ Material	ρ [kg/m ³]	V [m/s]	B/A	Attenuation [dB/cm/MHz]	B
Water	1000	1500	5.0	0.002	2.0
Fat	928	1427	10.0	0.75	1.0
Connective	1100	1537	7.87	1.125	1.0
Muscle	1041	1571	7.5	0.55	1.0
Liver	1050	1577	6.75	0.4	1.0

Currently, NUPROP will model each section individually, propagating the wavefront from the front interface to the back interface through the material for one-way propagation studies (onset distance, single frequency studies), and back through the same layer for two-way propagation (image formation studies). NUPROP handles “external boundaries” by assuming perfectly matched layering (PML). Inter-tissue boundaries are modeled in NUPROP using point scatter difference amplitudes. In other words, different materials possess different maximum amplitudes, but have a zero mean value so as to eliminate artificially enhanced inter-tissue boundaries.

Phase Aberrating Interfaces

Biological tissues have the potential of introducing phase aberrations, or temporal shifts, in ultrasonic signals, thereby corrupting the reconstruction of the image (B-Scan). One method for correcting phase aberrations is backpropagation of a wavefront given known experimentally measured data, employing angular spectrum as the means of backpropagation. Liu and Waag

[1997] use such a technique, with the stipulation that the inhomogeneous medium is modeled such as by a phase screen placed some distance away from the aperture in an effort to be able to steer the transmit beam effectively to other regions within the interrogation space. This property of beam steering is crucial in image formation. Liu and Waag [1994] couple the backpropagation wave with a reference wave to generate time-shift compensation. Clearly, this technique is highly dependent on the accuracy of phase measurement or phase simulation. NUPROP currently assumes no phase distortion.

References

- Averkiou, M. A. and M. F. Hamilton, "Nonlinear distortion of short pulses radiated by plane and focused circular pistons," J. Acoust. Soc. Am., vol. 102, 1997.
- Averkiou, Michalakas A., David N. Roundhill, and Jeffry E. Powers, "A new imaging technique based on the nonlinear properties of tissues," IEEE Ultrasonics Symposium, pp. 1561-1566, 1997.
- Baker, A. C. and V. F. Humphrey, "Nonlinear propagation of short ultrasonic pulses in focused fields," in *Frontiers of Nonlinear Acoustics: Proceedings of 12th ISNA*, edited by M. F. Hamilton and D. T. Blackstock, London: Elsevier Applied Science, pp. 185-190, 1990.
- Baker, A. C., A. M. Berg, and J. N. Tjøtta, "The nonlinear pressure field of plane, rectangular apertures: Experimental and theoretical results," J. Acoust. Soc. Am., vol. 97, pp. 3510-3517, 1997.
- Bamber, J. C., and R. J. Dickinson, "Ultrasonic B-scanning: a computer simulation," Phys. Med. Biol., Vol. 25, No. 3, pp. 463-479, 1980.
- Bassett, L. W., and C. Kimme-Smith, "Breast sonography," American Journal of Roentgenology, vol. 156, pp. 449-455, 1991.
- Berenger, J. P., "A Perfectly matched Layer for the Absorption of Electromagnetic Waves," J. Computational Physics, vol. 114, pp. 185-200, 1994.
- Beyer, R. T., "Parameter of nonlinearity in fluids," J. Acoust. Soc. Am., vol. 32, pp. 719-721, 1960.
- Beyer, R. and S. Letcher, Physical Ultrasonics, New York: Academic Press, pp. 202-241, 1969.
- Carson, Paul L., et. al., "Effects of Nonlinear Ultrasound Propagation on Output Display Indices," Journal of Ultrasound Medicine, vol. 18, pp. 27-31, 1999.
- Carternsen, Edwin L., D. Dalecki, S. M. Gracewski, and T. Christopher, "Nonlinear Propagation and the Output Indices," Journal of Ultrasound Medicine, vol. 18, pp. 69-80, 1999.
- Chivers, R. C., Ultrasound Med. Biol., Vol. 3, p. 1, 1977.
- Christopher, P. Ted, "Experimental investigation of finite amplitude distortion-based, second harmonic pulse echo ultrasound imaging," IEEE Transactions on Ultrasonics, Ferromagnetics, and Frequency Control, vol. 45, no. 1, pp. 158-162, 1998.

Christopher, P. Ted, "Finite amplitude distortion-based inhomogeneous pulse echo ultrasonic imaging," IEEE Transactions on Ultrasonics, Ferromagnetics, and Frequency Control, vol. 44, no. 1, pp. 125-139, 1997.

Christopher, P. Ted, and E. L. Carstensen, "Finite amplitude distortion and its relationship to linear derating formulae for diagnostic ultrasound systems," Ultrasound Med. Biol., vol. 22, p. 1103, 1996.

Christopher, P. Ted, and Kevin Parker, "New approaches to nonlinear diffractive field propagation," J. Acoust. Soc. Am., vol. 90(1), pp. 488-499, 1991.

Daly, C., and N. A.H. K. Rao, "The Lommel diffraction formulations: an approximate Fourier transform pair leading to closed-form spatially integrated diffraction corrections," PACS numbers 43.20Rz, 43.20Fn, 43.20Bi, unpublished, 1999.

Daly, C. The arccos and Lommel diffraction formulations, Doctoral Thesis, Rochester Institute of Technology, 1998.

Easton, Roger L., Linear Imaging Mathematics, Class Notes, Rochester Institute of Technology, pp., 3-24, 6-7 through 6-24, 1997.

Fields, S., and F. Dunn, J. Acoust. Soc. Am., Vol. 54, p. 809, 1973.

Fornage, B. D., M. J. Faroux, and A. Simatos, "Breast masses. Ultrasound guided fine needle aspiration biopsy," Radiology, vol. 162, pp. 409-414, 1987.

Fornage, B. D., N. Sneige, and M. J. Faroux, "Sonographic appearance and aspiration biopsy of breast carcinomas smaller than 1 cm^3 ," Journal of Ultrasound in Medicine, vol. 9, pp. 559-568, 1990.

Fornage, B. D., J. D. Coan, and C. L. David, "Ultrasound guided needle biopsy of breast and other interventional procedures," Radiologic Clinics of North America, vol. 30, pp. 167-185, 1992.

Fornberg, B., A Practical Guide to Pseudospectral Methods, Cambridge University Press, 1996.

Fubini, E., Alta Frequenza, vol. 4, p. 539, 1935.

Gaskill, J., Linear Systems, Fourier Transforms, and Optics, New York: Wiley Interscience, 1978.

Goodman, J. W., Introduction to Fourier Optics, New York: MacGraw-Hill, 1968.

Gore, J. C., and S. Leeman, Phys. Med. Biol., Vol. 22, p. 297, 1977.

- Gray, Henry, T. P. Pick, and R. Howden, Gray's Anatomy, New York: Bounty Books, p. 467, 1977.
- Haran, M. and B. Cook, "Distortion of finite amplitude ultrasound in lossy media," J. Acoust. Soc. Am., col. 73, no. 3, pp. 774-779, 1983.
- Higgins, F. P., S. J. Norton, and M. Linzer, "Optical interferometric visualization and computerized reconstruction of ultrasonic fields," J. Acoust. Soc. Am., vol. 68, pp. 1169-1176, 1980.
- Hinkelman, L. M., D. L. Liu, L. A. Metlay, and R. C. Waag, "Measurements of Ultrasonic Pulse Arrival Time and Energy Level Variations Produced by Propagation through Abdominal Wall," J. Acoust. Soc. Am., vol. 95(1), pp. 530-541, 1994.
- Hinkelman, L. M., T. D. Mast, M. J. Orr, and R. C. Waag, "Effects of Abdominal Wall Morphology on Ultrasonic Pulse Distortion," Proc. IEEE Ultrasonics Symposium, pp. 1493-1496, 1997.
- Krishnan, S., J. D. Hamilton, and M. O'Donnell, "Suppression of propagating second harmonic in non-linear imaging," IEEE Ultrasonics Symposium, pp. 1567-1570, 1997.
- Kuni, C. C., "Mammography in the 1990s: A plea for objective doctors and informed patients," American Journal of Preventive Medicine, vol. 9, pp. 195-190, 1993.
- Kuznetsov, V. P., "Equation of nonlinear acoustics," Sov. Phys. Acoust., vol. 16, pp. 467-470, 1970.
- Lewin, P., "Transducer characterization using the angular spectrum method," J. Acoust. Soc. Am., vol. 85(5), pp. 2202-2214, 1989.
- Lighthill, J., Waves in Fluids, Cambridge: Cambridge University Press, pp. 78-83, 1980.
- Liu, Dong-Lai, and Robert Waag, "Propagation and Backpropagation for Ultrasonic Wavefront Design," IEEE Transactions on Ultrasonics, Ferromagnetics, and Frequency Control, vol. 44, no. 1, pp. 1-13, 1997.
- Logan, J. David, Applied Mathematics, New York: John Wiley and Sons, pp. 242-244, 1987.
- Nicholas, D., ed. D. N. White, Recent Advances in Ultrasound in Biomedicine, Vol. 1, chapter 1, 1977.
- Nikoonahad, M. and M. Vaez Iravani, "Focusing ultrasound in biological media," IEEE Transactions on Ultrasonics, Ferromagnetics, and Frequency Control, vol. 36, no. 2, pp. 209-215, 1989.

Oberhettinger, F., "On transient solutions of the 'baffled piston' problem, Journal of Research of the national Bureau of Standards-B: mathematics and mathematical physics, 65B(1):1-5, 1961.

O'Donnell, M., E. T. Jaynes, and J. M. Miller, "Kramers-Kronig relationship between ultrasonic attenuation and phase velocity," J. Acoust. Soc. Am., col. 69, no. 3, pp. 696-701, 1981.

Powers, J. P., "Computer simulation of linear acoustic diffraction," Acoustical Holography, edited by L. W. Kesler (Plenum, New York), vol. 7, pp. 193-205, 1976.

Ryan, R. P., Ph.D. Thesis, Brown University, 1963

Ryan, R. P., A. Lutsch, and R. T. Beyer, *J. Acoust. Soc. Am.*, 34, 31, 1962

Seghal, C. M. and J. F. Greenleaf, "Ultrasonic absorption and dispersion in biological media: a postulated model," J. Acoust. Soc. Am., col. 72, no. 6, pp. 1711-1718, 1982.

Stepanishen, P. R. and K. C. Benjamin, "Forward and backward projection of acoustic fields using FFT methods," J. Acoust. Soc. Am., vol. 71, pp. 803-812, 1982.

Trivett, D. and A. V. Buren, "Comments on 'Distortion of finite amplitude ultrasound in lossy media'," J. Acoust. Soc. Am., vol. 76, no. 4, pp. 1257-1258, 1984.

Wojcik, Greg, J. Mould, S. Ayter, and L. Carcione, "A Study of Second Harmonic Generation by Focused Medical Transducer Pulses," Proc. IEEE Ultrasonics Symposium, pp. 1583-1588, 1998.

Wolf, E., "The X_n and Y_n functions of Hopkins, occurring in the theory of diffraction," Journal of Optical Society of America, 43(3):218, 1953

Zabolotskaya, E. A. and R. V. Khoklov, "Quasi-plane waves in the nonlinear acoustics of confined beams," Sov. Phys. Acoust., vol. 15, pp. 35-40, 1969.

Appendices

Appendix I. Mathematical Development of Burgers' Equation

Borrowing from J. David Logan [1987], given the Burgers' relationship in (2) and substituting the assumed solution form, $u = f(z-vt)$, letting $s = z-vt$, yields

$$\begin{aligned} \frac{\partial f(s)}{\partial t} + f(s) \cdot \frac{\partial f(s)}{\partial z} - v \cdot \nabla^2 f(s) &= 0 \\ -vf'(s) + f(s)f'(s) - vf''(s) &= 0 \end{aligned} \quad (I-1)$$

Upon integration, (I-1) becomes

$$-vf(s) + \frac{1}{2}f^2(s) - vf'(s) = B \quad (I-2)$$

where B is a constant of integration, noting that $f(s)f'(s) = \frac{1}{2} \frac{d}{ds} f^2$, thus

$$\frac{df(s)}{ds} = \frac{1}{2v} [f(s) - (v - \sqrt{v^2 + 2B})][f(s) - (v + \sqrt{v^2 + 2B})] \quad (I-3)$$

Assuming $c^2 > -2B$, employing a separation of variables, and integrating, yields

$$\begin{aligned} s &= 2v \int \frac{1}{[f(s) - (v - \sqrt{v^2 + 2B})][f(s) - (v + \sqrt{v^2 + 2B})]} df \\ &= \frac{1}{2\sqrt{v^2 + 2B}} \ln \frac{(v + \sqrt{v^2 + 2B}) - f(s)}{f(s) - (v - \sqrt{v^2 + 2B})} \end{aligned} \quad (I-4)$$

for $(v - \sqrt{v^2 + 2B}) < f(s) < (v + \sqrt{v^2 + 2B})$

Solving for $f(s)$ yields

$$f(s) = \frac{(v + \sqrt{v^2 + 2B}) + (v - \sqrt{v^2 + 2B})e^{\frac{s}{v}\sqrt{v^2 + 2B}}}{1 + e^{\frac{s}{v}\sqrt{v^2 + 2B}}} \quad (\text{I-5})$$

Thus, the traveling wave solution to Burgers' equation is given as

$$\begin{aligned} u(z, t) &= f(z - vt) \\ &= \frac{v + \sqrt{v^2 + 2B} + [v - \sqrt{v^2 + 2B}]e^{\frac{z - vt}{v}\sqrt{v^2 + 2B}}}{1 + e^{\frac{z - vt}{v}\sqrt{v^2 + 2B}}} \end{aligned} \quad (\text{I-6})$$

To avoid confusion, the velocity is usually denoted as c , thus (I-6) becomes

$$\begin{aligned} u(z, t) &= f(z - ct) \\ &= \frac{c + \sqrt{c^2 + 2B} + [c - \sqrt{c^2 + 2B}]e^{\frac{z - ct}{v}\sqrt{c^2 + 2B}}}{1 + e^{\frac{z - ct}{v}\sqrt{c^2 + 2B}}} \end{aligned} \quad (\text{I-7})$$

It should be noted that, without the viscosity term, $-v\nabla^2 u$, the wave will tend to "shock" faster and form a "breaking" wave. The viscosity term acts as a dampening of the nonlinear term,

$$u \cdot \frac{\partial u}{\partial z}.$$

Appendix II. Mathematical Development of Fubini's Solution

Beyer and Letcher [1969] provided the following derivation:

The particle velocity, $u = \xi$, is a function of density (ρ) or, likewise, condensation (s) such that

$$\rho = \rho_o(1 + \partial\xi/\partial z) \quad \text{or} \quad s = \frac{1}{(1 + \partial\xi/\partial z)} - 1 \quad (\text{II-1})$$

It follows that u can be written as a general function of $\partial\xi/\partial z$ such that $u = F(\partial\xi/\partial z)$ thus

$$\xi'' = f' \left(\frac{\partial\xi}{\partial z} \right) \frac{\partial^2\xi}{\partial z \partial t} \quad \text{and} \quad \frac{\partial^2\xi}{\partial z \partial t} = f' \frac{\partial^2\xi}{\partial z^2} \quad (\text{II-2})$$

Such that

$$\xi'' = (f')^2 \cdot \frac{\partial^2\xi}{\partial z^2} \quad (\text{II-3})$$

Comparing (II-3) with (II-2), letting $\gamma = 1 + \frac{B}{A}$ yields

$$f' = \frac{\pm c_o}{(1 + \partial\xi/\partial z)^{1 + \frac{B}{2A}}} \quad (\text{II-4})$$

Upon integration of (II-4) the following result is obtained

$$f = u = \frac{\pm c_o}{(1 + \partial \xi / \partial z)^{\frac{B}{2A}}} \left(\frac{-2A}{B} \right) + K \quad (\text{II-5})$$

In the absence of sound, $\partial \xi / \partial z$ equals 0 and u equals 0, such that

$$K = \frac{\pm 2Ac_o}{B} \quad (\text{II-6})$$

leading to

$$u = \pm \frac{2Ac_o}{B} \left(1 - \frac{1}{(1 + \partial \xi / \partial z)^{\frac{B}{2A}}} \right) = \pm \frac{2Ac_o}{B} \left(1 - (1 + s)^{\frac{B}{2A}} \right) \quad (\text{II-7})$$

By restricting the wave traveling in the +z direction and assuming that $\partial \xi / \partial z$ is negligibly small, then the rate of wave propagation as a function of particle velocity becomes

$$v = c_o \left(1 + \frac{B}{2A} \frac{u}{c_o} \right)^{\frac{2A}{B} + 1} \quad (\text{II-8})$$

The general solution of (6) is given as

$$u = F\left[\omega\left(t \pm \frac{z}{v}\right)\right] \quad (\text{II-9})$$

such that

$$\frac{\partial u}{\partial t} = F' \cdot \omega$$

$$\frac{\partial^2 u}{\partial t^2} = F'' \cdot \omega^2$$

$$\frac{\partial u}{\partial z} = F' \cdot \left(\pm \frac{1}{v} \right) \omega$$

$$\frac{\partial^2 u}{\partial z^2} = F'' \cdot \left(\frac{1}{v} \right)^2 \omega^2$$

(II-10, 11, 12, and 13)

Equating (II-13) and (II-11), the following is obtained

$$\frac{1}{\omega^2} \frac{\partial^2 u}{\partial t^2} = \frac{v^2}{\omega^2} \frac{\partial^2 u}{\partial z^2}$$

(II-14)

or

$$\frac{\partial^2 u}{\partial t^2} = v^2 \frac{\partial^2 u}{\partial z^2}$$

(II-15)

If the wave possesses a boundary condition of

$$u(0, t) = u_o \sin(\omega t)$$

(II-16)

then the general solution will be

$$\begin{aligned}
u(z,t) &= u_o \sin \left[\omega \left(t - \frac{z}{c_o} \left(1 + \frac{B}{2A} \frac{u}{c_o} \right)^{-\left(\frac{2A}{B}+1\right)} \right) \right] \\
&= u_o \sin \left[\omega t - \frac{\omega z}{c_o} \left(1 + \frac{B}{2A} \frac{u}{c_o} \right)^{-\left(\frac{2A}{B}+1\right)} \right] \\
&= u_o \sin \left[\omega t - kz \left(1 + \frac{B}{2A} \frac{u}{c_o} \right)^{-\left(\frac{2A}{B}+1\right)} \right]
\end{aligned}
\tag{II-17}$$

where $k = \frac{\omega}{c_o}$. By using binomial expansion on $\left(1 + \frac{B}{2A} \frac{u}{c_o} \right)^{-\left(\frac{2A}{B}+1\right)}$, and keeping only the first two terms, yields

$$u(z,t) \approx u_o \sin \left[\omega t - kz \left(1 - \left\{ 1 + \frac{B}{2A} \right\} \frac{u}{c_o} \right) \right]
\tag{II-18}$$

At this point, the concept of the discontinuity distance (l) must be introduced. By observation, one can see that a discontinuity will occur when the denominator term of (II-5), $\partial \xi / \partial z$, becomes negative 1. The denominator term must approach negative infinity at some propagation distance due to the fact that large values of u will propagate faster than small values of u , thus giving rise to wave distortions. This phenomenon is commonly referred to as a "shock front." Fubini computed this distance from the origin to the point where the shock forms as

$$l = \frac{c_o^2}{(B/2A + 1)\omega u_o}
\tag{II-19}$$

Substituting (II-19) into (II-18) yields

$$\frac{u}{u_o} = \sin \left[\omega t - kz + \frac{z}{l} \frac{u}{u_o} \right] \quad (\text{II-20})$$

which can be expanded into a Fourier series such that

$$\frac{u}{u_o} = \sum_{n=1}^{\infty} B_n \sin[n(\omega t - kz)] \quad (\text{II-21})$$

where

$$B_n = \frac{1}{\pi} \int_0^{2\pi} \frac{u}{u_o} \sin[n(\omega t - kz)] d(\omega t - kz) \quad (\text{II-22})$$

Substitution of (II-20) into (II-22) yields

$$B_n = \frac{2l}{nz} J_n \left(\frac{nz}{l} \right) \quad (\text{II-23})$$

Such that

$$\frac{u}{u_o} = \sum_{n=1}^{\infty} \frac{2l}{nz} J_n \left(\frac{nz}{l} \right) \sin[n(\omega t - kz)] \quad (\text{II-24})$$

For distances in excess of l , this explicit solution becomes invalid. Upon examination of (II-24), several characteristics can be observed:

1. The fundamental component of the wave will decrease as the wave propagates, as well as harmonics increase

2. If the initial wave amplitude is significant, then the wave will propagate a shorter distance before experiencing shock
3. As frequency increases, the shock distance will decrease
4. The ratio, u/u_o , can be viewed as appropriately weighted sum of frequency dependent, sinusoidal basis functions.

Appendix III: Linear Frequency Modulated Input Signal (Chirp)

Another multiple frequency input signal is the linear frequency modulated input signal commonly referred to as the chirp. Arguably one of the most useful linear filtering techniques is the use of the quadratic phase filter or chirp. The primary advantage of using a chirp signal over a single frequency sinusoid, or apodized sinusoid, is the ability to have a very wide bandwidth, infinite in fact, while maintaining reasonable signal gain (or signal to noise ratio). From Easton [1997], the quadratic phase filter has an impulse response of

$$h(x) = \frac{1}{|\alpha|} e^{\mp i \frac{\pi}{4}} e^{\pm i \pi \left(\frac{x}{\alpha}\right)^2} \quad (\text{III-1})$$

where α is the chirp rate, and a frequency domain form of

$$\mathfrak{F}\{h(x)\} = \mathfrak{F}\left\{\frac{1}{|\alpha|} e^{\mp i \frac{\pi}{4}} e^{\pm i \pi \left(\frac{x}{\alpha}\right)^2}\right\} = e^{\mp i \pi (\alpha \xi)^2} \quad (\text{III-2})$$

Hence, the frequency domain representation of the chirp is a chirp. This means that both the impulse response and the quadratic phase filter have constant magnitude and infinite support. For large values of α , the space-domain chirp will oscillate slowly whereas its frequency-domain counterpart will oscillate quickly.

Because the chirp is an all-pass filter, the complex correlation of its impulse response is a delta function as demonstrated using the filter theorem in the frequency domain

$$\begin{aligned} \mathfrak{F}\{h(x) \circ h^*(x)\} &= \mathfrak{F}\{h(x) * h^*(-x)\} = \mathfrak{F}\{h(x)\} \cdot \mathfrak{F}\{h^*(-x)\} \\ &= e^{\mp i \pi (\alpha \xi)^2} \cdot e^{\pm i \pi (\alpha \xi)^2} = 1(\xi) \rightarrow \mathfrak{F}^{-1}\{1(\xi)\} = \delta(x) \end{aligned} \quad (\text{III-3})$$

This is a very important characteristic because, if the return signal is comprised of a complex summation of chirp signals, i.e. the introduction of a chirp ultrasound into a biological medium, it

can be analyzed using an appropriate “chirp mask” to determine signal content, penetration depth, etc. A chirp mask can be comprised of a series of linearly shifted chirp signals, representing different penetration depths. Figure III-1 illustrates a simple, linear “chirp mask,” 512 by 512, shifted by one pixel in the x direction for every y-direction pixel. For this illustration, the maximum mask extent is 20 cm in both the x and y directions.

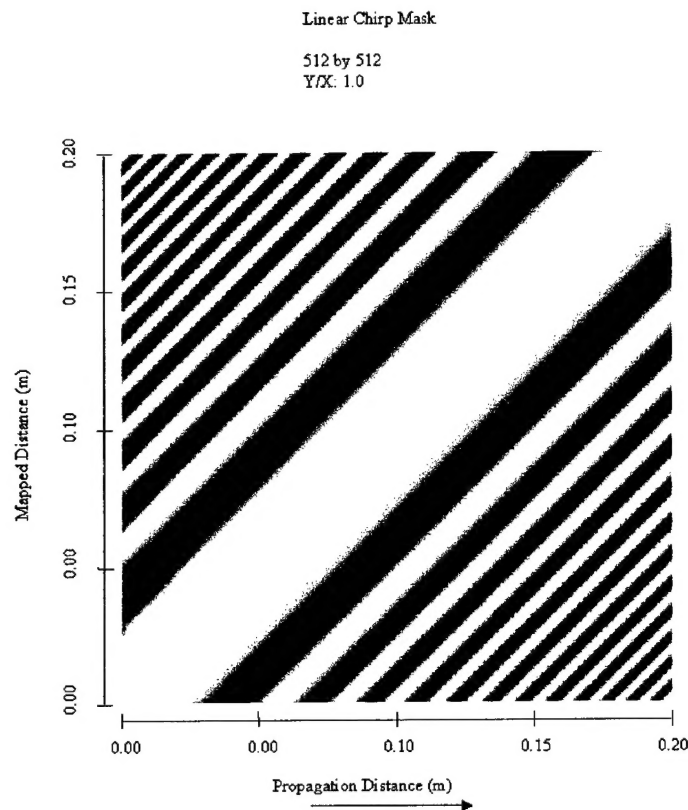


Figure III-1. Linear Chirp Mask. The linear chirp mask is comprised of a “stack” of a given chirp appropriately shifted in the mapped direction as a function of shift in the propagation direction. For this example, every shift in the propagation direction is matched, one for one, by a shift in the mapped direction

A linear chirp mask is one that does not introduce nonlinear effects as a function of propagation distance. So, as the chirp pulse propagates, no harmonics are introduced. Additionally, no amplitude modulation is introduced by the medium for this example. A return signal from various regions within the propagation path will be a complex summation of the chirp signal, appropriately shifted in space to represent the distance traveled by the chirp pulse. The

complex return chirp signal is correlated with the chirp mask and the correlation peaks are computed. For this example, a complex return signal is generated from the summation of chirps at positions (chirp numbers) 40, 70, 100, 130, 160, 190, 220, and 250. These positional numbers correspond to 0.016, 0.027, 0.039, 0.051, 0.063, 0.074, 0.086, and 0.098m propagation distances, respectively. Figure III-2 shows the effect of additive noise on the correlation of the return chirp signal with the linear chirp mask.

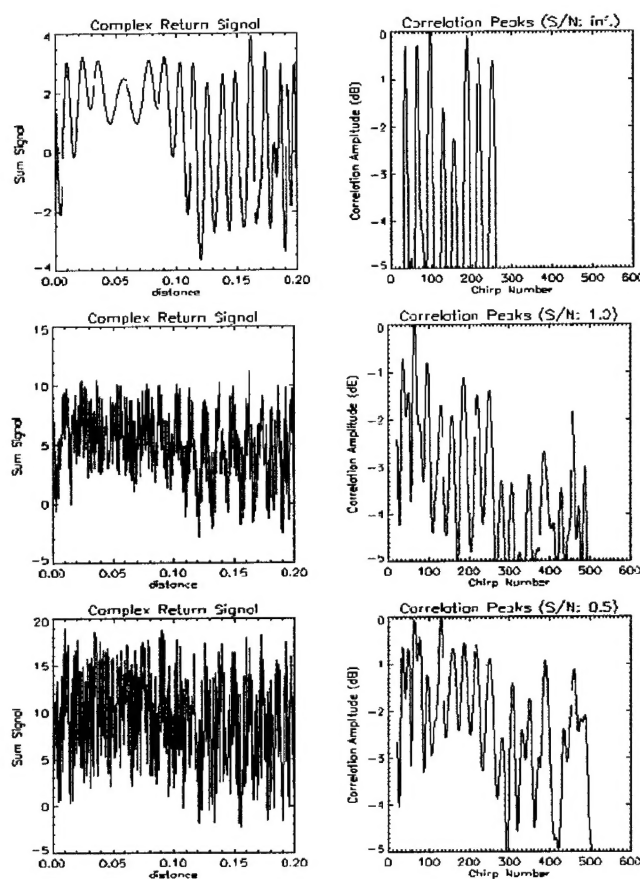


Figure III-2. Effect of noise on correlation between complex signal and chirp mask. The top graph depicts a complex return signal with no additive noise and its correlation as a function of chirp number. Each peak matches exactly the location in the propagation path of each reflection point. The center graph depicts a noisy return signal and its correlation with the chirp mask. Even under these stressful conditions, the peaks are discernable. The bottom graph depicts an extremely stressful sensing condition: S/N of 0.5. The correlation peaks are essentially obliterated by the noise.

For no noise conditions, the correlation peaks are clearly distinguishable and correspond exactly with the chirp numbers 40, 70, 100, 130, 160, 190, 220, and 250, respectively. As noise

increases, the correlation peaks become less and less prominent, until, at a noise level twice the signal level, the correlation peaks are nearly lost, save a few. Note that under these conditions, boosting the gain of the signal channel will necessarily boost the noise, thus providing no signal to noise improvement. The chirp provides high gain in noise or clutter environments due to its autocorrelation characteristics (i.e. impulse response) while maintaining an infinite bandwidth, in theory. In practice, the chirp still provides high gain characteristics, but the apodization, or spatio-temporal windowing, will limit the bandwidth. Likewise, the transducer's spatio-temporal characteristics will limit the actual detected (and processed) signal.

Now, add the complexity of nonlinear or harmonic generation. As the chirp propagates in the medium, each frequency within the chirp duration will potentially undergo nonlinear wave formation. So, the question arises: can the Fubini or Burgers' approaches be modified to account for a linear frequency modulated input as its initial condition? Consider the following derivation:

Given a function $f(z, t)$ such that

$$f(z, t) = e^{-i\pi[\omega t - kz]^2} \quad (\text{III-4})$$

Then the second partial derivative of $f(z, t)$ with respect to z is given as

$$\frac{\partial^2 f}{\partial z^2} = f(z, t) \left[-i2\pi k^2 + (i2\pi k\omega t - i2\pi k^2 z)^2 \right] \quad (\text{III-5})$$

And the second partial derivative of $f(z, t)$ with respect to t is given as

$$\frac{\partial^2 f}{\partial t^2} = f(z, t) \left[-i2\pi\omega^2 + (i2\pi k\omega z - i2\pi\omega^2 t)^2 \right] \quad (\text{III-6})$$

Now, suppose

$$\frac{\partial^2 f}{\partial t^2} = \gamma \frac{\partial^2 f}{\partial z^2} \quad (\text{III-7})$$

with $k = \frac{\omega}{c_o}$ and $z = c_o t$, where c_o is the group wave velocity. Then

$$\begin{aligned} \frac{\partial^2 f}{\partial t^2} &= f(z, t) \left[-i2\pi(c_o k)^2 + (i2\pi c_o^2 k^2 t - i2\pi c_o^2 k^2 t)^2 \right] \\ &= \gamma f(z, t) \left[-i2\pi k^2 + (i2\pi c_o k^2 t - i2\pi c_o k^2 t)^2 \right] \\ &\Rightarrow -i2\pi c_o^2 k^2 = \gamma (-i2\pi k^2) \\ &\Rightarrow \gamma = c_o^2 \end{aligned} \quad (\text{III-8})$$

in the absence of nonlinearities, yielding

$$\frac{\partial^2 f}{\partial t^2} = c_o^2 \frac{\partial^2 f}{\partial z^2} \quad (\text{III-9})$$

Comparing (III-9) with (3-6) implies that the Fubini solution for the chirp should be similar to the single sinusoid input, with the basis functions now being chirps with varying initial frequencies such that

$$\frac{u}{u_o} = 2 \sum_{n=1}^{\infty} \frac{J_n(nz/l)}{(nz/l)} \text{CHIRP}(ns) \text{GAUSS}(ns) \quad (\text{III-10})$$

where $\text{CHIRP}(ns)$ is defined as $e^{\pm i\pi(s)^2}$, $\text{GAUSS}(ns)$ as $e^{-\pi \left(\frac{s}{\sqrt{2}\sigma} \right)^2}$, s and σ defined as previously.

It is this hypothesis on which NUPROP constructs the Chirp-nonlinear result.